


UNIVERSITA' DELLA CALABRIA

Dipartimento di Ingegneria Informatica, Modellistica, Elettronica e Sistemistica

Scuola di Dottorato

Scienza e Tecnica "Bernardino Telesio"

XXVIII CICLO

Con il contributo della Regione Calabria

Programma Operativo Regionale (POR) Calabria - FSE 2007/2013

Asse V - Obiettivo Operativo N. 4 (Progetto RISPEISE)

IMPERFECTION SENSITIVITY ANALYSIS OF THIN WALLED SHELL STRUCTURES

Settore Scientifico Disciplinare

ICAR/08

Direttore: **Ch.mo Prof. Roberto Bartolino**

Supervisore: **Ch.mo Prof. Antonio Madeo**

Dottorando: **Dott. Giovanni Zucco**

A Dio per il dono della vita;

a Papa', Mamma e Chicca
con immenso amore;

ad Antotnio Madeo e p. Luigi Cortese
perche' senza di loro, molto probabilmente,
questo lavoro non ci sarebbe mai stato.

Contents

Introduction **1**

1 Koiter's asymptotic approach **3**
1.1 Introduction . . . 3
1.2 Foundamental equations . . . 4
1.3 Imperfection sensitivity analysis . . . 7

2 Corotational Formulation **8**
2.1 Introduction . . . 8
2.2 Geometrically linear formulation . . . 10
2.2.1 Mixed finite element . . . 12
2.3 Geometrically non linear formulation . . . 13
2.4 Element implementation . . . 15
2.4.1 Assumed stresses . . . 16
2.4.2 Assumed displacements . . . 17
2.4.3 Compliance and compatibility . . . 18
2.5 High order energy variations . . . 19
2.5.1 *Second-order variations* . . . 20
2.5.2 *Third-order variations* . . . 20
2.5.3 *Fourth-order variations* . . . 21

3 MISS-4 flat shell finite element: numerical assessment **22**
3.1 Introduction . . . 22
3.2 Linear static analysis of laminated plates . . . 22
3.2.1 Buckling analysis of a laminated square plate . . . 24
3.3 Linear and buckling analysis of laminated folded plates . . . 30
3.3.1 Clamped beam with Ω-section under shear force . . . 30
3.3.2 Clamped beam C-section under shear force . . . 32
3.3.3 Clamped box under torsional couple . . . 34
3.4 Further remarks . . . 37

4 Koiter asymptotic analysis of laminated composite plates **38**
4.1 Introduction . . . 38
4.2 Square plate under compression . . . 39
4.3 Hinged cylindrical roof . . . 42
4.4 Channel section under compression . . . 44
4.5 Further remarks . . . 46

5 Imperfection sensitivity analysis **48**
5.1 A rack member in compression 48
5.1.1 Buckling analysis 51
5.1.2 Post-buckling and imperfection sensitivity analysis 51
5.1.3 Limit load and worst case imperfection 55
5.1.4 A virtual laboratory for imperfection sensitivity analysis 62
5.1.5 Remarks on Koiter's asymptotic analysis 64
5.2 A laminated composite hinged box in compression 71
5.2.1 Buckling analysis 71
5.2.2 Post-buckling and imperfection sensitivity analysis 72
5.3 A laminated composite box beam in compression 77
5.3.1 Buckling analyses 77
5.3.2 Post-buckling and imperfection sensitivity analyses 79
5.4 Laminated composite cylindrical shells in compression 84
5.4.1 Buckling analysis 84
5.4.2 Post-buckling and imperfection sensitivity analysis 85
5.4.3 A virtual laboratory for imperfection sensitivity analysis of laminated composite cylindrical shells 88
5.4.4 Further remarks 94

Conclusions **96**

List of Figures

2.1 Corotational frame. 14
2.2 Global, local and internal coordinate systems. 15

3.1 Simply supported square plate. Geometry and mesh. 23
3.2 Simply supported square plate [0/90/0]. Convergence of bending moments and shear forces at point E, for regular for various values of span-to-thickness ratio. The solid line represents h^2 (shown for reference). S8R (Abaqus) and HQ4 [68] results are shown for comparison. 25
3.3 Simply supported square plate [0/90]. Convergence graphs for flexural moments, shear stress resultant, and axial stress resultant at point E for different span-to-thickness ratio using regular mesh. S8R (Abaqus) and HQ4 [68] results are shown for comparison. 26
3.4 Simply supported square plate $[-45/45]$. Convergence graphs for flexural moments resultant at points A and C for different span-to-thickness ratios using regular mesh. S8R (Abaqus) and HQ4 [68] results are shown for comparison. . . 27
3.5 Simply supported square plate $[30/-60/60/-30]$. Convergence graphs for flexural moments resultant at points A for different span-to-thickness ratio using regular mesh. S8R (Abaqus) and HQ4 [68] results are shown for comparison. 27
3.6 Simply supported square plate for different LSS. Convergence graphs using s-norm, for different span-to-thickness ratio using regular and distorted mesh. . . . 28
3.7 Square plate $[0/90/90/0]_S$ under uniaxial compression. Buckling modes. 29
3.8 Square plate $[0/90/90/0]_S$ under uniaxial compression. Convergence of buckling loads with mesh refinement. The solid line represents h^2 (for reference). 29
3.9 Clamped beam with Ω-section. Geometry, boundary conditions and mesh. 31
3.10 Clamped beam with Ω-section for different LSS. Convergence graphs using s-norm, for different values of a/t using regular mesh. The solid line represents h^2 (shown for reference). 31
3.11 Clamped beam C-section. Geometry, boundary condition and mesh. 32
3.12 Clamped beam with C-section under shear forces for different LSS. Convergence of buckling loads with mesh refinement. The solid line represents h^2 (for reference). 33
3.13 Clamped beam with C-section for LSS=LSS_1. Buckling modes corresponding to buckling loads $\lambda_1..\lambda_4$. 33
3.14 Geometry, boundary conditions, and load for clamped box subjected to torque load. 35
3.15 Clamped box under torsional couple for different LSS. Convergence of buckling loads with mesh refinement. The solid line represents h^2 (for reference). 36
3.16 Clamped box under torsional couple with LSS $[45/-45/45/-45/45]_s$. Buckling modes corresponding to buckling loads $\lambda_1 \cdots \lambda_4$. 36

4.1 Square plate under uniaxial compression. Buckling modes corresponding to buckling loads $\lambda_1, \cdots, \lambda_4$. 39
4.2 Square plate ($h \times h$) under uniaxial compression. (a) convergence of buckling loads and (b) convergence of post-critical quartic form. Solid line is for reference. 40
4.3 Square plate under compression. Equilibrium paths recovered using Koiter asymptotic analysis compared with that obtain Riks analysis. The load factor is indicated with λ while w denotes the transversal displacement of the center of the plate. 41
4.4 Hinged cylindrical roof. Geometry, boundary and load condition. 42
4.5 Hinged cylindrical roof. Buckling mode corresponding to buckling load λ_1. 43
4.6 Hinged cylindrical roofs. Equilibrium paths. The load factor is indicated with λ while denotes w (mm) is the transversal displacement of the center of the cylindrical roofs. 43
4.7 Channel section. Geometry, boundary, and load conditions. Dimensions are expressed in mm. 44
4.8 Channel section. Buckling modes corresponding to buckling loads $\lambda_1, \lambda_2, \cdots \lambda_6$. . 45
4.9 Channel section. Equilibrium paths recovered using Koiter asymptotic analysis compared with that obtain Riks analysis. Load factor is indicated with λ and it is normalized on the first buckling load λ_1. In the abscissa are plotted the axial displacement u of the end section and the transversal displacement w at a quarter of the height in the center of the web. 46

5.1 Geometry of RS 125 section (dimensions are expressed in mm) and boundary conditions. 48
5.2 Type of imperfections for numerical analysis (a) distortional and (b) global. . . . 49
5.3 Geometry, boundary conditions of the member, reference point ("A") for displacements. 50
5.4 Detail of mesh for RS 125 x 3.2 section. 50
5.5 Distorsional d_1, d_2 ... d_8 and global e_1, e_2 buckling modes for RSB 125 x 3.2 section in the range $L = 1400$ ... 2500 mm. 52
5.6 Distorsional d_1, d_2 ... d_8 and global e_1, e_2 buckling modes for RSN 125 x 3.2 section in the range $L = 1400$ ... 2500 mm. 53
5.7 Buckling modes for RSB 125 x 3.2 section with $L = 2200$ mm. 53
5.8 Buckling modes for RSN 125 x 3.2 section with $L = 2200$ mm. 54
5.9 Buckling load and corresponding length for RSN 125 x 3.2 section. The length $L = 2200$ mm corresponding to global/distortional interactive buckling has been denoted. 54
5.10 Quadratic corrections for RSB 125 x 3.2 section with $L = 2200$ mm. 55
5.11 Quadratic corrections for RSN 125 x 3.2 section with $L = 2200$ mm. 55
5.12 Equilibrium paths λ versus ξ_i $i = 1 \cdots 4$ for the length $L = 2000$ mm. λ_{min} is the lowest critical load found. 56
5.13 Equilibrium paths λ versus u. λ_{min} is the lowest critical load found. The displacement components u_x, u_y and u_z are measured in the point A. See Fig.5.3. . 56
5.14 Equilibrium paths λ versus ξ_i $i = 1 \cdots 4$ for four lengths. λ_{min} is the lowest critical load found. 57
5.15 Frequency distribution of the limit load found λ_{lim} for the brut section (a) and net section (b). 58

5.16 Section RS 125 x 3.2, brut and net, with length of 2200 mm: (a) initial shapes for worst imperfection amplified by factor 5.0, (b) deformed shapes at limit load for worst imperfection amplified factor 2.5. 59
5.17 (a) Probability distribution functions, for 500 geometric imperfections, corresponding to the investigated length range for RSN 125 x 3.2 section; (b) Probability distribution functions for $L = 2000$ mm for various numbers of imperfections. The values of the parameters of the probability distribution function (eq. (5.4)) are reported in the tables. 60
5.18 Section RSN 125 x 3.2 $L = 1400$ ... 2500 mm: the minimum limit load λ_{lim}^{min} is normalized on the first buckling load for each length. The specimen with maximum erosion is highlighted in red. 60
5.19 Section RS 125 x 3.2 $L = 1400$ ... 2500 mm: Sensitivity curve for the worst imperfection. 61
5.20 Section RSB 125 x 3.2 $L = 1400$ ... 2500 mm: initial shapes for worst imperfection. 62
5.21 Section RSN 125 x 3.2 $L = 1400$ ... 2500 mm: initial shapes for worst imperfection. 63
5.22 Section RSB 125 x 3.2 $L = 1400$ ... 2500 mm: deformed shapes at limit load for worst imperfection. 63
5.23 Section RSN 125 x 3.2 $L = 1400$ ... 2500 mm: deformed shapes at limit load for worst imperfection. 64
5.24 Section RSB 125: Frequency distribution of the limit load found λ_{lim}. 65
5.25 Section RSN 125: Frequency distribution of the limit load found λ_{lim}. 66
5.26 Section RSB 125 $L = 1400$ ... $2500\,mm$: Sensitivity curve for the worst imperfection. 67
5.27 Section RSN 125 $L = 1400$ ... $2500\,mm$: Sensitivity curve for the worst imperfection. 68
5.28 Section RS 125 x 3.2, length $L = 2000$ mm: equilibrium paths λ/λ_{min} versus the displacements u_x for different numbers of buckling modes considered for Koiter's analysis. For each analysis, the worst imperfection in the buckling modes space has been used. 69
5.29 Section RS 125 x 3.2, length $L = 2000$ mm: Yield stress increase due to cold forming ($\%f_y$). 70
5.30 Section RS 125 x 3.2, length $L = 2000$ mm: equilibrium paths λ/λ_{min} versus the displacements u_y using Koiter's and Riks elastic analysis and GMNIA. For each analysis the worst imperfection (see Table5.3) has been used. 70
5.31 Section RS 125 x 3.2 $L = 2000$ mm: (a) deformed shape at limit load for worst imperfection obtained by Koiter approach; (b) deformed shape at limit load for worst imperfection obtained by Riks analysis. 71
5.32 Geometry, boundary conditions, and load for the box in compression. 72
5.33 Buckling modes for the box in compression at $t/a = 1/400$. 72
5.34 Quadratic corrections for the box in compression, with $t/a = 1/400$. 73
5.35 Equilibrium paths λ versus ξ_i, $i = 1...8$ for the box in compression, with $t/a = 1/400$. 74
5.36 Equilibrium paths λ versus u for the box in compression, with $t/a = 1/400$. The displacement component u_x is measured at point A in Fig.(5.32). 74
5.37 Interaction between the first mode (with amplitude ξ_1) and the remaining modes $\xi_j, j = 2..8$. The presence of attractive paths is clear. 75
5.38 Deformed configuration at points A, B and C, labeled in Figure (5.35). 75
5.39 Frequency distribution of the lowest limit load found λ_{lim} for the clamped box in compression and several values of t/a. 75
5.40 Shape of the worst imperfection for the box in compression, with $t/a = 1/400$. . 76

5.41 Mode shape at minimum limit load with the worst imperfection for the box in compression, with $t/a = 1/400$. 76
5.42 Load sensitivity to worst imperfection amplitude $\tilde{u}_{max}/t$ for the box in compression at several values of t/a. 76
5.43 Box beam loaded axially. Geometry, boundary, and load conditions. 77
5.44 Buckling modes for the box beam with L=20 mm, t/a=3/10. 78
5.45 Quadratic corrections for the box beam with L=20 mm, t/a=3/10. 79
5.46 Equilibrium paths λ versus ξ_i (see (1.7e)) for the box beam loaded axially with uniform edge-pressure and simply supported at both ends on skin only, $L = 20$, 40...200 mm, t/a=3/10. Ordinate: λ/λ_{min}. Abscissa: mode amplitudes ξ_i, with $i = 1...4$ denoted by colors orange, grey, yellow, and red, respectively. λ_{min} is the lowest critical load found. 80
5.47 Equilibrium paths λ versus edge displacement u for the box beam loaded axially with uniform edge-pressure and simply supported at both ends on skin only, t/a=3/10. Ordinate: λ/λ_{min}. Abscissa: edge displacement u, for three cases denoted by colors orange, grey, and yellow, corresponding to column length $L = 20, 40, 200$ mm, respectively. λ_{min} is the lowest critical load found. 81
5.48 Frequency distribution of the lowest limit load found λ_{lim} for the box beam loaded axially with uniform edge-pressure and simply supported at both ends on skin only, $L = 20, 40, ...200$ mm; t/a=3/10. 82
5.49 Shapes of the worst imperfection for the box beam loaded axially with uniform edge-pressure and simply supported at both ends on skin only, $L = 20$, 40, 100, 120, 160, 180 mm mm, t/a=3/10. 82
5.50 Mode shapes at minimum limit load with the worst imperfection for the box beam loaded axially with uniform edge-pressure and simply supported at both ends on skin only, $L = 20$, 40, 100, 120, 160, 180 mm, t/a=3/10. 83
5.51 Sensitivity curve using the worst imperfection for the box beam loaded axially with uniform edge-pressure and simply supported at both ends on skin only, $L = 20, 40, 100, 120, 160, 180$ mm, t/a=3/10. 83
5.52 Buckling modes for cylinder Z33 with $R/t = 200$. 85
5.53 Quadratic corrections for cylinder Z33 with $R/t = 200$. 86
5.54 Frequency distribution of the lowest limit load λ_{lim} for cylinders Z32 on the left and Z33 on the right at several values of radius-to-thickness ratios. 86
5.55 Shapes of the worst imperfection for cylinder Z33 at several radius-to-thickness ratios. 86
5.56 Mode shapes at minimum limit load with the worst imperfection for cylinder Z33 and several radius-to-thickness ratios. 87
5.57 Limit load sensitivity to worst imperfection amplitude for cylinders Z32 and Z33 and several radius-to-thickness ratios. 87
5.58 Shapes of the worst imperfection for several cylinders using 1000 geometrical imperfection. 90
5.59 Shapes of the worst deformation for several cylinders using 1000 geometrical imperfection. 91
5.60 Limit load sensitivity to worst imperfection amplitude for cylinders $Z07$, $Z11$, $Z12$, $Z14$, $Z15$, $Z18$, $Z21$, $Z32$, $Z33$ and $Z36$ using 1000 geometrical imperfection. 92
5.61 Limit load sensitivity to worst imperfection amplitude for cylinder $Z07$ and several radius-to-thickness ratios. 92

5.62 Limit load sensitivity to worst imperfection amplitude for cylinder $Z15$ and several radius-to-thickness ratios. 93
5.63 Limit load sensitivity to worst imperfection amplitude for cylinder $Z33$ and several radius-to-thickness ratios. 93
5.64 Limit load sensitivity to worst imperfection amplitude for cylinder $Z36$ and several radius-to-thickness ratios. 94
5.65 Load sensitivity to worst imperfection $\tilde{u}_{max}$ for cylinder Z33 with $R/t = 200$. . . 95

List of Tables

3.1 Percentage error with respect to the analytical solution values [85] on the transversal displacement at point A, bending moments and shear forces at point E, for regular mesh and span-to-thickness ratios on a simply supported square plate [0/90/0] under uniform distributed load. 24

3.2 Percentage error with respect to the analytical solution values [85] on the transversal displacement at point A, bending moments and shear forces at point E, for regular mesh and span-to-thickness ratios on a simply supported square plate [0/90] under uniform distributed load. 30

3.3 Percentage error with respect to the analytical solution values [85] on the transversal displacement at point A, bending moments at points A, C, shear forces at point B and membrane stress resultant at point C, for regular mesh and span-to-thickness ratios on a simply supported square plate $[-45/45]$ under uniform distributed load. 32

3.4 Percentage error with respect to the analytical solution values [85] on the transversal displacement at point A, bending moments at point A and shear force at point D, for regular mesh and span-to-thickness ratios on a simply supported square plate $[30/-60/60/-30]$ under uniform distributed load. 34

3.5 Square plate $[0/90/90/0]_S$ under uniaxial compression. Convergence of buckling loads with mesh refinement. 34

3.6 Clamped beam C-section for different LSS. Convergence of buckling loads with mesh refinement. The values on the first column refer to the numbers of the element along b. 35

3.7 Clamped box under torsional couple for different LSS. Convergence of buckling loads with mesh refinement. The values on the first column refer to the numbers of the element along a. 37

4.1 Square plate under uniaxial compression. Convergence of buckling loads with mesh refinement. 39

4.2 Koiter's vs Riks analysis timing 42

5.1 The first four buckling loads corresponding to the investigated length range for RSB 125 x 3.2 section. The buckling loads are expressed in kN. The buckling modes specified by letters d (d_1, d_2 ... d_8) and e (e_1, e_2) are respectively distorsional and global. The abbreviations S, A, F and FT indicate respectively: symmetric, antisymmetric, flexural and flexural torsional (see Fig. 5.5). 51

5.2 The first four buckling loads corresponding to the investigated length range for RSN 125 x 3.2 section. The buckling loads are expressed in kN. The buckling modes specified by letters d (d_1, d_2 ... d_8) and e (e_1, e_2) are respectively distorsional and global. The abbreviations S, A, F and FT indicate respectively: symmetric, antisymmetric, flexural and flexural torsional (see Fig. 5.6). 52
5.3 Participation of buckling modes in worst imperfection in percentage (%) corresponding to the investigated length range for RSN 125 x 3.2 section. The buckling modes are normalized as reported in Eq. **??**. The sign in brackets indicates how the mode is accounted for with respect to the normalization. 58
5.4 Section RS 125 x 3.2 $L = 1400$ ... 2500 mm: Computational costs. N_v denotes the numbers of variables. 61
5.5 Section RS 125 x 3.2, length $L = 2000$ mm: λ_{lim}^{min} and λ_{lim}^{max} for varying numbers of buckling modes accounted for in Koiter's analysis. 69
5.6 Buckling loads (in Newtons) for the box in compression at several t/a ratios. . . 72
5.7 Buckling loads (in Newtons) for the box beam loaded axially. The used mesh for the analysis is reported in Fig. 5.43. 78
5.8 Buckling loads (in kN) for cylinder Z32 as a function of radius/thickness ratio. . 85
5.9 Buckling loads (in kN) for cylinder Z33 as a function of radius/thickness ratio. . 85
5.10 Geometrical and mechanical parameters for the cylinders analyzed. 88
5.11 The LSS for each cylinder analyzed. 88
5.12 Buckling loads (in kN) for the cylinders $Z07$, $Z11$, $Z12$, $Z14$, $Z15$, $Z18$, $Z21$ and $Z36$. 88
5.13 Buckling loads (in kN) for the cylinders $Z15$ as a function of R/t. 89
5.14 Buckling loads (in kN) for the cylinders $Z33$ as a function of R/t. 89
5.15 Tthe cylinders $Z36$ as a function of R/t 89
5.16 Computational cost for cylinder Z33 and several radius-to-thickness ratios. The cost refers to the solution of equation (1.7h). 95

Introduction

The design of composite structures is most often dominated by buckling [1, 2]. For example, the demands for fuel efficiency is prompting the aircraft industry to revolutionize airframe construction to save weight, and thus fuel. A promising concept is to let the airframe operate in the postbuckling regime, where the skin of the composite stiffened panels are allowed to buckle in normal flight conditions. This hinges upon the assumption that stiffened panels, and thus the entire airframe, are imperfection insensitive.

Imperfection sensitivity analysis requires the identification of a large number of buckling modes and their interaction. Because of the large number of possible modes and our a priori ignorance about which ones would interact with each other, such analysis is prohibitively time consuming. Continuation methods based on Riks scheme are often used [3]. In spite of the simplicity of its numerical implementation, which requires only an approximation of the tangent stiffness matrix, the method suffers in the case of multiple bifurcations, requiring ad-hoc branch switch algorithms [4]. Continuation methods are time consuming, requiring a lengthy analysis for each assumed imperfection. Furthermore, type and shape of imperfections are unknown, either because the structure is in the design stage or because it is too difficult to measure them.

Therefore, the aim of this work is to propose a robust and efficient methodology to calculate the imperfection sensitivity of laminated composite folded plates. The proposed methodology does not require a priori knowledge of the shape and magnitude of imperfections and does not rely on lengthy continuation analysis. Instead, it uses Koiter's perturbation approach [5, 6] to calculate the bifurcation load, post-buckling path, and interaction between modes to detect bifurcations on the post-buckling path of individual modes, as well as the paths emanating from those bifurcations. The requirement for linearity of the constitutive equations is easily met by composite materials, which have a broad, linear stress and strain range of operation in compression [7].

The most recent implementations of Koiter's approach include spatial beam assemblages [8], folded plates [9, 10], and composite structures [11]. Since the approach is based on fourth-order energy expansion [8], a finite element capable of accurately representing fourth-order terms is

required for robustness of the analysis. The corotational approach [12, 13] fulfils this requirement allowing the complete reuse of a linear element for geometrically nonlinear analysis. A mixed formulation is used to avoid extrapolation locking [14]. The recent 3D plate finite element [15] based on Hellinger-Reissner variational formulation guarantees an accurate evaluation of linear elastic response and of rotation fields [16], so it is very suitable to be used with a corotational formulation to obtain a geometrically nonlinear formulation, which is accurate up to fourth order energy terms [11].

Koiter's method provides robust prediction of the path emanating form interaction bifurcations between three or more modes, thus providing a good estimate of the imperfection sensitive, post-buckling trajectory (even when the shape and magnitude of the imperfections are unknown) that otherwise would be very costly to follow by a continuation methods. Mode interaction often produces the most deleterious imperfection sensitive path with the larger drop in load carrying capacity [18, 19, 20]. The difficulty resides on how to select the set of modes that produces the worst behavior.

The Monte Carlo method is proposed herein to find the modes that yield the most unfavorable, imperfection sensitive path. Although Monte Carlo is an expensive method, the computational cost is keep low thanks to the efficiency of both the element used and Koiter's approach. Also, Koiter's approach is quite demanding about the quality of higher order (up to 4th order) derivatives of the energy, but the element formulation used in this work is uniquely suited to satisfy those demands for accuracy at a low computational cost. The proposed methodology allows us to run thousand of analysis in a few seconds, obtaining the worst imperfection using a Monte Carlo simulation.

Chapter 1

Koiter's asymptotic approach

1.1 Introduction

The starting point for the analysis of slender elastic structures is the total potential energy $\Pi[u]$, where u are the configuration variables. In particular we have

$$\Pi[u] = \Phi[u] - \lambda p u \tag{1.1}$$

with $\Phi[u]$ the strain energy, λ the load control parameter and p the applied load. The solution of the problem requires solving the nonlinear problem

$$\Pi'[u]\delta u = \Phi'[u]\delta u - \lambda p \delta u = 0 \quad \forall \delta u \tag{1.2}$$

where the prime denotes the Frèchet derivative with respect to u. Using a Finite Element technique, Eq. 1.2, can be rewritten as

$$\delta \boldsymbol{u}^T \boldsymbol{r}[\boldsymbol{u}, \lambda] = 0 \quad \forall \delta \boldsymbol{u} \qquad \boldsymbol{r}[\boldsymbol{u}, \lambda] = (\boldsymbol{s}[\boldsymbol{u}] - \lambda \boldsymbol{p}) \tag{1.3}$$

with $u = \mathcal{L}\boldsymbol{u}, p = \mathcal{L}\boldsymbol{p}$ with $\mathcal{L}$ the interpolation operator, $\boldsymbol{s}[\boldsymbol{u}]$ the structural response and $\boldsymbol{p}$ the load vector. The solution of Eq. 1.3 and then the equilibrium path can be obtained using the path-following approach and asymptotic approach. In the former, the equilibrium path is obtained as a sequence of equilibrium points

$$\{(\boldsymbol{u}_0, \lambda_0), (\boldsymbol{u}_1, \lambda_1), ...(\boldsymbol{u}_i, \lambda_i)\} \quad i = 0, 1..n \tag{1.4}$$

using an iterative scheme based on the Newton-Raphson method or its modifications [3]. The Path-following approach is widely used as a solution scheme because of its ease of implementation and its robustness. Its disadvantages are the computational cost that is directly related to the numbers of variables of Finite Element discretization (i.e. the dimension $\boldsymbol{u}$); the need to perform an analysis for each load case even in the case of small modifications (i.e. in the case of imperfections) of the load and the difficulties that arise in the case of multiple and near coincident buckling modes.

On the other hand, in the asymptotic analysis the equilibrium path is obtained in an approximate fashion through an asymptotic expansion with respect to the expansion parameters $\xi_i, i = 0..m$ red,

$$\begin{cases} \boldsymbol{u} = \boldsymbol{u}_0 + \sum_{i=0}^{n} \xi_i \dot{\boldsymbol{u}}_i + \frac{1}{2} \sum_{i,j=0}^{m} \xi_i \xi_j \ddot{\boldsymbol{u}}_{ij} + \cdots + \mathcal{O}(\xi_i^k) \\ \lambda = \lambda_0 + \sum_{i=0}^{n} \xi_i \dot{\lambda}_i + \frac{1}{2} \sum_{i,j=0}^{m} \xi_i \xi_j \ddot{\lambda}_{ij} + \cdots + \mathcal{O}(\xi_i^k) \end{cases} \tag{1.5}$$

denoting with $(\cdot)$ the derivation with respect to ξ. The nonlinear system of equation 1.3, can be rewritten as

$$\boldsymbol{r}[\boldsymbol{\xi}, \lambda] = \boldsymbol{0} \tag{1.6}$$

with $\boldsymbol{\xi}$ the vector collecting the ξ_i expansion parameters. The nonlinear system Eq. 1.6 has in general a reduced number of variables. In practical contexts m is of the order of tens. Moreover, as further explained in the next section once having recovered the terms of the Eq. 1.5, i.e. the so-called 'perfect structure', all deviations of the assumed load (i.e. load imperfections), geometrical or other kind of imperfections, i.e. loads applied eccentrically, require only the solution of equation 1.6. This is a great advantage of the method because the nonlinear system has a reduced dimension and so allows the easy testing of the effect of thousands of imperfections with very low computational cost.

In the next section, a summary of the FE asymptotic analysis proposed by Casciaro et al. [6] is presented. The described implementation is also called *quadratic algorithm*.

1.2 Foundamental equations

Asymptotic analysis is essentially the implementation of Koiter's nonlinear elastic stability approach [5] into the finite element method (FEM) [6]. The solution process is based on an expansion of the potential energy Φ in terms of load factor λ and modal amplitudes ξ_i. It can be summarized as follows:

i.. The *fundamental path* is obtained as a linear extrapolation

$$\boldsymbol{u}^f[\lambda] = \boldsymbol{u}_0 + \lambda\hat{\boldsymbol{u}} \tag{1.7a}$$

where $\boldsymbol{u}_0$ is an initial displacement, possibly null, and $\boldsymbol{u} = \lambda\hat{\boldsymbol{u}}$ is the vector of kinematic parameters, i.e., the space of *degrees of freedom (dof)* of the structure, and $\widehat{\boldsymbol{u}} = d\boldsymbol{u}/d\lambda$ is obtained as the solution of the linear algebraic equation

$$\boldsymbol{K}_0\,\hat{\boldsymbol{u}} = \hat{\boldsymbol{p}} \tag{1.7b}$$

where $\hat{\boldsymbol{p}}$ is the reference load and $\boldsymbol{K}_0 = \boldsymbol{K}[\boldsymbol{u}_0]$ is the stiffness matrix, which contains the coefficients of the quadratic terms of the energy Φ''.

ii.. A cluster of *buckling loads* λ_i, $i = 1\cdots m$, and associated *buckling modes* $\dot{\boldsymbol{v}}_i$ are obtained along $\boldsymbol{u}^f[\lambda]$ by the critical condition

$$\boldsymbol{K}[\lambda_i]\,\dot{\boldsymbol{v}}_i = \boldsymbol{0} \quad , \quad \boldsymbol{K}[\lambda] = \boldsymbol{K}[\boldsymbol{u}_0 + \lambda\hat{\boldsymbol{u}}] \tag{1.7c}$$

the eigenvalue problem is defined as fully nonlinear, to correctly recover the post-critical behavior. The nonlinearity is introduced by updating the configuration along the fundamental path.

Note that the size m of the subspace of buckling modes needed for the analysis is orders of magnitude smaller than the number of dof used to discretize the structure, often as little as $m = 3$.

We denote by $\mathcal{V} = \{\dot{\boldsymbol{v}} = \sum_{i=1}^{m} \xi_i\dot{\boldsymbol{v}}_i\}$ the subspace spanned by the buckling modes $\dot{\boldsymbol{v}}_i$ (where ξ_i are the modal amplitudes) and by $\mathcal{W} = \{\boldsymbol{w} : \boldsymbol{w}\perp\dot{\boldsymbol{v}}_i\,,\ i = 1\cdots m\}$ its orthogonal complement, defined by the orthogonality condition

$$\boldsymbol{w}\perp\dot{\boldsymbol{v}}_i \ \Leftrightarrow\ \Phi_b'''\hat{u}\dot{v}_i w = 0 \tag{1.7d}$$

where $\hat{u} = \mathcal{L}\hat{\boldsymbol{u}}$, $\dot{v}_i = \mathcal{L}\dot{\boldsymbol{v}}_i$, $w = \mathcal{L}\boldsymbol{w}$ and $\mathcal{L}$ is the linear operator of FEM interpolation.

We denote by λ_b an appropriate reference value for the cluster, e.g. the smallest of λ_i or their mean value. Accordingly, a suffix "b" denotes quantities evaluated in correspondence to $\boldsymbol{u}_b = \boldsymbol{u}^f[\lambda_b]$.

iii.. Defining $\xi_0 = (\lambda - \lambda_b)$ and $\dot{\boldsymbol{v}}_0 = \hat{\boldsymbol{u}}$, the asymptotic approximation for any equilibrium path

is approximated by a expansion in terms of mode amplitudes ξ_k as follows

$$\boldsymbol{u}[\lambda,\xi_k] = \boldsymbol{u}_b + \sum_{i=0}^{m} \xi_i \dot{\boldsymbol{v}}_i + \frac{1}{2}\sum_{i,j=0}^{m} \xi_i\xi_j \boldsymbol{w}_{ij} \tag{1.7e}$$

where $\boldsymbol{w}_{ij} \in \mathcal{W}$ are quadratic corrections introduced to satisfy the projection of the equilibrium equation (see[21, Section 3.3]) into $\mathcal{W}$, obtained by the linear *orthogonal equations*

$$\delta\boldsymbol{w}^T(\boldsymbol{K}_b\boldsymbol{w}_{ij} + \boldsymbol{p}_{ij}) = 0\ , \quad \forall \boldsymbol{w} \in \mathcal{W} \tag{1.7f}$$

where $\boldsymbol{K}_b = \boldsymbol{K}[\boldsymbol{u}^f[\lambda_b]]$ and vectors $\boldsymbol{p}_{ij}$ are defined as a function of modes $\dot{\boldsymbol{v}}_i\ ;\ i = 0\cdots m$, by the energy equivalence $\delta\boldsymbol{w}^T\boldsymbol{p}_{ij} = \Phi_b'''\delta w\, \dot{v}_j\dot{v}_j$.

iv.. The following energy terms are computed for $i,j = 0\cdots m$, $k = 1\cdots m$:

$$\begin{aligned}
\mathcal{A}_{ijk} &= \Phi_b'''\dot{v}_i\dot{v}_j\dot{v}_k \\
\mathcal{B}_{ijhk} &= \Phi_b''''\dot{v}_i\dot{v}_j\dot{v}_h\dot{v}_k - \Phi_b''(w_{ij}w_{hk} + w_{ih}w_{jk} + w_{ik}w_{jh}) \\
\mathcal{C}_{ik} &= \Phi_b''w_{00}w_{ik} \\
\mu_k[\lambda] &= \frac{1}{2}\lambda_b(\lambda - \frac{1}{2}\lambda_b)\Phi_b'''\hat{u}^2\dot{v}_k + \frac{1}{6}\lambda_b^2(\lambda_b - 3\lambda)\Phi_b''''\hat{u}^3\dot{v}_k
\end{aligned} \tag{1.7g}$$

where the *implicit imperfection factors* μ_k are defined by the 4th order expansion of the unbalanced work on the fundamental path, i.e., $\mu_k[\lambda] = (\lambda\hat{p} - \Phi'[\lambda\hat{u}])\dot{v}_k$ (see [21, Eqs.(31,32)]).

v.. The equilibrium path is obtained by projecting the equilibrium equation [21, Section 3.4] on $\mathcal{V}$. According to eqs, (1.7a)–(1.7g), we have

$$\frac{1}{2}\sum_{i,j=0}^{m} \xi_i\xi_j\mathcal{A}_{ijk} + \frac{1}{6}\sum_{i,j,h=0}^{m} \xi_i\xi_j\xi_h\mathcal{B}_{ijhk} + \mu_k[\lambda] - \lambda_b(\lambda - \frac{1}{2}\lambda_b)\sum_{i=0}^{m}\xi_i\mathcal{C}_{ik} = 0\ , \quad k = 1\ldots m \tag{1.7h}$$

Equation (1.7h) is an algebraic nonlinear system of m equations in the $m+1$ variables $\xi_0, \xi_1\cdots\xi_m$, with known coefficients.

The accuracy of equilibrium equation Eq. 1.7h requires that the mechanical behaviour of the structure is adequately represented by a 4th-order energy expansion. Furthermore, it is also related to the local linearization of the critical equation which implies $(\lambda_i - \lambda_b) << 1 \quad \forall\lambda_i$. This can be assumed in the case of nearly coincident buckling modes or in the case of linear pre-critical buckling modes as generally occurs in compressed members. However the equation has also been tested for distant buckling modes in the case of nonlinear pre-critical in paper [9] where the recovered equilibrium path shows great accuracy compared with path-following solution.

The implementation of the asymptotic approach is quite easy and its computational cost remains of the order of that required by a linear buckling analysis [6]. Once the preprocessor phase of the analysis has been performed (steps i. to iv.), the presence of imperfections can be taken into account in step 5, by adding additional imperfection terms in the expression for $\mu_k[\lambda]$, allowing for an inexpensive imperfection sensitivity analysis.

1.3 Imperfection sensitivity analysis

The geometry and loads of thin-walled structures are affected by random distribution of small *imperfections*. In the proposed asymptotic method, the presence of small imperfections expressed by a load $\tilde{p}[\lambda]$ and/or an initial displacement $\tilde{u}$ affect Eq.(1.7g) only on the imperfection term $\mu_k[\lambda]$ that becomes [6]

$$\mu_k[\lambda] = \frac{1}{2}\lambda_b(\lambda - \frac{1}{2}\lambda_b)\Phi_b'''\hat{u}^2\dot{v}_k + \frac{1}{6}\lambda_b^2(\lambda_b - 3\lambda)\Phi_b''''\hat{u}^3\dot{v}_k + \mu_k^g[\lambda] + \mu_k^l[\lambda] \tag{1.8}$$

with

$$\mu_k^g[\lambda] + \mu_k^l[\lambda] = \lambda\left(\Phi_c'''\hat{u}\tilde{u}\dot{v}_k - \tilde{p}[\lambda]\dot{v}_k\right) = \lambda\bar{\mu}_k \tag{1.9}$$

The aim of the *imperfection sensitivity analysis* is to link the presence of geometrical and load imperfections to the reduction of the limit load. For structures presenting coupled buckling modes, even a small load or geometrical imperfection may result in a marked reduction of the limit load with respect to the bifurcation load [27, 28, 29, 30, 31, 32]. Therefore, an effective safety analysis should include an investigation of all possible imperfection shapes and sizes to recover the *worst case imperfection* (see [33]).

The asymptotic approach provides a powerful tool for performing this extensive investigation. In fact, the analysis for a different imperfection only needs to update the imperfection factors $\mu_k^g[\lambda]$ and $\mu_k^l[\lambda]$ through Eq.(1.8)–(1.9) and solve the nonlinear system (1.7g)–(1.7h). Even if this system, which collects all the nonlinear parts of the original problem, proves to be highly nonlinear and some care has to be taken in treating the occurrence of multiple singularities, its solution through a path–following process is relatively easy because of the small number m of unknowns involved.

Chapter 2

Corotational Formulation

2.1 Introduction

Asymptotic analysis exploits a fourth–order expansion of the strain energy and so it requires that the energy expression is characterized by fourth–order accuracy at least. Satisfying this requirement exactly is not an easy task. In fact, the usual plate and shell theories (the so called "technical theories") and current finite element (FE) technologies only provide second order accuracy exactly and third order one with some approximations [34]. This introduces an objectivity error into the element description, i.e. a non rational dependence of the strain energy on the rigid body motion, which can lead to a poor recovery of the post–buckling behavior of the structure at increasing displacements. At the moment, various proposals for the FE asymptotic analysis of shells [34] suffer from this inconvenience, even if in some cases (e.g. when the post–buckling behavior is largely dominated by stress redistribution, as discussed in [35]) the approximation made can be considered as acceptable.

The corotational formulation, as devised for example in [36, 37], provides an effective general tool for performing fully objective, geometrically nonlinear finite element analysis. The use of a local reference frame, moving with the element, allows the rigid body motion from the description of the element internal deformations to be filtered and, so, decouple the geometrical nonlinearity from the elastic response. In this way, the element response can be described, in the local frame, using the standard linear theory. A remarkable contribution to the corotational approach was [38]. Its main advantage lies in its ability to fully exploit the existing FE technology available for linear analysis. Corotational algebra, that is algebra expressing the reference change between a global fixed frame and the local moving element frames, as shown in [8], reduces to standard algebraic procedures and recursive formulas expressing corotational derivatives can be obtained in explicit form.

The corotational approach to asymptotic analysis was investigated in [8] with reference to 3D assemblages of beams, by Zagari et al. [9] with reference to shell structures and by Barbero et al. [11] with reference to composites shell structures. The resulting solution procedure is really effective and offers a robust tool to capture the pre- and post-buckling nonlinear behavior in a way which is both qualitatively correct and quantitatively accurate. In addition, it is computationally convenient with respect to path-following analysis, since imperfection sensitivity analysis can be carried out very effectively.

Folded laminated plates are widely used in the form of structural profiles [39, Fig. 10.1], stiffened panels [39, Section 11.3], cellular structures [40] and so on. Open or closed sections composed of flat walls are attractive because they maximize the bending and torsional stiffness for minimum weight and at the same time they take advantage of the high strength of fiber reinforced materials. Using laminated panels affords high flexibility to the design by virtue of the broad range of stiffness and strength that can be imparted to the walls. Ever increasing demands for lightweight structures for transportation vehicles of all kinds requires the use of optimized thin-walled structures for which buckling become the design constraint. Accurate computation of buckling loads, modes, mode interaction [19], and imperfection sensitivity [22, 23] is thus required. Since these calculations are computationally intensive, there is significant interest in developing accurate yet economical simulation methods. The use of corotational formulation is quite attractive in this regard because it allows for simple extension to nonlinear analysis of proven, accurate, computationally efficient linear analysis elements.

A linear, mixed formulation element called MISS-4 is used as starting point for this work [15]. The stress resultant interpolation, which accounts for the average distortion of the element, is self-equilibrated and isostatic. Only 18 stress parameters are used into 6 constant, 8 linear, and 4 quadratic stress shape functions. The kinematics uses 6 degrees of freedom (dof) per node for an overall 24 dof. Convergence rate and accuracy is shown in this work to be comparable to that of 48 dof, displacement based elements such as Abaqus S8R.

The performance of the linear element has been shown to be very good for the case of isotropic material, both for the recovery displacements and rotations as well as for evaluation of stress resultants. Numerical results, show s-norm h^2 convergence rate [70]. Furthermore, the element is free from locking. The element matrices are evaluated analytically along the contour. Moreover, the element uses 6 standard degrees of freedom (dof) per node (3 displacements and 3 rotations), thus allowing for trivial implementation as a user element into commercial codes [15, 58].

In this work, the drilling rotations are implemented as per [24, 25], without un-symmetric formulation or penalty constraints [26], allowing for an accurate recovery of drilling rotation field; thus enabling the element to be used for geometrically nonlinear analysis using a corotational

formulation [8, 12, 13, 9, 11]. An incompatible cubic mode is used to eliminate the spurious zero energy mode [16].

A review paper [60] describes the most recent available finite elements based on various laminated theories for buckling and post-buckling, free vibration, dynamics, failure, and damage. Similarly, [61] offers an overview on different strategies for modeling laminated composites plates. Recently proposed elements range from assumed displacements [62, 63], mixed and hybrid formulations [64, 65, 66, 68, 69], mixed interpolation of tensorial components (MITC) [71, 72], NURBS-based isogeometric elements [73], radial point interpolation [74], thickness-stretch deformation elements [75] and zigzag elements in nonlinear context [76]. Comparison between various laminated composite plate and finite element results is provided in [77].

For this work, the laminate kinematics has been approximated by first order shear deformation theory (FSDT) [85, 42], which offers a good compromise between simplicity and accuracy in the recovery of displacements, rotations, and stress resultants. Furthermore, the mixed stress-displacement formulation chosen for this work allows for better recovery of stress profiles than displacement-only formulations [82, 83].

2.2 Geometrically linear formulation

As it was stated earlier, the formulation must be capable of accurate representation of fourth-order terms on the potential energy. Therefore, we start with a mixed formulation. The initial reference configuration of the element is flat and referred to a local Cartesian frame $\{\boldsymbol{e}_1, \boldsymbol{e}_2, \boldsymbol{e}_3\}$. Furthermore, $\{x, y\}$ is a vector lying on the middle surface Ω defined by the unit vectors $\{\boldsymbol{e}_1, \boldsymbol{e}_2\}$, s is the thickness along the $\boldsymbol{e}_3$ direction, and Γ is the boundary of Ω. On this frame, the Hellinger-Reissner strain energy for a flat shell can be written as

$$\begin{aligned} \Phi[\boldsymbol{t}, \boldsymbol{d}] &= \int_\Omega \left\{ \boldsymbol{t}^T \boldsymbol{D} \boldsymbol{d} - \frac{1}{2} \boldsymbol{t}^T \boldsymbol{E}^{-1} \boldsymbol{t} \right\} \mathrm{d}\Omega \\ \boldsymbol{t} = \begin{bmatrix} \boldsymbol{t}_m \\ \boldsymbol{t}_f \end{bmatrix}, \quad \boldsymbol{d} &= \begin{bmatrix} \boldsymbol{d}_m \\ \boldsymbol{d}_f \end{bmatrix}, \quad \boldsymbol{D} = \begin{bmatrix} \boldsymbol{D}_m & \boldsymbol{0} \\ \boldsymbol{0} & \boldsymbol{D}_f \end{bmatrix} \end{aligned} \tag{2.1}$$

where $\boldsymbol{t}_m, \boldsymbol{t}_f$ are the in- and out-of-plane stress parameters, respectively; and $\boldsymbol{d}_m, \boldsymbol{d}_f$ are the in- and out-plane kinematical parameters, defined as follows

$$\boldsymbol{t}_m = \begin{bmatrix} N_x \\ N_y \\ N_{xy} \end{bmatrix} \quad , \quad \boldsymbol{t}_f = \begin{bmatrix} M_x \\ M_y \\ M_{xy} \\ S_x \\ S_y \end{bmatrix} \quad , \quad \boldsymbol{d}_m = \begin{bmatrix} d_x \\ d_y \end{bmatrix} \quad , \quad \boldsymbol{d}_f = \begin{bmatrix} d_z \\ \varphi_x \\ \varphi_y \end{bmatrix} \tag{2.2}$$

where $\boldsymbol{N}, \boldsymbol{M}, \boldsymbol{S}$ are the membrane, bending, and shear stress resultants, respectively; and $\boldsymbol{d}, \boldsymbol{\varphi}$ are the midsurface strains and rotations, respectively.

Using first-order shear deformable theory (FSDT) [42], the differential operators $\boldsymbol{D}_m$ and $\boldsymbol{D}_f$ are defined as

$$\boldsymbol{D}_m = \begin{bmatrix} \partial/\partial x & 0 \\ 0 & \partial/\partial y \\ \partial/\partial y & \partial/\partial x \end{bmatrix} \quad , \quad \boldsymbol{D}_f = \begin{bmatrix} 0 & 0 & -\partial/\partial x \\ 0 & \partial/\partial y & 0 \\ 0 & \partial/\partial x & -\partial/\partial y \\ \partial/\partial x & 0 & 1 \\ \partial/\partial y & -1 & 0 \end{bmatrix} \tag{2.3}$$

The constitutive matrix for a laminate with n layers can be written as

$$\boldsymbol{E} = \begin{bmatrix} \boldsymbol{E}_m & \boldsymbol{E}_{mb} & \boldsymbol{0} \\ & \boldsymbol{E}_b & \boldsymbol{0} \\ \text{sym.} & & \boldsymbol{E}_s \end{bmatrix} \tag{2.4}$$

where

$$\begin{aligned} \boldsymbol{E}_m &= \sum_k^n (z_k - z_{k-1}) \boldsymbol{E}_m^{(k)} \\ \boldsymbol{E}_{mb} &= \frac{1}{2} \sum_k^n (z_k^2 - z_{k-1}^2) \boldsymbol{E}_m^{(k)} \\ \boldsymbol{E}_b &= \frac{1}{3} \sum_k^n (z_k^3 - z_{k-1}^3) \boldsymbol{E}_m^{(k)} \\ \boldsymbol{E}_s &= \boldsymbol{\kappa} \odot \sum_k^n (z_k - z_{k-1}) \boldsymbol{E}_s^{(k)} \end{aligned} \tag{2.5}$$

where z_k, z_{k-1} are the top and bottom coordinates of k-th lamina, respectively, $\boldsymbol{E}_m^{(k)}, \boldsymbol{E}_s^{(k)}$ are the lamina constitutive matrices referring to in-plane and transverse stress/strain, respectively

[42] and [39, Eq.(6.16)]. Finally, symbol $\odot$ denotes the component product (.* in [43]) that allows us to introduce different shear correction factors for each component of the $\boldsymbol{E}_s$ matrix [65, 66, 44]

$$\boldsymbol{\kappa} = \begin{bmatrix} \kappa_{11} & \kappa_{12} \\ \kappa_{12} & \kappa_{22} \end{bmatrix} \tag{2.6}$$

When the stress resultants are defined so that the equilibrium equations are satisfied with zero load, the following identity holds [45]

$$\int_\Omega \boldsymbol{t}^T \boldsymbol{D} \boldsymbol{d}\, \mathrm{d}\Omega = \int_\Gamma \boldsymbol{t}^T \boldsymbol{N}^T \boldsymbol{d}\, \mathrm{d}\Gamma = \int_\Gamma \boldsymbol{t}_m^T \boldsymbol{N}_m^T \boldsymbol{d}_m\, \mathrm{d}\Gamma + \int_\Gamma \boldsymbol{t}_f^T \boldsymbol{N}_f^T \boldsymbol{d}_f\, \mathrm{d}\Gamma \tag{2.7}$$

where $\boldsymbol{N}$ is the matrix collecting the components of the unit outward normal to the contour Γ, that can be split into membrane $\boldsymbol{N}_m$ and bending $\boldsymbol{N}_f$ parts

$$\boldsymbol{N} = \begin{bmatrix} \boldsymbol{N}_m & \boldsymbol{0} \\ \boldsymbol{0} & \boldsymbol{N}_f \end{bmatrix} \tag{2.8}$$

2.2.1 Mixed finite element

Assuming a mixed interpolation for the stress resultants and displacements, a discrete expression for the Hellinger–Reissner mixed strain energy (2.1) can be evaluated. In general, the mixed interpolation can be written as

$$\boldsymbol{t} = \boldsymbol{B}\boldsymbol{t}_e \quad , \quad \boldsymbol{d} = \boldsymbol{U}\boldsymbol{d}_e \tag{2.9}$$

where $\boldsymbol{B}$ is the matrix collecting the assumed stress modes, $\boldsymbol{t}_e$ is the vector of stress parameters, $\boldsymbol{U}$ is the matrix of the displacement shape functions and $\boldsymbol{d}_e$ is the vector of displacement and rotation kinematical parameters. Substituting (2.9) into (2.1) and integrating on the element domain Ω_e leads to the evaluation of the element mixed energy

$$\Phi_e[\boldsymbol{t}_e, \boldsymbol{d}_e] = \boldsymbol{t}_e^T \boldsymbol{D}_e \boldsymbol{d}_e - \frac{1}{2} \boldsymbol{t}_e^T \boldsymbol{H}_e \boldsymbol{t}_e \quad , \quad \begin{cases} \boldsymbol{D}_e = \displaystyle\int_{\Omega_e} \left\{ \boldsymbol{B}^T \boldsymbol{D} \boldsymbol{U} \right\} \mathrm{d}\Omega \\ \boldsymbol{H}_e = \displaystyle\int_{\Omega_e} \left\{ \boldsymbol{B}^T \boldsymbol{E}^{-1} \boldsymbol{B} \right\} \mathrm{d}\Omega \end{cases} \tag{2.10}$$

where $\boldsymbol{D}_e$ and $\boldsymbol{H}_e$ are the compatibility and flexibility matrices, respectively [46], [49].

When the assumed stress modes (shape functions) are chosen so that the stress resultants identically satisfy equilibrium equations with zero load (self equilibrating stress field in the element), the compatibility matrix can be evaluated on the element contour Γ_e, i.e., Eq. (2.7) yields

$$\boldsymbol{D}_e = \int_{\Gamma_e} \boldsymbol{B}^T \boldsymbol{N}^T \boldsymbol{U}\, \mathrm{d}\Gamma \tag{2.11}$$

Applying static condensation to the stress parameters $\boldsymbol{t}_e$, the element energy can be evaluated solely in terms of kinematic parameters $\boldsymbol{d}_e$, and using (2.11), the displacements and rotations, need to be interpolated only along the contour. Details of the element implementation are given in §2.4.

2.3 Geometrically non linear formulation

A linear finite element can be made geometrically nonlinear using corotational algebra to describe the rigid body motion [8]. Following the original proposal by Rankin et. al [36, 37], this framework is still used [51, 52, 53, 54, 55, 56]. With respect to the fixed frame $\{\boldsymbol{e}_1, \boldsymbol{e}_2, \boldsymbol{e}_3\}$, a corotational (CR) frame $\{\bar{\boldsymbol{e}}_1, \bar{\boldsymbol{e}}_2, \bar{\boldsymbol{e}}_3\}$ is defined as

$$\bar{\boldsymbol{e}}_k = \boldsymbol{Q}[\boldsymbol{\alpha}]\boldsymbol{e}_k, \quad k = 1..3 \tag{2.12}$$

with $\boldsymbol{Q}$ being a rigid rotation, parametrized by the rotation vector $\boldsymbol{\alpha}$ according to Rodrigues' formulation [57] (see Fig. 2.1) . The origin is assumed to be translated by vector $\boldsymbol{c}$. Denoting by $\boldsymbol{d}$ and $\boldsymbol{R}$ the displacement and the rotation associated to position $\boldsymbol{X}$ in the fixed reference frame, the following geometrical relationships hold

$$\bar{\boldsymbol{d}} = \boldsymbol{Q}^T(\boldsymbol{X} + \boldsymbol{d} - \boldsymbol{c}) - \boldsymbol{X} \quad , \quad \bar{\boldsymbol{R}} = \boldsymbol{Q}^T\boldsymbol{R} \tag{2.13}$$

with $\bar{\boldsymbol{d}}$ and $\bar{\boldsymbol{R}}$ being the displacement and the rotation in the corotational frame. Using a vector parametrization for $\bar{\boldsymbol{R}}$ and $\boldsymbol{R}$ and denoting by $\bar{\boldsymbol{\psi}}$ and $\boldsymbol{\psi}$ the rotation vectors, we have

$$\bar{\boldsymbol{\psi}} = \log(\bar{\boldsymbol{R}}[\bar{\boldsymbol{\psi}}]) = \log\left(\boldsymbol{Q}^T[\boldsymbol{\alpha}]\boldsymbol{R}[\boldsymbol{\psi}]\right) \tag{2.14}$$

A CR frame can be defined for each element through the element rotation vector $\boldsymbol{\alpha}_e$ which is a function of the element kinematical parameters $\boldsymbol{d}_e$ in the fixed frame

$$\boldsymbol{\alpha}_e = \boldsymbol{\alpha}_e[\boldsymbol{d}_e] \tag{2.15}$$

The local kinematical parameters $\bar{\boldsymbol{d}}_e$ in the CR frame are related to $\boldsymbol{d}_e$ by the geometrical transformation

$$\bar{\boldsymbol{d}}_e = \boldsymbol{g}[\boldsymbol{d}_e] \tag{2.16}$$

where $\boldsymbol{g}$ collects the CR transformations for displacements (2.13) and rotations (2.14) opportunely rearranged in terms of the local kinematical parameters $\bar{\boldsymbol{d}}_e$ of the finite element. See [9]

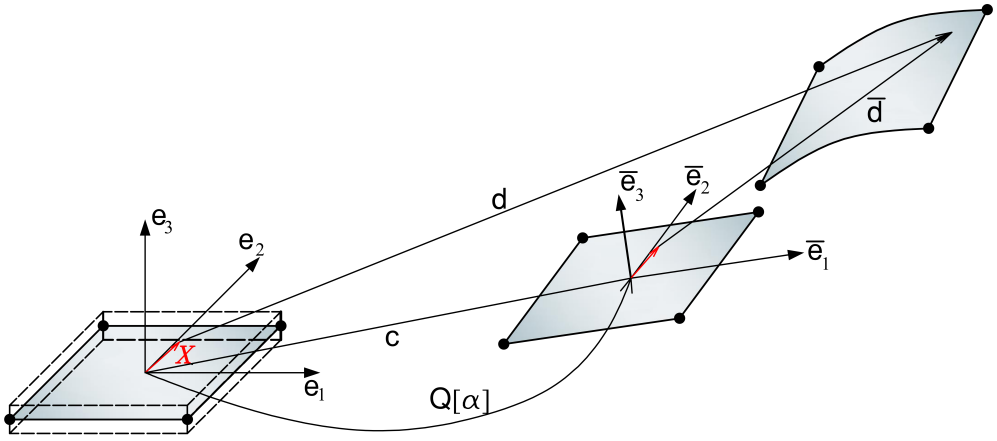

Figure 2.1: Corotational frame.

for further details.

Based on the above relations, the linear finite element characterized by energy (2.10) can be transformed into a geometrically nonlinear element simply by introducing a corotational description and assuming that the element kinematical parameters in eq. (2.10) are referred to the corotational frame. This leads to:

$$\Phi_e[\boldsymbol{t}_e, \boldsymbol{d}_e] = \boldsymbol{t}_e^T \boldsymbol{D}_e \boldsymbol{g}[\boldsymbol{d}_e] - \frac{1}{2}\boldsymbol{t}_e^T \boldsymbol{H}_e \boldsymbol{t}_e \tag{2.17}$$

The element energy can be expressed in terms of the element vector

$$\boldsymbol{u}_e = \{\boldsymbol{t}_e, \boldsymbol{d}_e\}^T \tag{2.18}$$

which collects all the parameters defining the element configuration in a single vector and can be related to the global configuration vector $\boldsymbol{u}$ through the standard assemblage procedure

$$\boldsymbol{u}_e = \boldsymbol{A}_e \boldsymbol{u} \tag{2.19}$$

where the matrix $\boldsymbol{A}_e$ implicitly contains the compatibility constraints between elements. For the Hellinger-Reissner formulation used here, the components of $\boldsymbol{u}$ are the global displacements/rotations of the nodes of the elements and the the stress parameters of each element. Using static condensation, the stress parameters can be eliminated at the element level, and then a compatible scheme can be employed [58].

2.4 Element implementation

The **M**ixed **I**sostatic **S**elf-equilibrated **S**tress flat shell element **MISS**-4 [15, 11] is used as the starting point here. It is a 4–node quadrilateral externally defined by 24 kinematical dofs and internally by an isostatic self–equilibrated stress expansion represented by 18 parameters.

It is described by four nodal coordinates on the plane $Z = 0$ of the global Cartesian system $\{X, Y, Z\}$ and the element connectivity ((2.2)).

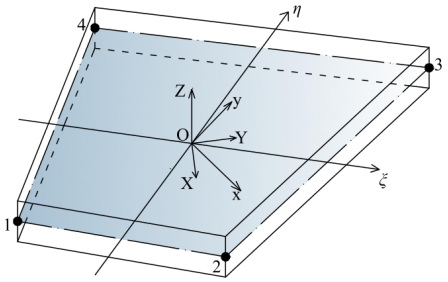

Figure 2.2: Global, local and internal coordinate systems.

Next, a dimensionless internal system is defined over the element mid surface with $\{\xi, \eta\}$, $-1 \leq \xi \leq 1, -1 \leq \eta \leq 1$, which is implicitly defined by

$$\begin{cases} X = a_0 + a_1\xi + a_2\xi\,\eta + a_3\eta \\ Y = b_0 + b_1\xi + b_2\xi\,\eta + b_3\eta \end{cases} \tag{2.20}$$

where

$$\begin{bmatrix} a_0 & b_0 \\ a_1 & b_1 \\ a_2 & b_2 \\ a_3 & b_3 \end{bmatrix} = \frac{1}{4} \begin{bmatrix} 1 & 1 & 1 & 1 \\ -1 & 1 & 1 & -1 \\ 1 & -1 & 1 & -1 \\ -1 & -1 & 1 & 1 \end{bmatrix} \begin{bmatrix} X^1 & Y^1 \\ X^2 & Y^2 \\ X^3 & Y^3 \\ X^4 & Y^4 \end{bmatrix} \tag{2.21}$$

where $\{X^i, Y^i\},\ i = 1, .., 4$ are the global nodal coordinates.

The third system is a local Cartesian system $\{x, y\}$, defined over the element mid surface, centered and aligned with the element. To define the local system, we introduce the Jacobian matrix $\boldsymbol{J}^G$ and its average $\bar{\boldsymbol{J}}^G$

$$\begin{aligned} \boldsymbol{J}^G &= \begin{bmatrix} X_{,\xi} & X_{,\eta} \\ Y_{,\xi} & Y_{,\eta} \end{bmatrix} = \begin{bmatrix} (a_1 + a_2\eta) & (a_3 + a_2\xi) \\ (b_1 + b_2\eta) & (b_3 + b_2\xi) \end{bmatrix} \\ \bar{\boldsymbol{J}}^G &= \frac{1}{4} \int_{\xi=-1}^{1} \int_{\eta=-1}^{1} \boldsymbol{J}^G \,\mathrm{d}\xi\,\mathrm{d}\eta = \begin{bmatrix} a_1 & a_3 \\ b_1 & b_3 \end{bmatrix} \end{aligned} \tag{2.22}$$

The average Jacobian $\bar{\boldsymbol{J}}^G$ is decomposed into an orthogonal matrix $\boldsymbol{R}$ and a symmetric matrix $\bar{\boldsymbol{J}}$, so that

$$\bar{\boldsymbol{J}}^G = \boldsymbol{R}\,\bar{\boldsymbol{J}} \tag{2.23}$$

$$\boldsymbol{R} = \begin{bmatrix} \cos\alpha & -\sin\alpha \\ \sin\alpha & \cos\alpha \end{bmatrix}, \quad \alpha = \arctan\left(\frac{a_3 - b_1}{a_1 + b_3}\right), \quad \bar{\boldsymbol{J}} = \begin{bmatrix} a & c \\ c & b \end{bmatrix}$$

The local Cartesian system $\{x, y\}$ has its origin at the element centroid ($\xi = \eta = 0$) and is rigidly rotated by $\boldsymbol{R}$ with respect to $\{X, Y\}$. The coordinates $\{x, y\}$ are defined according the transformation

$$\begin{bmatrix} x \\ y \end{bmatrix} = \boldsymbol{R}^T \begin{bmatrix} X - a_0 \\ Y - b_0 \end{bmatrix} \tag{2.24}$$

The use of a local system $\{x, y\}$ allows us to eliminate the rigid part of the global element distortion, providing a finite element description that is objective with respect to a rigid body motion of the element.

2.4.1 Assumed stresses

The stresses are assumed to be self equilibrated and isostatic, leading to a minimum set of parameters, which are the 18 components of the vector $\boldsymbol{\beta}_e$. Then, the stress resultants can be written as

$$\boldsymbol{t} = \boldsymbol{B}\boldsymbol{\beta}_e = \begin{bmatrix} \boldsymbol{B}_m & \boldsymbol{0} \\ \boldsymbol{0} & \boldsymbol{B}_f \end{bmatrix} \begin{bmatrix} \boldsymbol{\beta}_m \\ \boldsymbol{\beta}_f \end{bmatrix} \tag{2.25a}$$

where $\boldsymbol{B}_m$ and $\boldsymbol{B}_f$ are matrices representing the assumed stress modes for the membrane and flexural generalized stresses, respectively, and $\boldsymbol{\beta}_m, \boldsymbol{\beta}_f$ are 9-component vectors representing membrane and flexural effects, respectively. For the membrane stresses, it is assumed that

$$\boldsymbol{B}_m = \begin{bmatrix} 1 & 0 & 0 & y & 0 & x & 0 & y^2 & -2\,a^2\,x\,y \\ 0 & 1 & 0 & 0 & x & 0 & y & -x^2 & 2\,b^2\,x\,y \\ 0 & 0 & 1 & 0 & 0 & -y & -x & 0 & a^2\,y^2 - b^2\,x^2 \end{bmatrix} \tag{2.25b}$$

For the flexural stress, it is assumed that

$$\boldsymbol{B}_f = \begin{bmatrix} \boldsymbol{B}_b \\ \boldsymbol{B}_s \end{bmatrix} \quad \text{with} \quad \begin{cases} \boldsymbol{B}_b = \begin{bmatrix} 1 & 0 & 0 & x & 0 & y & 0 & x\,y & 0 \\ 0 & 1 & 0 & 0 & x & 0 & y & 0 & x\,y \\ 0 & 0 & 1 & 0 & y\,\bar{c} & x/\bar{c} & 0 & 0 & 0 \end{bmatrix} \\ \boldsymbol{B}_s = \begin{bmatrix} 0 & 0 & 0 & -1 & -\bar{c} & 0 & 0 & -y & 0 \\ 0 & 0 & 0 & 0 & 0 & -1/\bar{c} & -1 & 0 & -x \end{bmatrix} \end{cases} \tag{2.25c}$$

with $\bar{c} = a^2/b^2$. Both, membrane and flexural stresses are obtained starting from a polynomial expansion in Cartesian coordinates x, y and using Pian's equilibrium filter [15, 16, 17].

2.4.2 Assumed displacements

The interpolation of the displacement field $\boldsymbol{u}$ is controlled by the 24-component vector $\boldsymbol{u}_e$, collecting displacements and rotations of the four nodes of the element. Since the stress approximation satisfies the equilibrium equation, the internal work can be obtained by integrating on the element contour. Therefore, only contour displacements are needed. The displacement interpolation $\boldsymbol{u}_k$ along element side k is defined as the sum of three contributions

$$\boldsymbol{u}_k[\zeta] = \boldsymbol{u}_{kl}[\zeta] + \boldsymbol{u}_{kq}[\zeta] + \boldsymbol{u}_{kc}[\zeta] \tag{2.26a}$$

where $-1 \le \zeta \le 1$ is a one-dimensional coordinate along element side k. The first term is a linear expansion

$$\boldsymbol{u}_{kl}[\zeta] = \frac{1}{2}[(1-\zeta)\boldsymbol{u}^i + (1+\zeta)\boldsymbol{u}^j], \quad \begin{cases} \boldsymbol{u}^i = [u_x^i,\, u_y^i,\, u_z^i]^T \\ \boldsymbol{u}^j = [u_x^j,\, u_y^j,\, u_z^j]^T \end{cases} \tag{2.26b}$$

where superscripts i, j denote the nodes of element side k. The second and third terms correspond to quadratic and cubic expansions for the normal component of the element side displacements

$$\boldsymbol{u}_{kq}[\zeta] = \frac{1}{8}\, L_k(\zeta^2 - 1) \begin{bmatrix} (\varphi_z^i - \varphi_z^j)\, \boldsymbol{n}_k \\ -(\boldsymbol{\varphi}^i - \boldsymbol{\varphi}^j)^T \boldsymbol{n}_k \end{bmatrix}, \quad \boldsymbol{u}_{kc}[\zeta] = \frac{1}{4}\, L_k(\zeta - \zeta^3) \begin{bmatrix} \boldsymbol{n}_k \\ 0 \end{bmatrix} \theta \tag{2.26c}$$

with

$$\boldsymbol{\varphi}^i = [\varphi_x^i,\, \varphi_y^i]^T \quad , \quad \boldsymbol{\varphi}^j = [\varphi_x^j,\, \varphi_y^j]^T \tag{2.26d}$$

where $\boldsymbol{n}_k = [n_{kx}, n_{ky}]^T$ is the normal to the element side and L_k is the side length; and θ is the average in-plane distortional rotation, defined as

$$\theta = \frac{1}{4}\sum_{i=1}^{4} \varphi_z^i - \bar{\varphi}_z \tag{2.26e}$$

with $\bar{\varphi}_z$ the average in-plane rigid rotation of the element

$$\begin{aligned} \bar{\varphi}_z &= \boldsymbol{N}_\theta \boldsymbol{u}_{me} \\ \boldsymbol{N}_\theta &= \frac{1}{4\Omega_e}\left[-d_{4y},\ d_{4x},\ -d_{1y},\ d_{1x},\ -d_{2y},\ d_{2x},\ -d_{3y},\ d_{3x}\right] \end{aligned} \tag{2.26f}$$

By definition, the linear part $\boldsymbol{u}_{kl}$ and the quadratic part $\boldsymbol{u}_{kq}$ are continuous at the inter-element boundaries. The cubic contribution $\boldsymbol{u}_{kc}$ corresponds to an incompatible mode, which is added to avoid rank defectiveness [16]. Finally, a simple bilinear interpolation for bending rotations is used along the side

$$\boldsymbol{\varphi}_k[\zeta] = \frac{1}{2}[(1-\zeta)\boldsymbol{\varphi}_i + (1+\zeta)\boldsymbol{\varphi}_j], \quad \boldsymbol{\varphi}_k[\zeta] = [\varphi_x,\ \varphi_y]^T \tag{2.26g}$$

2.4.3 Compliance and compatibility

Introducing assumed stress (2.25) and assumed displacements (2.26) into the mixed strain energy (2.1), the mixed strain energy Φ_e of the element can be defined as follows

$$\Phi_e = \boldsymbol{\beta}_e^T \boldsymbol{D}_e \boldsymbol{u}_e - \frac{1}{2}\boldsymbol{\beta}_e^T \boldsymbol{H}_e \boldsymbol{\beta}_e \tag{2.27a}$$

where $\boldsymbol{H}_e$ and $\boldsymbol{Q}_e$ are the element compliance matrix and the compatibility matrix respectively. The compliance matrix can be written as follows

$$\boldsymbol{H}_e = \begin{bmatrix} \boldsymbol{H}_m & \boldsymbol{H}_{mb} & \boldsymbol{0} \\ & \boldsymbol{H}_b & \boldsymbol{0} \\ \text{sym} & & \boldsymbol{H}_s \end{bmatrix} \tag{2.27b}$$

where

$$\boldsymbol{H}_m = \int_{\Omega_e} \left\{\boldsymbol{B}_m^T \boldsymbol{E}_m^{-1} \boldsymbol{B}_m\right\} \mathrm{d}\Omega, \quad \boldsymbol{H}_{mb} = \int_{\Omega_e} \left\{\boldsymbol{B}_m^T \boldsymbol{E}_{mb}^{-1} \boldsymbol{B}_b\right\} \mathrm{d}\Omega \tag{2.27c}$$

and

$$\boldsymbol{H}_b = \int_{\Omega_e} \left\{\boldsymbol{B}_b^T \boldsymbol{E}_b^{-1} \boldsymbol{B}_b\right\} \mathrm{d}\Omega, \quad \boldsymbol{H}_s = \int_{\Omega_e} \left\{\boldsymbol{B}_s^T \boldsymbol{E}_s^{-1} \boldsymbol{B}_s\right\} \mathrm{d}\Omega \tag{2.27d}$$

Since the compatibility matrix is due to self-equilibrated stress interpolation, and it is eval-

uated trough analytical contour integration, it can be written as follows

$$\boldsymbol{Q}_e = \begin{bmatrix} \boldsymbol{Q}_m & \boldsymbol{0} \\ \boldsymbol{0} & \boldsymbol{Q}_f \end{bmatrix}, \quad \boldsymbol{Q}_m = \sum_{k=1}^{4} \boldsymbol{Q}_{mk} + \boldsymbol{Q}_c \,, \quad \boldsymbol{Q}_f = \sum_{k=1}^{4} \boldsymbol{Q}_{fk} \tag{2.27e}$$

The matrices $\boldsymbol{Q}_{mk}$ and $\boldsymbol{Q}_{fk}$ are defined as follows

$$\begin{aligned} \boldsymbol{\beta}_m^T \boldsymbol{Q}_{mk} \boldsymbol{u}_{em} &= \int_{-1}^{1} \boldsymbol{t}_m^T[\zeta] \boldsymbol{N}_{mk}^T \boldsymbol{u}_{mk}[\zeta] \, \mathrm{d}\zeta \\ \boldsymbol{\beta}_m^T \boldsymbol{Q}_c \boldsymbol{u}_{em} &= \int_{-1}^{1} \boldsymbol{t}_m^T[\zeta] \boldsymbol{N}_{mk}^T \boldsymbol{u}_c[\zeta] \, \mathrm{d}\zeta \\ \boldsymbol{\beta}_f^T \boldsymbol{Q}_{fk} \boldsymbol{u}_{ef} &= \int_{-1}^{1} \boldsymbol{t}_f^T[\zeta] \boldsymbol{N}_{fk}^T \boldsymbol{u}_{fk}[\zeta] \, \mathrm{d}\zeta \end{aligned} \tag{2.27f}$$

where the vectors $\boldsymbol{u}_{em}$ and $\boldsymbol{u}_{ef}$ collect the nodal displacements and rotations describing the membrane and flexural behavior, respectively. Finally, the matrices $\boldsymbol{N}_{mk}, \boldsymbol{N}_{fk}$ split the components of the normal to the element side, as follows

$$\boldsymbol{N}_{mk} = \begin{bmatrix} n_{kx} & 0 & n_{ky} \\ 0 & n_{ky} & n_{kx} \end{bmatrix}, \quad \boldsymbol{N}_{fk} = \begin{bmatrix} 0 & 0 & 0 & n_{kx} & n_{ky} \\ n_{kx} & n_{ky} & 0 & 0 & 0 \\ -n_{ky} & 0 & -n_{kx} & 0 & 0 \end{bmatrix}. \tag{2.27g}$$

2.5 High order energy variations

To apply the asymptotic approach to the corotational version of element MISS-4, explicit expressions for the second-, third- and fourth–order energy variations need to be computed [8] with respect to a configuration that can be either the initial ($\boldsymbol{u}_0$ in (1.7a)) or the bifurcation one ($\boldsymbol{u}_0 + \lambda\hat{\boldsymbol{u}}$ in (1.7a)). For computation of second or higher order terms, the constant terms $\boldsymbol{u}_0$ and $\boldsymbol{u}_0 + \lambda\hat{\boldsymbol{u}}$ are irrelevant, so at the element level we can assume $\boldsymbol{d}_e = \boldsymbol{0}$.

The corotational approach is very convenient to express the strain energy variations, because the only nonlinearity is limited to the geometrical relationship $\boldsymbol{g}[\boldsymbol{d}_e]$, eq. (2.16). The Taylor expansion of this relationship can be written as

$$\boldsymbol{g}[\boldsymbol{d}_e] = \boldsymbol{g}_1[\boldsymbol{d}_e] + \frac{1}{2}\boldsymbol{g}_2[\boldsymbol{d}_e, \boldsymbol{d}_e] + \frac{1}{6}\boldsymbol{g}_3[\boldsymbol{d}_e, \boldsymbol{d}_e, \boldsymbol{d}_e] + \frac{1}{24}\boldsymbol{g}_4[\boldsymbol{d}_e, \boldsymbol{d}_e, \boldsymbol{d}_e, \boldsymbol{d}_e] + \cdots \tag{2.28}$$

where $\boldsymbol{g}_n$ are n–multilinear symmetric forms which express the nth Fréchet variations of function $\boldsymbol{g}[\boldsymbol{d}_e]$. In the following, the vector $\boldsymbol{u}_i$ ($i = 1 \ldots 4$) denotes a generic variation of the global finite element configuration vector and the vector $\boldsymbol{u}_{ei} = \boldsymbol{A}_e \boldsymbol{u}_i = \{\boldsymbol{t}_{ei}, \boldsymbol{d}_{ei}\}^T$ denotes the corresponding vector at the element level, that collects stress and displacement parameters. With the same notation, $\boldsymbol{u}_0$ and $\boldsymbol{u}_{e0}$ are the global and element reference configuration vectors.

2.5.1 *Second-order variations*

Second–order energy variations are used in the evaluation of the fundamental path (1.7a) and the buckling modes $\dot{\boldsymbol{v}}$. In both cases, using expansion (2.28) and the energy expression (2.17), the contribution of the element to the energy variation can be expressed as

$$\Phi_e^{''}\boldsymbol{u}_{e1}\boldsymbol{u}_{e2} = \boldsymbol{t}_{e1}^T\boldsymbol{D}_e\boldsymbol{g}_1[\boldsymbol{d}_{e2}] + \boldsymbol{t}_{e2}^T\boldsymbol{D}_e\boldsymbol{g}_1[\boldsymbol{d}_{e1}] - \boldsymbol{t}_{e1}^T\boldsymbol{H}_e\boldsymbol{t}_{e2} + \boldsymbol{t}_{e0}^T\boldsymbol{D}_e\boldsymbol{g}_2[\boldsymbol{d}_{e1},\boldsymbol{d}_{e2}] \tag{2.29}$$

Introducing matrices $\boldsymbol{L}_1$ and $\boldsymbol{G}[\boldsymbol{t}_e]$ through the following equivalences

$$\boldsymbol{L}_1\boldsymbol{d}_{ej} = \boldsymbol{g}_1[\boldsymbol{d}_{ej}] \quad , \quad \boldsymbol{d}_{e1}^T\boldsymbol{G}[\boldsymbol{t}_{e0}]\boldsymbol{d}_{e2} = \boldsymbol{t}_{e0}^T\boldsymbol{D}_e\boldsymbol{g}_2[\boldsymbol{d}_{e1},\boldsymbol{d}_{e2}], \tag{2.30}$$

eq. (2.29) can be rearranged in a more compact form:

$$\boldsymbol{u}_{e1}^T\Phi_e^{''}\boldsymbol{u}_{e2} = \boldsymbol{u}_{e1}^T\boldsymbol{K}_e\boldsymbol{u}_{e2} \quad , \quad \boldsymbol{K}_e = \begin{bmatrix} -\boldsymbol{H}_e & \boldsymbol{D}_e\boldsymbol{L}_1 \\ \boldsymbol{L}_1^T\boldsymbol{D}_e^T & \boldsymbol{G}[\boldsymbol{t}_{e0}] \end{bmatrix} \tag{2.31}$$

The mixed tangent matrix of the element $\boldsymbol{K}_e$ can be directly used, through a standard assemblage process, to obtain the overall stiffness matrix $\boldsymbol{K}$

$$\boldsymbol{u}_1^T\Phi^{''}\boldsymbol{u}_2 = \boldsymbol{u}_1^T\boldsymbol{K}\boldsymbol{u}_2 \quad , \quad \boldsymbol{K} = \sum_e \boldsymbol{A}_e^T\boldsymbol{K}_e\boldsymbol{A}_e \tag{2.32}$$

2.5.2 *Third-order variations*

Third-order energy variations are used in Koiter analysis to evaluate the third–order coefficients and are also used to evaluate the secondary force vectors. The element contribution to the scalar coefficients can be easily calculated using the general formula

$$\begin{aligned}\Phi_e^{'''}\boldsymbol{u}_{e1}\boldsymbol{u}_{e2}\boldsymbol{u}_{e3} = {} & \boldsymbol{t}_{e1}^T\boldsymbol{D}_e\boldsymbol{g}_2[\boldsymbol{d}_{e2},\boldsymbol{d}_{e3}] + \boldsymbol{t}_{e2}^T\boldsymbol{D}_e\boldsymbol{g}_2[\boldsymbol{d}_{e3},\boldsymbol{d}_{e1}] + \boldsymbol{t}_{e3}^T\boldsymbol{D}_e\boldsymbol{g}_2[\boldsymbol{d}_{e1},\boldsymbol{d}_{e2}] \\ & + \boldsymbol{t}_{e0}^T\boldsymbol{D}_e\boldsymbol{g}_3[\boldsymbol{d}_{e1},\boldsymbol{d}_{e2},\boldsymbol{d}_{e3}]\end{aligned} \tag{2.33}$$

Then the element contributions can be simply added to get the global values. On the other hand, taking advantage of the above expression, the element contribution to vector secondary force vector can be evaluated by

$$\Phi_e^{'''}\boldsymbol{u}_{e1}\boldsymbol{u}_{e2} = \boldsymbol{p}_e = \begin{bmatrix} \boldsymbol{D}_e\boldsymbol{g}_2[\boldsymbol{d}_{e1},\boldsymbol{d}_{e2}] \\ \boldsymbol{G}[\boldsymbol{t}_{e1}]\boldsymbol{d}_{e2} + \boldsymbol{G}[\boldsymbol{t}_{e2}]\boldsymbol{d}_{e1} + \boldsymbol{q}[\boldsymbol{t}_{e0},\boldsymbol{d}_{e1},\boldsymbol{d}_{e2}] \end{bmatrix} \tag{2.34}$$

where vector $\boldsymbol{q}$ is defined according to the following condition:

$$\boldsymbol{d}_{e3}^T \boldsymbol{q}[\boldsymbol{t}_{e0}, \boldsymbol{d}_{e1}, \boldsymbol{d}_{e2}] = \boldsymbol{t}_{e0}^T \boldsymbol{D}_e \boldsymbol{g}_3[\boldsymbol{d}_{e1}, \boldsymbol{d}_{e2}, \boldsymbol{d}_{e3}] \tag{2.35}$$

Then, the overall vector is obtained by standard assemblage

$$\Phi''' \boldsymbol{u}_1 \boldsymbol{u}_2 = \sum_e \boldsymbol{A}_e^T \boldsymbol{p}_e[\boldsymbol{u}_{e1}, \boldsymbol{u}_{e2}]$$

2.5.3 *Fourth-order variations*

Finally, fourth-order energy variations, used to evaluate the fourth–order coefficients, can be computed by summing the relevant element contributions based on the following expression

$$\begin{aligned} \Phi_e'''' \boldsymbol{u}_{e1} \boldsymbol{u}_{e2} \boldsymbol{u}_{e3} \boldsymbol{u}_{e4} = {} & \boldsymbol{t}_{e1}^T \boldsymbol{D}_e \boldsymbol{g}_3[\boldsymbol{d}_{e2}, \boldsymbol{d}_{e3}, \boldsymbol{d}_{e4}] + \boldsymbol{t}_{e2}^T \boldsymbol{D}_e \boldsymbol{g}_3[\boldsymbol{d}_{e3}, \boldsymbol{d}_{e4}, \boldsymbol{d}_{e1}] \\ & + \boldsymbol{t}_{e3}^T \boldsymbol{D}_e \boldsymbol{g}_3[\boldsymbol{d}_{e4}, \boldsymbol{d}_{e1}, \boldsymbol{d}_{e2}] + \boldsymbol{t}_{e4}^T \boldsymbol{D}_e \boldsymbol{g}_3[\boldsymbol{d}_{e1}, \boldsymbol{d}_{e2}, \boldsymbol{d}_{e3}] \\ & + \boldsymbol{t}_{e0}^T \boldsymbol{D}_e \boldsymbol{g}_4[\boldsymbol{d}_{e1}, \boldsymbol{d}_{e2}, \boldsymbol{d}_{e3}, \boldsymbol{d}_{e4}] \end{aligned} \tag{2.36}$$

Chapter 3

MISS-4 flat shell finite element: numerical assessment

3.1 Introduction

In this chapter, an investigation on the performance of the proposed shell element for linear static and buckling analysis of laminated composite folded plates is presented. First, the static linear analysis of laminated composite plates for different laminate stacking sequences (LSS) and span-to-thickness ratios is performed. Particular attention is given to the point-wise and global convergence of the stress resultant to elucidate the behavior of the element for regular and distorted mesh. Then, buckling of simply supported plates is reported. Buckling modes, loads, and their convergence are reported. Finally, linear static and buckling analysis of three folded, laminated-composite, are reported. The first is a clamped Ω section under shear force. The second is a clamped C shaped section under shear force while the third is a clamped box under torsional couple. Different LSS are considered. Global convergence for linear static analysis and convergence on buckling load, buckling modes and comparison with S8R are given.

3.2 Linear static analysis of laminated plates

The benchmark for static linear analysis is a simply supported square plate of side a (see fig. 3.1) under uniform distributed load q. The lamina elastic properties are: $E_1 = 25$, $E_2 = 1$, $G_{12} = G_{13} = 0.5$, $G_{23} = 0.2$, $\nu_{12} = 0.25$.

Cross-ply and angle-ply laminates are considered, as follows:

i.. A symmetric cross-ply laminate [0/90/0] with SS1 boundary [67, Section 3.1.3] and shear factors $k_{11} = 235445/404004$, $k_{12} = 0$, $k_{22} = 289/360$ [68];

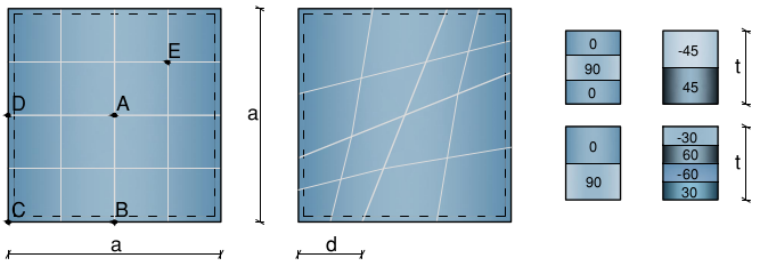

Figure 3.1: Simply supported square plate. Geometry and mesh.

ii.. An antisymmetric cross-ply laminate [0/90], with SS1 boundary and shear factors $k_{11} = k_{22} = 297680/362481$, $k_{12} = 0$ [68];

iii.. An antisymmetric angle-ply $[-45/45]$ [69];

iv.. An angle-ply $[-30/60/-60/30]$, with SS2 boundary condition and shear factors $k_{11} = k_{22} = k_{12} = 5/6$ [69].

All results are obtained for side-length/thickness ratio $a/t = 10, 20, 100$. Analytical solutions [42] are used as reference, using the following dimensionless parameters for displacement and stress resultants:

$$\bar{w} = w\frac{100\,E_2}{qt\,(a/t)^4}, \quad \bar{N}_x = N_x\frac{100}{q\,t\,(a/t)^2}, \quad \bar{S}_y = S_y\frac{100}{q\,t\,(a/t)} \tag{3.1}$$

and

$$\begin{bmatrix} \bar{M}_x \\ \bar{M}_y \\ \bar{M}_{xy} \end{bmatrix} = \frac{100}{q\,t^2\,(a/t)^2}\begin{bmatrix} M_x \\ M_y \\ M_{xy} \end{bmatrix} \tag{3.2}$$

being w the transversal displacement of the plate.

Point-wise converge for displacements and stress resultant are listed in Tables 3.1, 3.2, 3.3 and 3.4. The percentage error is defined as

$$error\% = 100 \times \frac{\text{numerical} - \text{analytical}}{\text{analytical}} \tag{3.3}$$

It can be seen in Tables 3.1–3.4 that the convergence to the analytical solution is very fast for all values of span-to-thickness ratio.

Stress resultant convergence are graphed in Figs. 3.2, 3.3, 3.4 and 3.5. The solid line representing h^2 is shown for reference; where h is the element size of the regular mesh, or span over number of elements per side for irregular meshes. It can be seen that the element displays h^2 convergence for a variety of laminates and span-to-thickness ratios, and that the h^2 convergence

is maintained for distorted mesh (Fig. 3.6).

Point-wise and overall convergence properties are investigated using also distorted mesh with $d = 0.2\,a$ (see Fig. 3.1). The convergence rate measured using s-norm [70], shows that the rate of convergence is preserved also for distorted mesh (Fig. 3.6).

The results are compared with the S8R laminated plate elements implemented in the commercial software Abaqus [84, 67] and when available with mixed finite element available in literature [68].

		% error				
a/t	Mesh	$\bar{w}^A$	$\bar{M}_x^E$	$\bar{M}_y^E$	$\bar{M}_{xy}^E$	$\bar{S}_y^E$
10	4x4	3.152	1.197	8.011	21.016	6.552
	8x8	0.745	0.127	1.053	4.986	1.963
	16x16	0.188	-0.019	0.2	1.199	0.506
	32x32	0.051	-0.006	0.043	0.316	0.111
	64x64	0.017	-0.001	0.009	0.095	0.016
20	4x4	3.931	-0.569	9.537	22.012	1.151
	8x8	0.929	-0.174	1.441	4.463	1.402
	16x16	0.226	-0.067	0.315	0.983	0.481
	32x32	0.063	-0.017	0.079	0.227	0.11
	64x64	0.013	-0.003	0.023	0.038	0.015
100	4x4	4.886	-4.264	9.921	24.363	-17.493
	8x8	1.087	-0.338	1.711	4.56	-3.414
	16x16	0.268	-0.086	0.38	0.904	0.015
	32x32	0.06	-0.022	0.101	0.205	0.068
	64x64	0.015	-0.004	0.025	0.041	0.005
		Dimensionless analytical values				
a/t	-	$\bar{w}^A$	$\bar{M}_x^E$	$\bar{M}_y^E$	$\bar{M}_{xy}^E$	$\bar{S}_y^E$
10	-	-1.168	7.016	1.15	-0.317	18.955
20	-	-0.796	7.432	0.888	-0.264	19.976
100	-	-0.671	7.594	0.789	-0.243	20.448

Table 3.1: Percentage error with respect to the analytical solution values [85] on the transversal displacement at point A, bending moments and shear forces at point E, for regular mesh and span-to-thickness ratios on a simply supported square plate [0/90/0] under uniform distributed load.

3.2.1 Buckling analysis of a laminated square plate

The buckling analysis of a laminated square plate ($l \times l \times t$) is presented here. The geometry, material properties, boundary, and load conditions are taken from [86]. The plate is simply supported on its boundary and loaded with a uniform edge pressure λ. The thickness is $t = 1.272\,10^{-4}$ m. The length is $l = 0.508$ m. The LLS is $[0/90/90/0]_S$. The lamina materials properties are $E_1 = 181$ GPa, $E_2 = 10.27$ GPa, $G_{12} = 7.17$ GPa, $\nu_{12} = 0.28$. The critical loads are listed in Table 4.1 and the buckling modes are shown in Fig. 4.1. Note that h^2 convergence is achieved for buckling loads (i.e., eigenvalues) as shown in Fig. 4.2. While the results obtained using the proposed element coincide with those obtained using Abaqus S8R elements when both use a 64x64 mesh, it must be noted that the proposed element has only 24 dof in comparison to 48 dof for S8R.

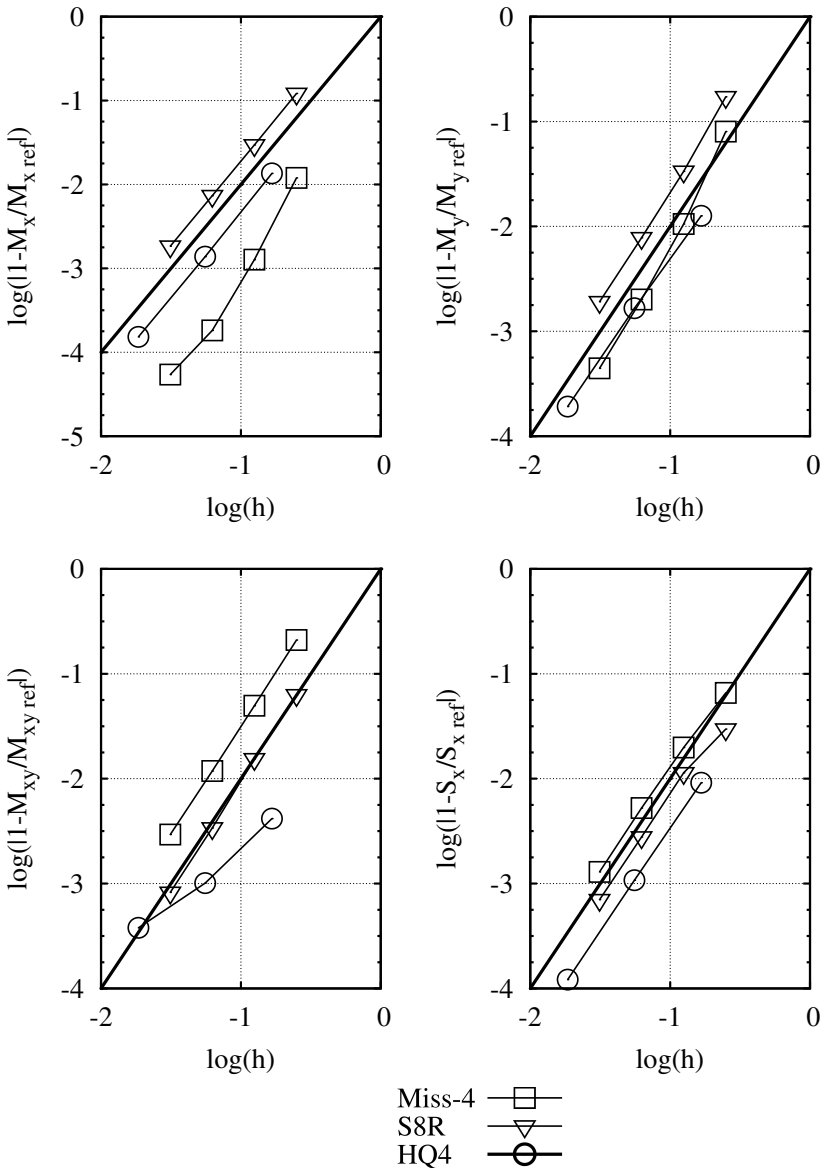

Figure 3.2: Simply supported square plate [0/90/0]. Convergence of bending moments and shear forces at point E, for regular for various values of span-to-thickness ratio. The solid line represents h^2 (shown for reference). S8R (Abaqus) and HQ4 [68] results are shown for comparison.

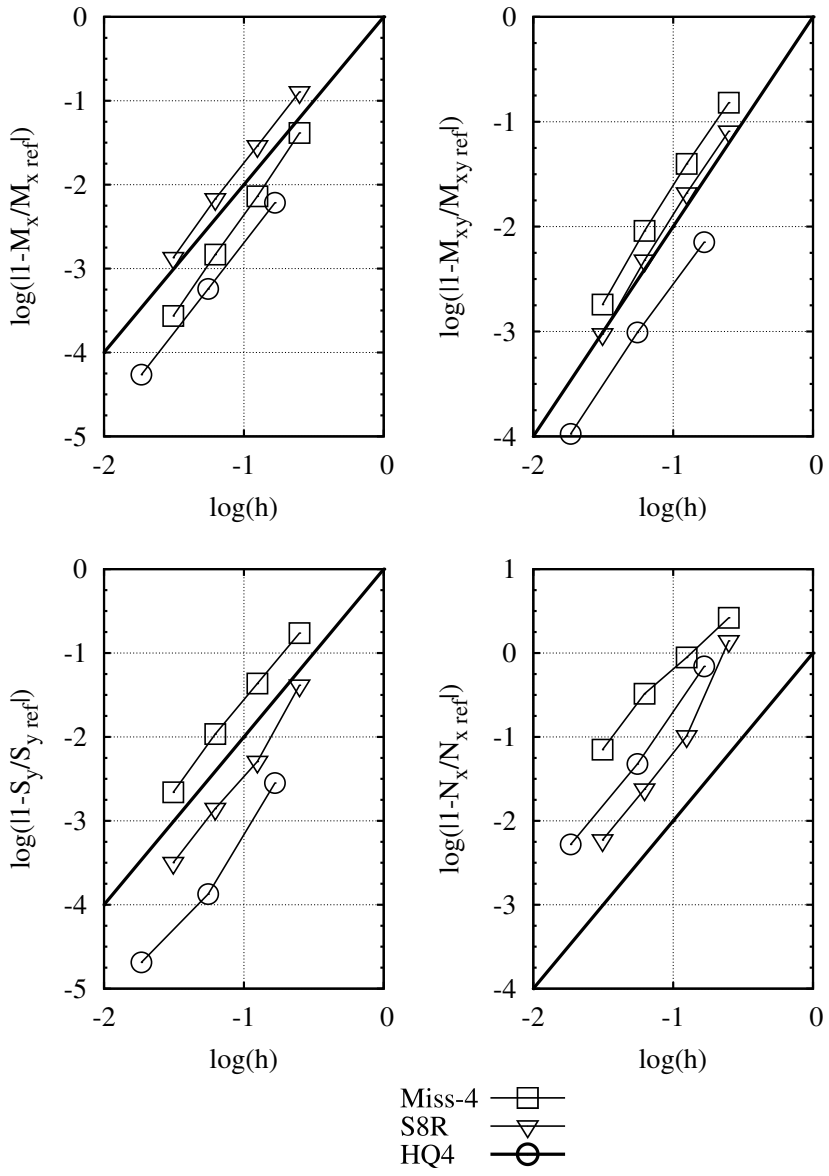

Figure 3.3: Simply supported square plate [0/90]. Convergence graphs for flexural moments, shear stress resultant, and axial stress resultant at point E for different span-to-thickness ratio using regular mesh. S8R (Abaqus) and HQ4 [68] results are shown for comparison.

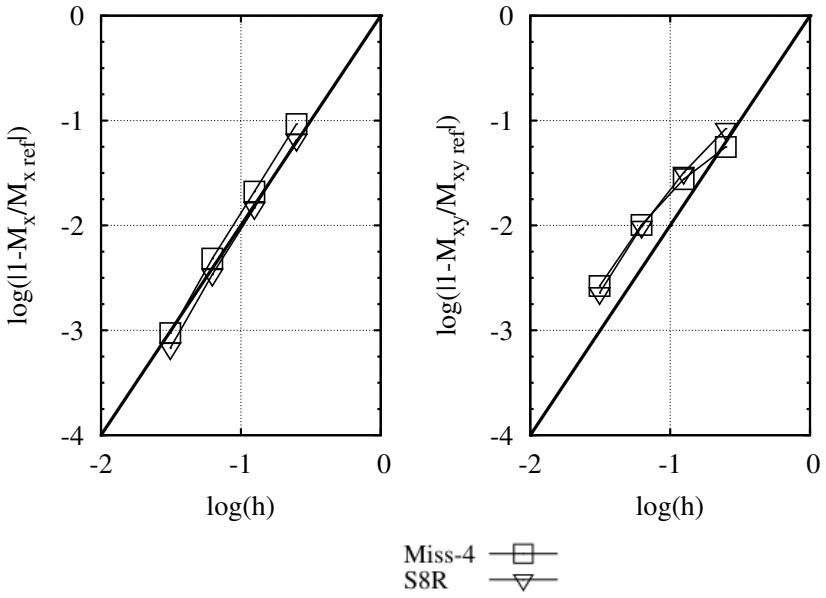

Figure 3.4: Simply supported square plate $[-45/45]$. Convergence graphs for flexural moments resultant at points A and C for different span-to-thickness ratios using regular mesh. S8R (Abaqus) and HQ4 [68] results are shown for comparison.

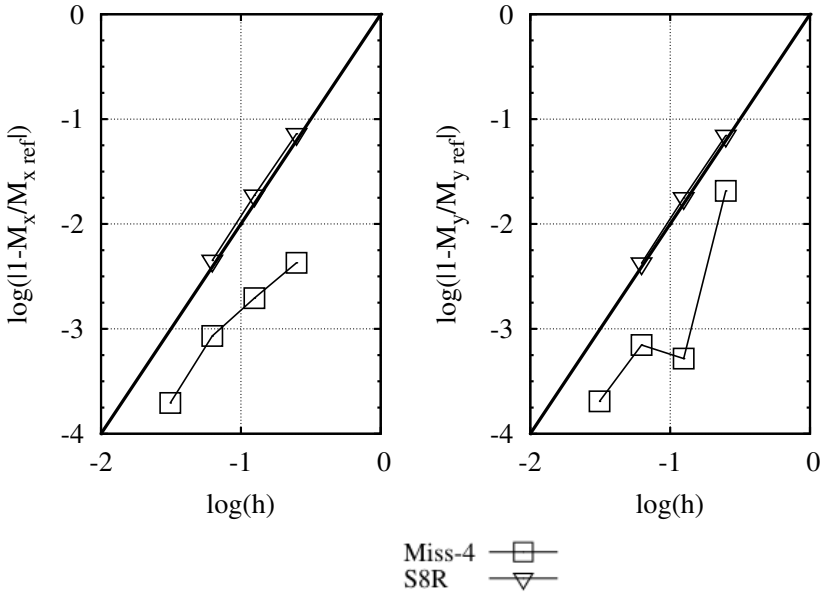

Figure 3.5: Simply supported square plate $[30/-60/60/-30]$. Convergence graphs for flexural moments resultant at points A for different span-to-thickness ratio using regular mesh. S8R (Abaqus) and HQ4 [68] results are shown for comparison.

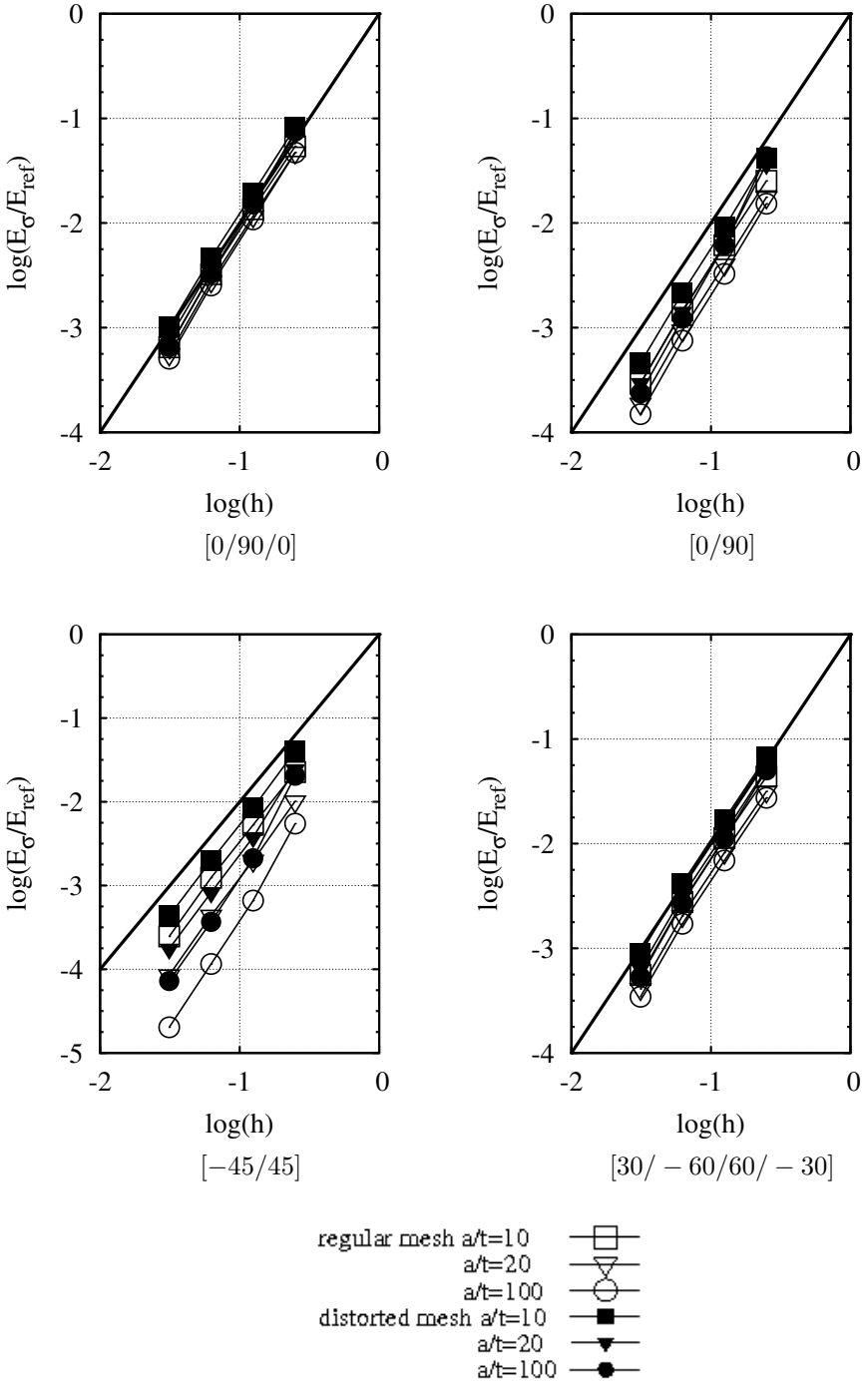

Figure 3.6: Simply supported square plate for different LSS. Convergence graphs using s-norm, for different span-to-thickness ratio using regular and distorted mesh.

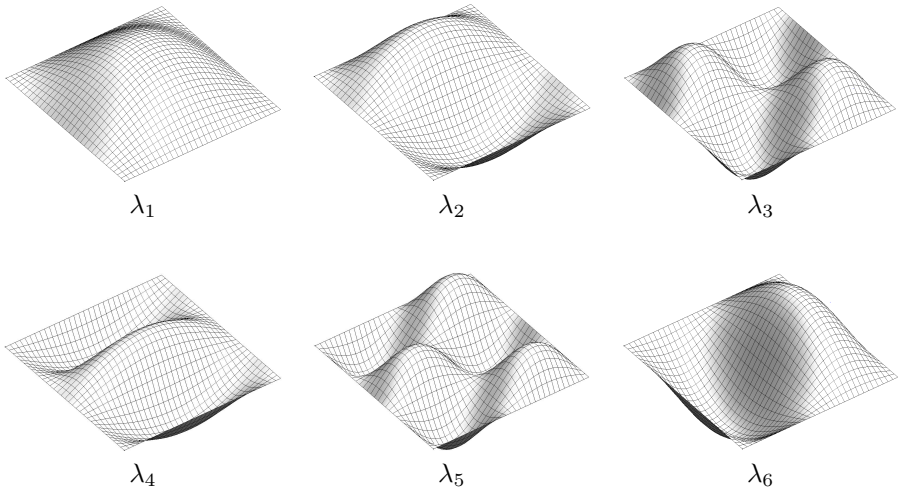

Figure 3.7: Square plate $[0/90/90/0]_S$ under uniaxial compression. Buckling modes.

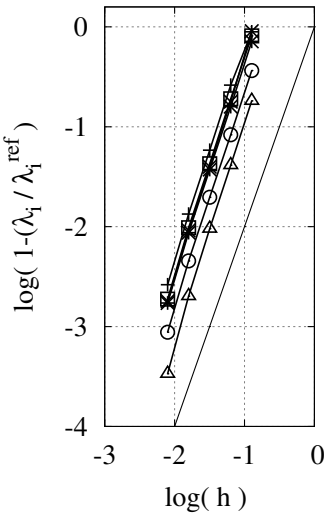

Figure 3.8: Square plate $[0/90/90/0]_S$ under uniaxial compression. Convergence of buckling loads with mesh refinement. The solid line represents h^2 (for reference).

		% error			
a/t	Mesh	$\bar{w}^A$	$\bar{M}_x^E$	$\bar{M}_{xy}^E$	$\bar{S}_y^E$
10	4x4	1.553	1.683	7.541	-29.66
	8x8	0.359	0.231	2.138	-16.246
	16x16	0.087	0.032	0.474	-8.555
	32x32	0.021	0.002	0.062	-4.389
	64x64	0.005	-0.005	-0.025	-2.222
20	4x4	1	0.677	9.609	-30.793
	8x8	0.244	0.126	3.044	-16.347
	16x16	0.057	0.008	0.812	-8.538
	32x32	0.006	-0.005	0.171	-4.372
	64x64	0	-0.006	0.006	-2.213
100	4x4	0.724	-0.144	11.321	-32.146
	8x8	0.194	0.008	4.041	-16.747
	16x16	0.041	-0.008	1.257	-8.618
	32x32	0.006	-0.008	0.34	-4.376
	64x64	0	-0.008	0.071	-2.21
		Dimensionless analytical values			
a/t	-	$\bar{w}^A$	$\bar{M}_x^E$	$\bar{M}_{xy}^E$	$\bar{S}_y^E$
10	-	-1.951	6.268	-1.604	-34.703
20	-	-1.759	6.291	-1.577	-34.881
100	-	-1.698	6.301	-1.559	-34.937

Table 3.2: Percentage error with respect to the analytical solution values [85] on the transversal displacement at point A, bending moments and shear forces at point E, for regular mesh and span-to-thickness ratios on a simply supported square plate [0/90] under uniform distributed load.

3.3 Linear and buckling analysis of laminated folded plates

The linear static and buckling analysis of three folded plate structures are here presented here. The first is a clamped beam with Ω-section under shear force, the second is a clamped beam with C-section under shear forces, and the third is a clamped box beam subjected to torque. Each folded section is analyzed for various laminate stacking sequences (LSS). For the first section, static linear analysis is performed and the convergence using s-norm is reported. For the second and third sections, buckling convergence as a function of mesh refining is discussed. The predictions are compared with results obtained using element S8R in Abaqus.

3.3.1 Clamped beam with Ω-section under shear force

Linear static analysis of a clamped beam with Ω section is reported here. The geometry is shown in Fig. 3.9. The length is $l = 100$ mm and the width is $a = 2.5$ mm. Three thickness are considered $a/t = 2, 5/2, 10/3$. The mechanical properties of each lamina are $E_1 = 104$ GPa; $E_2 = 10.3$ GPa; $G = 5.15$ GPa; $\nu_{12} = 0.021$ and two LSS are analyzed, [0/90/0/90] and [0/45/0/45]. A line load $q = 25$ kN/mm is applied. The global convergence using s-norm is reported in Fig. 3.10 and a rate of convergence h^2 is shown.

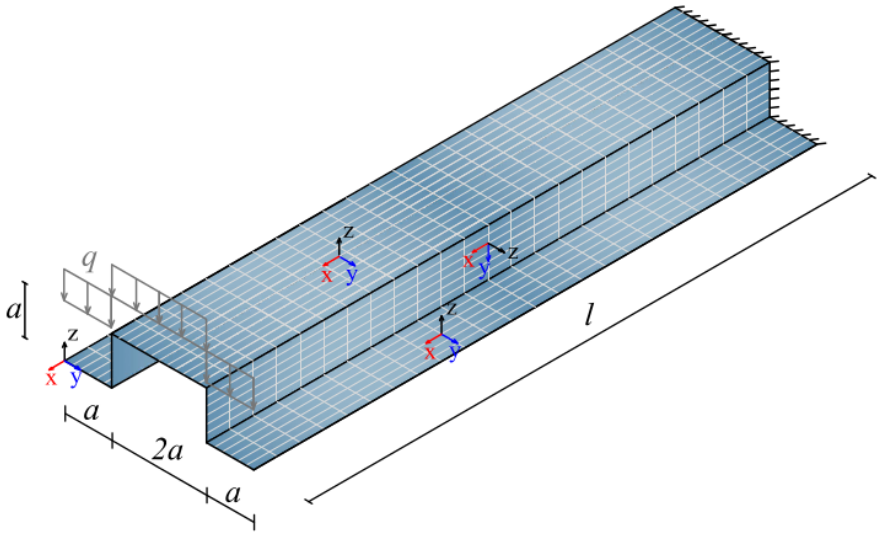

Figure 3.9: Clamped beam with Ω-section. Geometry, boundary conditions and mesh.

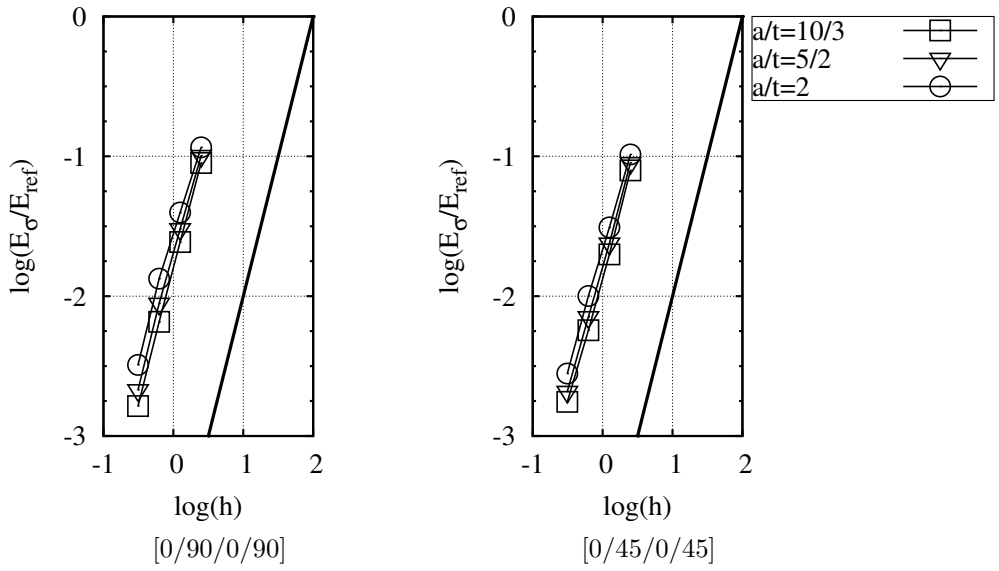

Figure 3.10: Clamped beam with Ω-section for different LSS. Convergence graphs using s-norm, for different values of a/t using regular mesh. The solid line represents h^2 (shown for reference).

		% error				
a/t	Mesh	$\bar{w}^A$	$\bar{M}_x^A$	$\bar{M}_{xy}^C$	$\bar{S}_y^B$	$\bar{N}_x^C$
10	4x4	1.29	9.298	5.699	-30.38	-21.691
	8x8	0.305	2.132	2.862	-16.845	-11.659
	16x16	0.078	0.511	1.109	-8.961	-5.901
	32x32	0.023	0.121	0.363	-4.621	-2.492
	64x64	0.008	0.027	0.098	-2.345	-0.93
20	4x4	0.513	8.206	5.899	-31.78	-18.554
	8x8	0.147	2.054	2.659	-17.046	-6.974
	16x16	0.037	0.497	0.998	-9.026	-3.673
	32x32	0.009	0.117	0.33	-4.656	-1.808
	64x64	0	0.024	0.087	-2.365	-0.761
100	4x4	0.136	7.741	6.274	-33.255	-17.434
	8x8	0.078	2.008	2.885	-17.702	-3.964
	16x16	0.019	0.493	0.991	-9.173	-1.077
	32x32	0	0.12	0.288	-4.679	-0.421
	64x64	0	0.027	0.066	-2.371	-0.234
		Dimensionless analytical values				
a/t	-	$\bar{w}^A$	$\bar{M}_x^A$	$\bar{M}_{xy}^C$	$\bar{S}_y^B$	$\bar{N}_x^C$
10	-	-1.279	3.72	-4.381	-32.788	-0.774
20	-	-1.091	3.745	-4.479	-32.517	-0.697
100	-	-1.031	3.755	-4.552	-32.398	-0.641

Table 3.3: Percentage error with respect to the analytical solution values [85] on the transversal displacement at point A, bending moments at points A, C, shear forces at point B and membrane stress resultant at point C, for regular mesh and span-to-thickness ratios on a simply supported square plate $[-45/45]$ under uniform distributed load.

3.3.2 Clamped beam C-section under shear force

The buckling analysis of folded C-section [118] is presented here. The geometrical data (Fig. 3.11) are $l = 36$ m, $b = 2.025$ m, $a = 6.05$ m and $t = 0.05m$. The concentrated load is $F = 250$ KN. The mechanical properties of each lamina are $E_1 = 30.6$ GPa; $E_2 = 8.7$ GPa; $G_{12} = 3.24$ GPa; $G_{23} = 2.29$ GPa; $\nu_{12} = 0.29$ and two LSS, here called LSS_1 and LSS_2, are analyzed. LSS_1 is shown in Fig. 3.11 and LSS_2 is a $[0/90/0]$ for all three panels in the C-section. Buckling loads are reported in Table. 3.6, achieving h^2 convergence, as shown in Fig.3.12. The corresponding modes are graphed in Fig. 3.13.

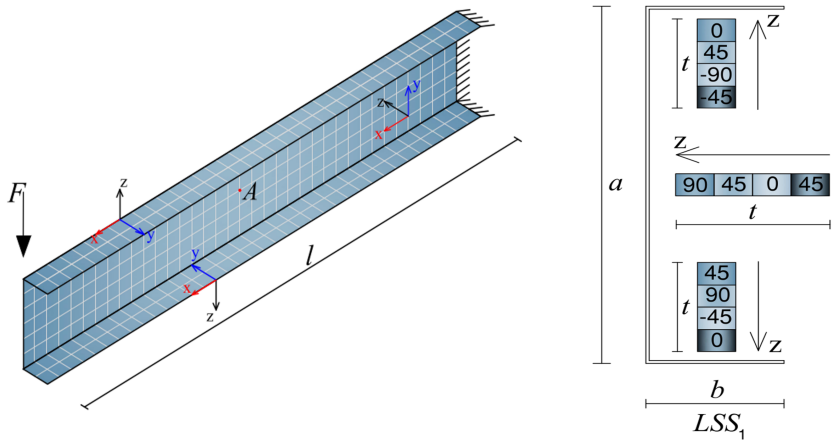

Figure 3.11: Clamped beam C-section. Geometry, boundary condition and mesh.

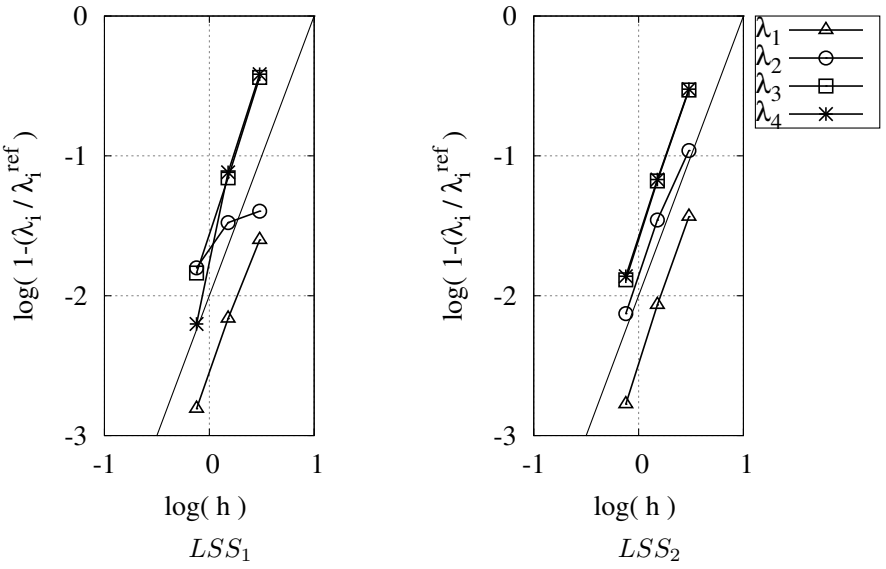

LSS_1 LSS_2

Figure 3.12: Clamped beam with C-section under shear forces for different LSS. Convergence of buckling loads with mesh refinement. The solid line represents h^2 (for reference).

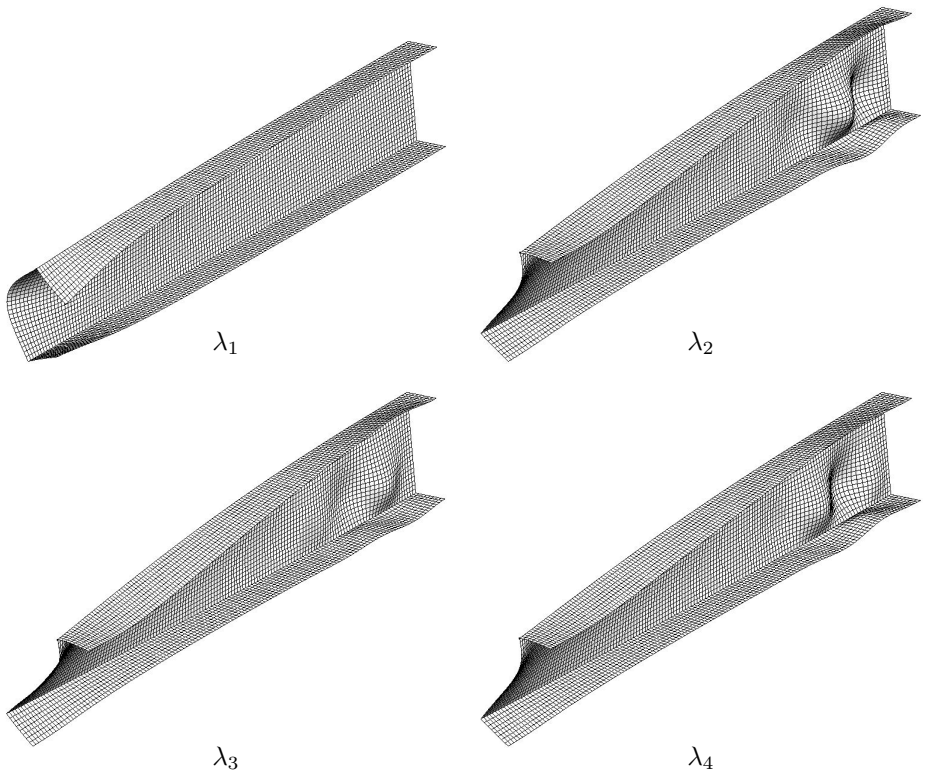

λ_1 λ_2 λ_3 λ_4

Figure 3.13: Clamped beam with C-section for LSS=LSS_1. Buckling modes corresponding to buckling loads $\lambda_1..\lambda_4$.

		% error			
a/t	Mesh	$\bar{w}^A$	$\bar{M}_x^A$	$\bar{M}_y^A$	$\bar{S}_y^D$
10	4x4	2.818	0.413	2.057	-27.937
	8x8	0.54	-0.211	0.038	-15.242
	16x16	0.097	-0.1	-0.084	-7.994
	32x32	0.011	-0.034	-0.034	-4.096
	64x64	0	-0.014	-0.014	-2.071
20	4x4	2.313	-0.345	1.507	-28.723
	8x8	0.397	-0.32	-0.02	-15.368
	16x16	0.055	-0.121	-0.091	-8.029
	32x32	0	-0.04	-0.036	-4.109
	64x64	0	-0.016	-0.014	-2.08
100	4x4	2.066	-0.465	1.573	-29.419
	8x8	0.329	-0.366	-0.034	-15.88
	16x16	0.045	-0.128	-0.088	-8.1
	32x32	0	-0.042	-0.036	-4.11
	64x64	0	-0.016	-0.016	-2.078
		Dimensionless analytical values			
a/t	-	$\bar{w}^A$	$\bar{M}_x^A$	$\bar{M}_y^A$	$\bar{S}_y^D$
10	-	-0.926	7.126	4.419	-37.18
20	-	-0.731	7.274	4.413	-37.117
100	-	-0.668	7.326	4.412	-37.109

Table 3.4: Percentage error with respect to the analytical solution values [85] on the transversal displacement at point A, bending moments at point A and shear force at point D, for regular mesh and span-to-thickness ratios on a simply supported square plate $[30/-60/60/-30]$ under uniform distributed load.

mesh	λ_1	λ_2	λ_3	λ_4	λ_5	λ_6
4x4	1.757	4.505	11.140	11.852	17.938	19.140
8x8	1.548	3.575	7.083	8.008	10.677	11.827
16x16	1.500	3.365	6.202	7.166	8.9565	10.438
32x32	1.489	3.315	6.006	6.968	8.5765	10.131
64x64	1.486	3.303	5.959	6.911	8.4855	10.057
64x64 (S8R)	1.486	3.299	5.944	6.904	8.460	10.033

Table 3.5: Square plate $[0/90/90/0]_S$ under uniaxial compression. Convergence of buckling loads with mesh refinement.

3.3.3 Clamped box under torsional couple

The buckling analysis of a clamped box under torsional couple is presented here. The geometry, boundary conditions, and load are shown in Fig. (3.14). The geometrical data are $l = 1000$ mm, $a = 100$ mm and $t = 10$ mm. The line load is $q = 25$ kN/mm. Two LLS are considered: $[45/-45/45/-45/45]_s$ and $[15/-15/15/-15/15]_s$. The elastic modula for the lamina are: $E_1 = 104$ GPa; $E_2 = 10.3$ GPa; $G_{12} = 5.15$ GPa and $\nu_{12} = 0.021$.

The lower four buckling modes are listed in Table 3.7, where comparison with S8R elements have been made, and h^2 convergence is shown in Fig. 3.15. Finally, buckling modes, for LSS $[45/-45/45/-45/45]_s$, are shown in Fig. 3.16.

	LSS_1				LSS_2			
mesh	λ_1	λ_2	λ_3	λ_4	λ_1	λ_2	λ_3	λ_4
2	1.1209	1.5855	2.1198	2.1807	0.6902	1.6842	2.0256	2.0550
4	1.1010	1.5750	1.6623	1.6963	0.6714	1.5714	1.6667	1.6882
8	1.0952	1.5483	1.5767	1.5859	0.6668	1.5299	1.5836	1.6029
16	1.0935	1.5242	1.5541	1.5760	0.6657	1.5186	1.5633	1.5811
16 (S8R)	1.0736	1.5164	1.5450	1.5919	0.6670	1.5200	1.5865	1.6080

Table 3.6: Clamped beam C-section for different LSS. Convergence of buckling loads with mesh refinement. The values on the first column refer to the numbers of the element along b.

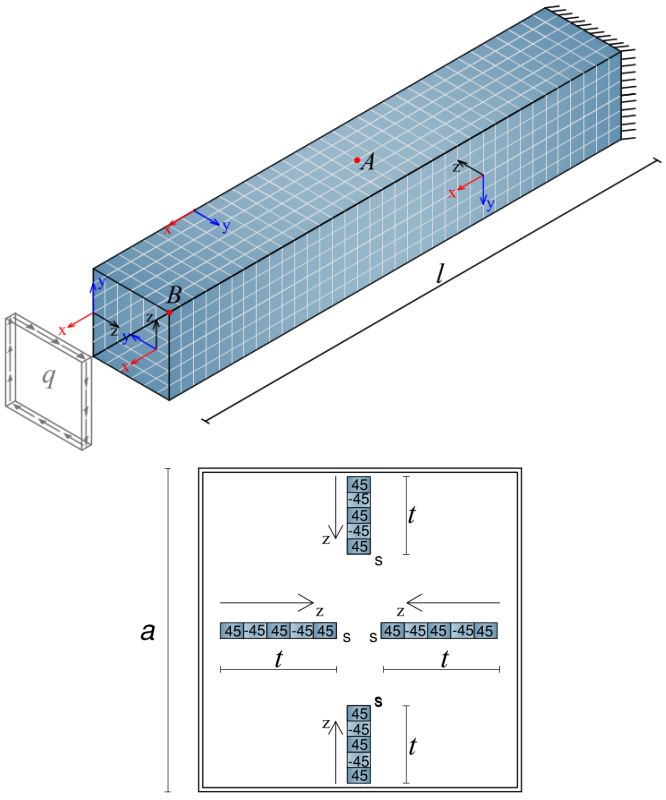

Figure 3.14: Geometry, boundary conditions, and load for clamped box subjected to torque load.

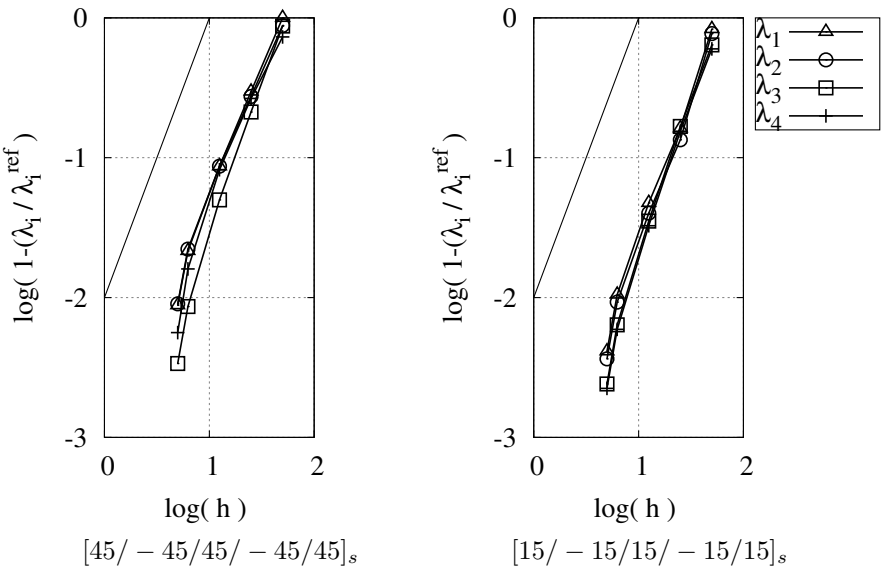

$[45/-45/45/-45/45]_s$ $[15/-15/15/-15/15]_s$

Figure 3.15: Clamped box under torsional couple for different LSS. Convergence of buckling loads with mesh refinement. The solid line represents h^2 (for reference).

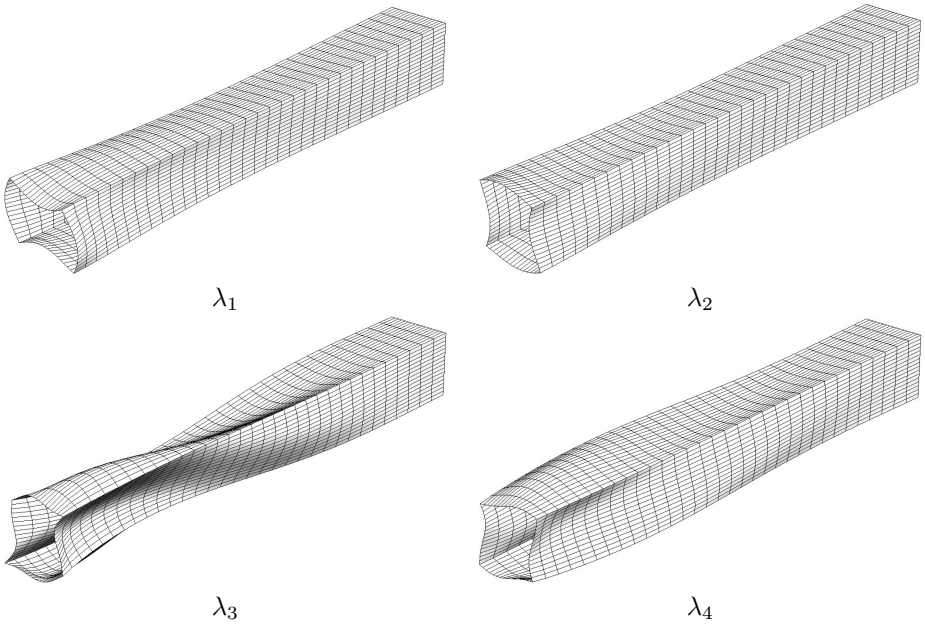

λ_1 λ_2

λ_3 λ_4

Figure 3.16: Clamped box under torsional couple with LSS $[45/-45/45/-45/45]_s$. Buckling modes corresponding to buckling loads $\lambda_1 \cdots \lambda_4$.

	$[45/-45/45/-45/45]_s$				$[15/-15/15/-15/15]_s$			
mesh	λ_1	λ_2	λ_3	λ_4	λ_1	λ_2	λ_3	λ_4
2	424.81	453.06	488.72	535.83	195.29	204.22	272.38	278.44
4	241.50	306.71	316.28	391.71	123.95	130.78	193.82	200.86
8	202.34	261.70	273.92	334.97	111.71	119.92	171.88	179.67
16	190.19	246.10	263.15	314.52	107.76	116.36	167.09	175.02
20	187.82	242.93	261.78	311.30	107.08	115.71	166.43	174.38
24	186.18	240.76	260.90	309.56	106.64	115.29	166.03	173.99
24 (S8R)	184.83	242.78	258.47	307.13	106.53	115.63	165.14	173.40

Table 3.7: Clamped box under torsional couple for different LSS. Convergence of buckling loads with mesh refinement. The values on the first column refer to the numbers of the element along a.

3.4 Further remarks

A simple mixed quadrilateral 3D plate finite element with 6 dof/node for linear static and buckling analysis of plate/folded plate has been presented. An assessment of performance is given. In the linear analysis case, numerical results show a global convergence h^2 measured in s-norm for different LSS and thickness-to-span ratios. The point-wise convergence is comparable to that of displacement based elements with higher number of dof, such as S8R. This makes the proposed element particularly suitable for stress resultant recovery in the case of coarse meshes. The use of drilling rotation, within a symmetric formulation and without penalty functions (thus avoiding spurious modes), and accurate evaluation of displacements and rotation, makes the element suitable for folded plate structures and geometrically nonlinear analysis when coupled with a corotational formulation. The same behavior shown in linear analysis of plates is preserved for linear analysis and buckling analysis of folded plates. Not only h^2 convergence is shown for the evaluation of buckling loads but also very low errors are seen, on average, for coarse meshes.

Chapter 4

Koiter asymptotic analysis of laminated composite plates

4.1 Introduction

In the following, three benchmarks are analyzed using Koiter asymptotic analysis. The first is a simply supported plate under uniaxial compression with different LSS [86]. The accuracy in the recovery critical and post-critical behavior are shown and the performance in terms of computational cost are compared with Riks path-following analysis. The second is a hinged cylindrical roof, that is a classical test [119] with a strong non linear precritical behavior and, as in the first benchmark, with a post-critical dominated by the first buckling mode. The last is a channel column, studied experimentally by [120] and aimed to show the accuracy and good performance in the analysis of folded plate including buckling mode interaction [20].

The accuracy and reliability of the results are closely related to the use of geometrically exact structural models and mixed formulation, the latter is necessary to prevent extrapolation locking phenomena [14]. The use of a corotational formulation coupled with a mixed finite element allows to easily satisfy previous requirements.

Moreover, Koiter approach being based on asymptotic expansion, allows to recover the equilibrium path in an approximate fashion. The best accuracy is available for the precritical and the initial post-critical behavior. A study of convergence can be found in [121], for the Koiter asymptotic approach called simple linear algorithm as proposed in [14] and very good results was proven. The currently used approach called full quadratic algorithm (see [6] and references therein) has shown better performance than simple linear one in all experiences done.

4.2 Square plate under compression

The buckling and post-buckling analysis of a laminated, simply-supported square plate under uniaxial membrane load [86] is presented and comparison with Riks path-following analysis using ABAQUS [84] is made. The lamina materials properties are $E_1 = 181$ GPa, $E_2 = 10.27$ GPa, $G_{12} = 7.17$ GPa, ν_{12} =0.28. The thickness is $t = 1.27210^{-4}$ m while the length is $l = 0.508$ m.

To evaluate accuracy, an test is performed for a simply supported $[0/90]_{4S}$ square plate ($h \times h$) subjected to uniaxial edge pressure λ. The critical loads are listed in Table 4.1 and the buckling modes are shown in Fig. 4.1. Note that h^2 convergence is achieved for critical values as shown in Fig. 4.2.

$[0/90]_{4S}$				
mesh	λ_1	λ_2	λ_3	λ_4
4x4	1.7562	5.0349	12.089	12.543
8x8	1.5472	4.0021	7.0816	9.0840
16x16	1.5002	3.7684	6.2008	8.1365
32x32	1.4892	3.7126	6.0054	7.9138
64x64	1.4867	3.6990	5.9588	7.8593
64x64 (S8R)	1.4861	3.6947	5.9443	7.8414

Table 4.1: Square plate under uniaxial compression. Convergence of buckling loads with mesh refinement.

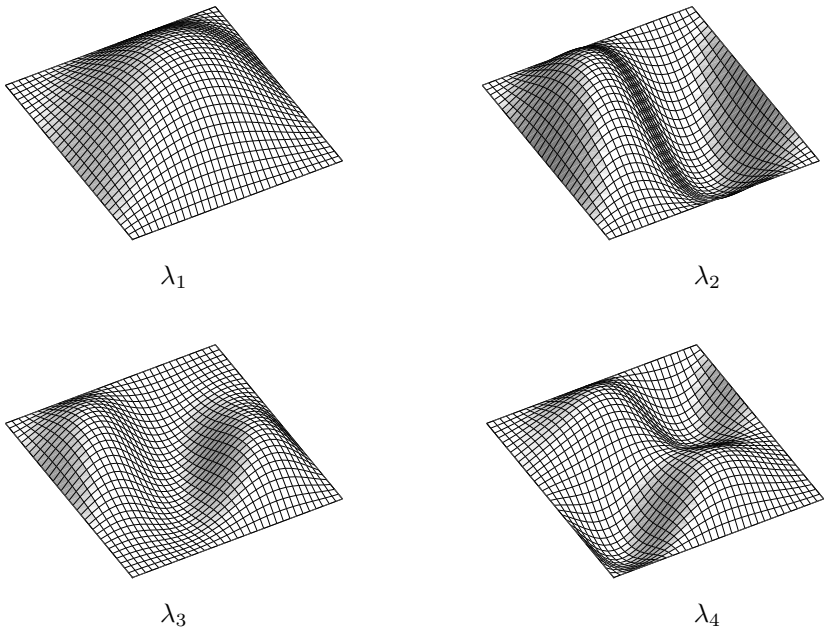

Figure 4.1: Square plate under uniaxial compression. Buckling modes corresponding to buckling loads $\lambda_1, \cdots, \lambda_4$.

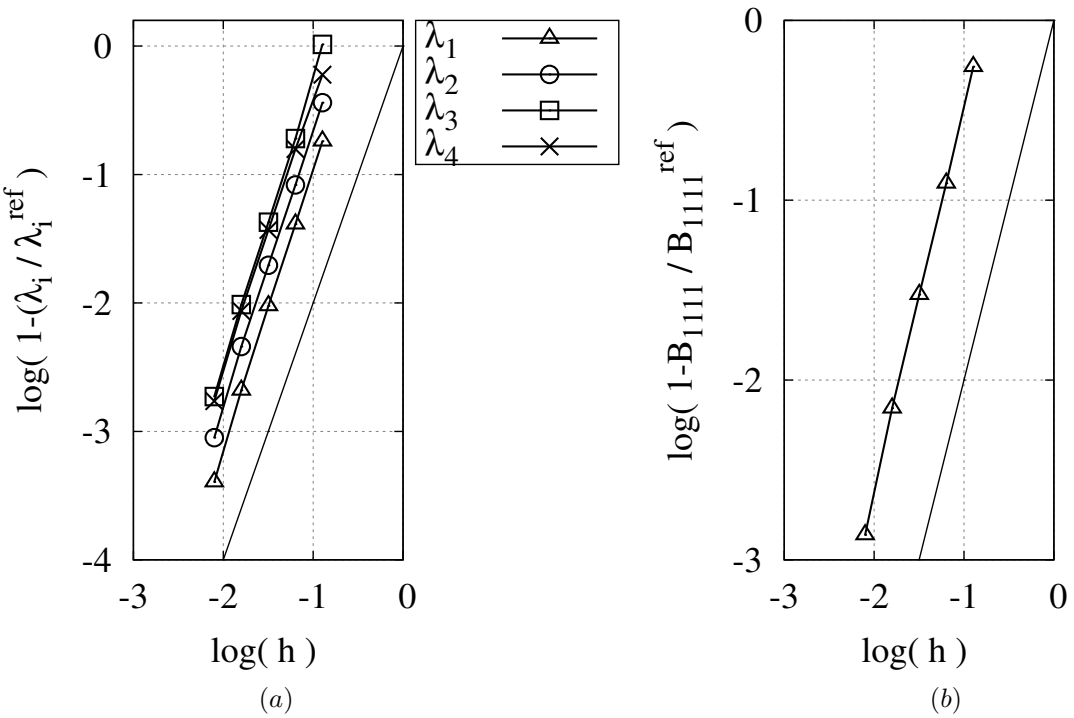

(a) (b)

Figure 4.2: Square plate ($h \times h$) under uniaxial compression. (a) convergence of buckling loads and (b) convergence of post-critical quartic form. Solid line is for reference.

Then, the accuracy of the post-critical behavior is investigated by looking at the convergence of the fourth order form $\mathbb{B}_{ijhk}$ [6], which is reported in Fig. 4.2, showing convergence of of order h^2.

Then, the post-critical behavior for different LLS was calculated. The equilibrium paths graphed in Fig. 4.3 when compared with those obtained using path-following analysis confirm good accuracy both the pre-critical and in the initial post-critical behavior. As expected, up to the initial post-critical range the two equilibrium paths coincide while over the accuracy gradually decrease.

Finally, to compare the performance of Koiter's analysis with that of Riks path–following analysis, the computational cost of one analysis is reported. The aim is to evaluate the time needed for both analysis. For Koiter analysis, a 64x64 element mesh (about 25000 dofs) was employed to analyze only one imperfection. The most time is spent performing the linear analysis (see eq. 3 in [8]), the buckling (see eq. 4 in [8]) and to evaluate the post-critical energy variations (see eq. 8 in [8]). Just a little fraction of the time is spent to recover the equilibrium path (eq. 9 in [8]). Note that only the last step needs to be redone for analyzing a different imperfection. The total time spent for each problem was about 12 seconds, where less than a tenth of second was spent for recovering the equilibrium path.

The Riks analysis is performed using a coarser, 40x40 mesh of linear S4R elements (about 9600 dofs) in Abaqus. The analysis is particularly sensible to the Risk control settings, including

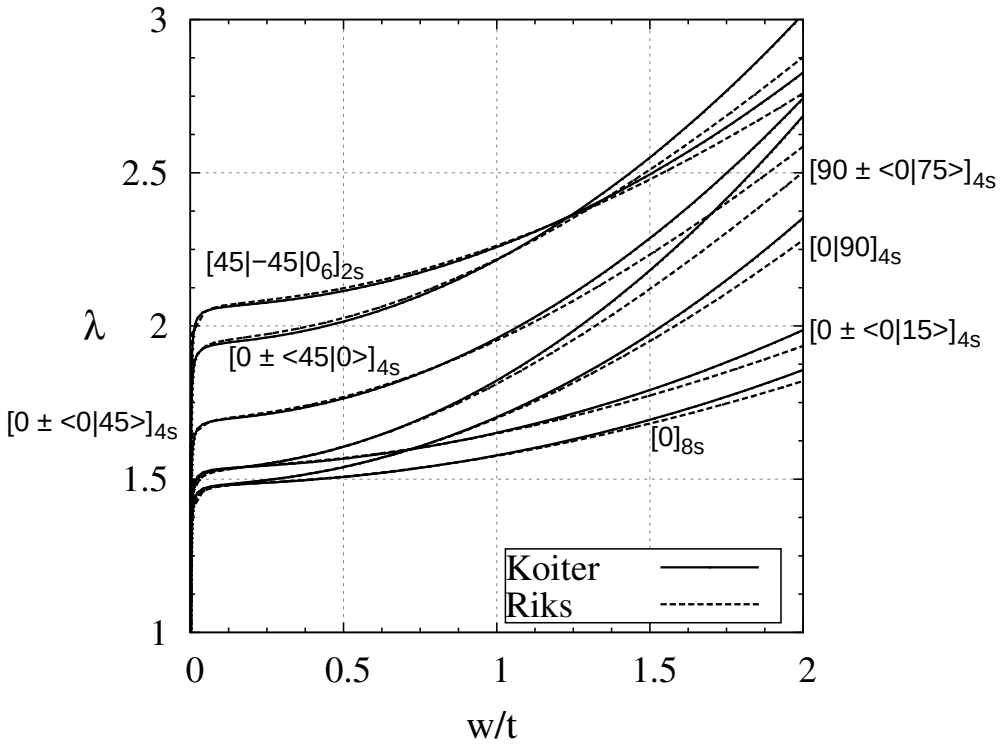

Figure 4.3: Square plate under compression. Equilibrium paths recovered using Koiter asymptotic analysis compared with that obtain Riks analysis. The load factor is indicated with λ while w denotes the transversal displacement of the center of the plate.

the initial imperfection, which must be chosen by the analyst either in the load or in the initial geometry. For this comparison only, a geometrical imperfection in the form of the first buckling mode with the maximum magnitude displacement equal to 10^{-4} mm is used. The initial step length is assumed to be a tenth of the total arc length, and the later is assumed to be 1.0. The maximum incrementation is assumed to be 10. The other Riks control settings are left at their Abaqus default values. These control settings are optimized trough a careful tuning for this particular test. Note that each new test needs news settings.

Each Riks analysis takes about 60 steps within a 1 or 2 equilibrium iterations, which impose matrix reforming, decomposition, and solving a linear system for each iteration. Note that the run must be fully redone for each new imperfection. The total time spent for one imperfection is reported in Table 4.2. The computations are performed on a Intel(R) Xeon(R) CPU E5-2620 2.00Ghz Dual Core, 32 GB Ram on a single core for both, Koiter and Riks analysis.

A shown in Table 4.2, the Koiter analysis is faster for every analysis. Obviously, Koiter's analysis becomes even more efficient when different imperfections are analyzed. When analyzing multiple imperfections, each imperfection requires the same time for Riks analysis, while the cost of Koiter's analysis becomes becomes negligible because only the nonlinear system (see eq. 9 on [8]) needs to be solved.

problem	Koiter	Riks
1	11 s	39 s
2	14 s	38 s
3	13 s	54 s
4	13 s	37 s
5	11 s	36 s
6	13 s	58 s
7	13 s	44 s
Average	12.5 s	43.7 s

Table 4.2: Koiter's vs Riks analysis timing

4.3 Hinged cylindrical roof

The popular hinged cylindrical roof [119, 116] is analyzed in this section. The geometry, boundary condition and load are represented in Fig. 4.4. The lenght is $l = 2.54$ m, the radius is $R = 25.40$ m and the angle is $\beta = 0.1$ rad. The base load is $P = 10^3$ N.

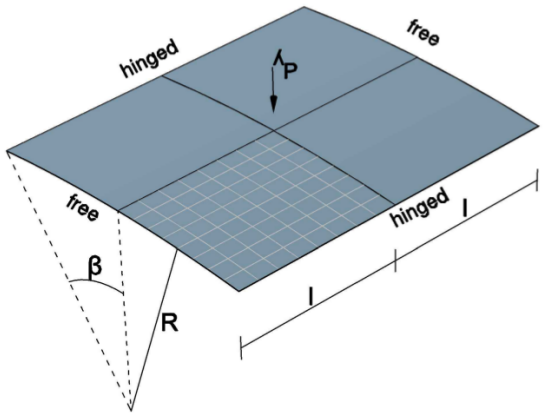

Figure 4.4: Hinged cylindrical roof. Geometry, boundary and load condition.

Three cases are considered. The first is a single layer with isotropic material and elastic modula $E = 3102.75$ MPa, $\nu = 0.3$ and the thickness $t = 0.127$ m. The second and the third are laminated composite with LSS [0/90/0] and [90/0/90] respectively. The materials constants are $E_1 = 3300$ MPa, $E_2 = 1100$ Mpa, $G_{12} = 660$ Mpa, $\nu = 0.25$, and the thickness is $t = 0.127$ m. The interesting aspect of this test is the strong nonlinearity of the pre-critical path. The first buckling load is $\lambda_1 = 4.5607$ for isotropic single layer, $\lambda_1 = 3.5849$ and $\lambda_1 = 2.2177$ for LSS [0/90/0] and [90/0/90] respectively. The corresponding mode is represented in Fig. 4.5 for isotropic single layer.

The equilibrium path recovered for laminated composite and for isotropic material are reported in Fig 4.6 in comparison with Riks analysis. Note that the limit load is about one-half of the value of the first buckling load, for all cases.

The good representation of pre-critical behavior, limit load, and initial post-critical path

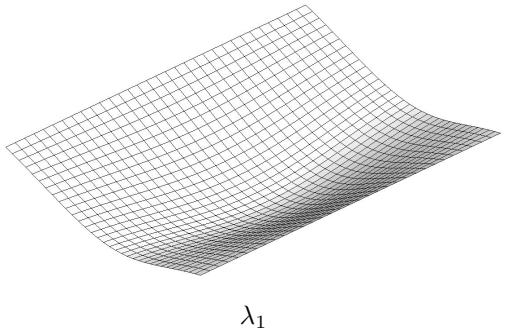

Figure 4.5: Hinged cylindrical roof. Buckling mode corresponding to buckling load λ_1.

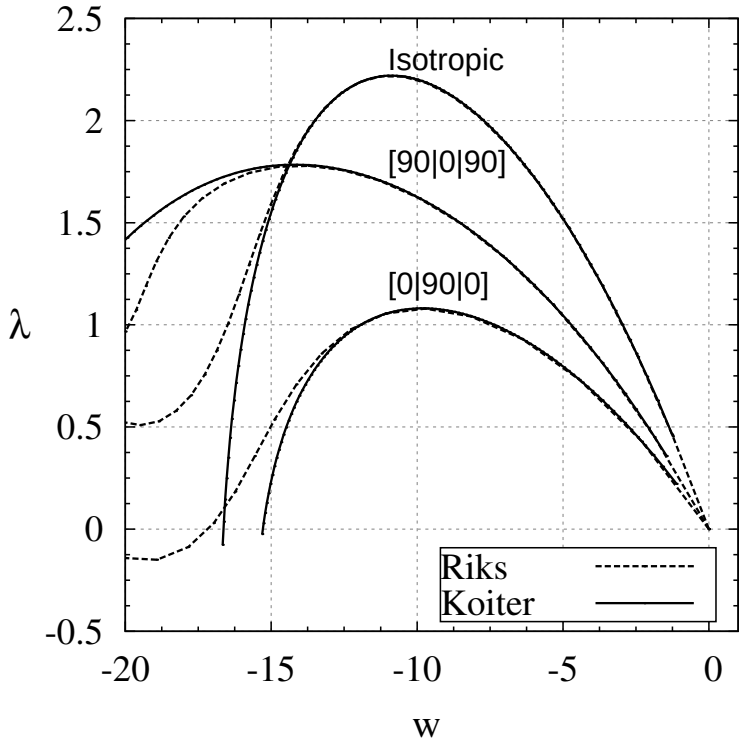

Figure 4.6: Hinged cylindrical roofs. Equilibrium paths. The load factor is indicated with λ while denotes w (mm) is the transversal displacement of the center of the cylindrical roofs.

is clear also in Fig. 4.6 for this particularly difficult case. Really, the Koiter equilibrium path coincide with that of Riks analysis up to the limit point. The expected accuracy is shown while over the limit point the accuracy gradually decrease.

4.4 Channel section under compression

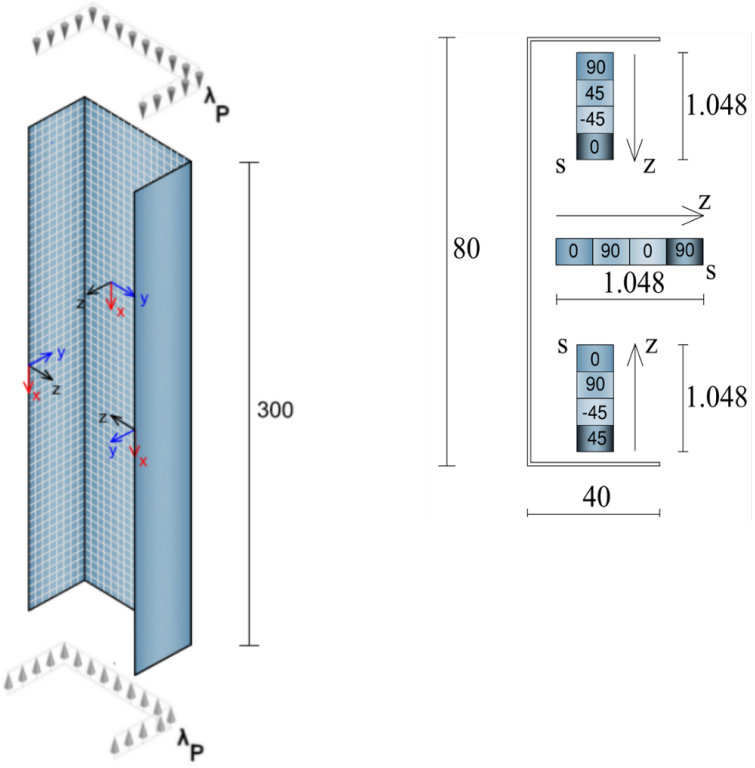

Figure 4.7: Channel section. Geometry, boundary, and load conditions. Dimensions are expressed in mm.

A channel section under compression is analyzed next. Experimental results for this problem are available in [120], being one of their more recent results in this field [122, 123, 124]. The geometry, load, and boundary conditions, as well as the LSS for each panel of the channel section are reported in Fig. 4.7.

The material data are $E_1 = 130.71$ GPa, $E_2 = 6.36$ GPa, $G_{12} = 4.18$ GPa, $\nu = 0.32$. The results of buckling analysis are reported in Fig. 4.8 for the six lower buckling modes. The analysis is performed with a fine mesh (16 elements on the wings, 32 on the web, and 120 along the height). Mode deflections involve both the wings and the web. Moreover, some of the critical loads are very close.

The equilibrium paths are reported in Fig. 4.9. Koiter's analysis is performed with a rough mesh (8 element on the wings, 16 on the web, and 60 along the height). The first six modes

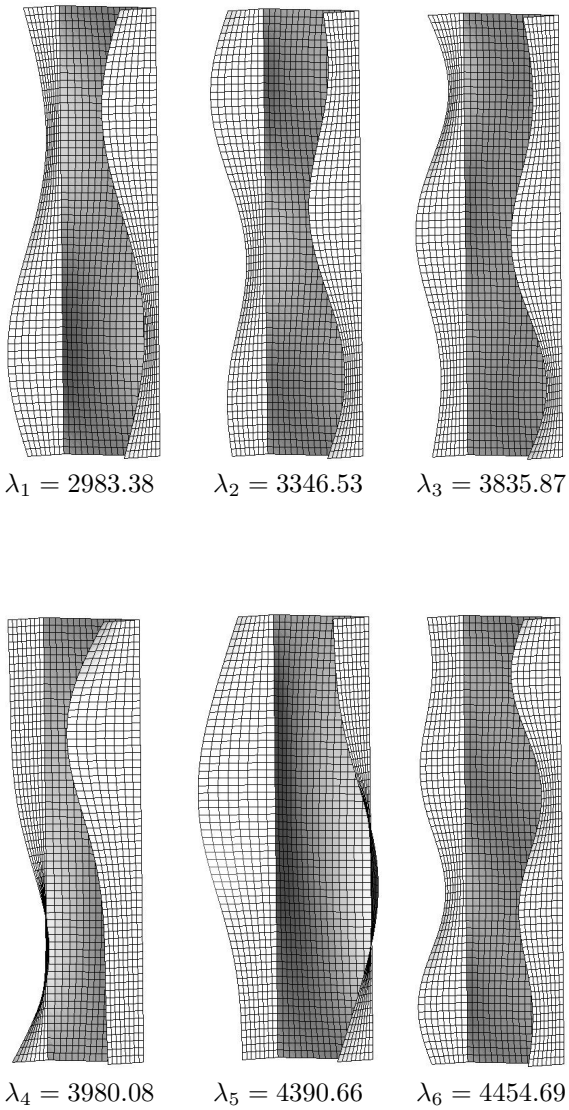

Figure 4.8: Channel section. Buckling modes corresponding to buckling loads $\lambda_1, \lambda_2, \cdots \lambda_6$.

are reported. Two displacements components are plotted: the axial displacement u (mm) of the end section and the transversal displacement w (mm) at a quarter of the height in the center of the web. The equilibrium path recovered with Koiter's analysis is compared with Rik's path-following analysis. The results clearly show the accuracy in the recovery the initial post-critical behavior.

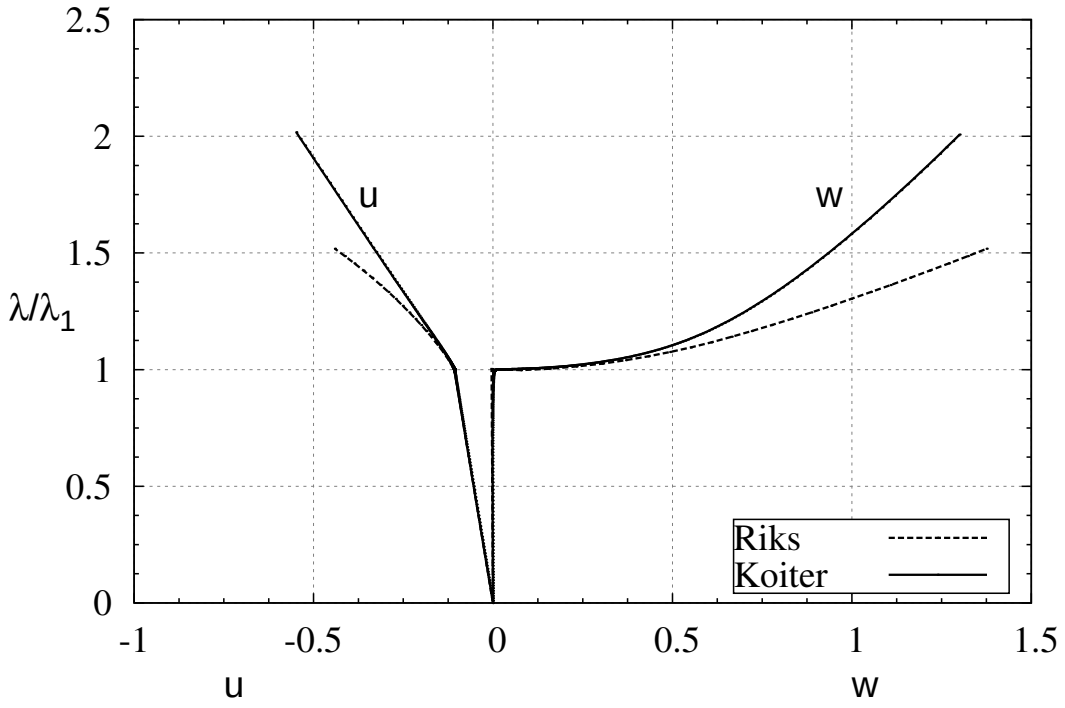

Figure 4.9: Channel section. Equilibrium paths recovered using Koiter asymptotic analysis compared with that obtain Riks analysis. Load factor is indicated with λ and it is normalized on the first buckling load λ_1. In the abscissa are plotted the axial displacement u of the end section and the transversal displacement w at a quarter of the height in the center of the web.

4.5 Further remarks

Koiter's asymptotic analysis represents a valid, less computational expensive alternative to Riks path-following analysis for the recovery the initial post-critical behavior of composite structures, even those displaying strong pre-critical behavior and buckling mode interaction. Its use in the context of laminated composite folded plate (shell) structures has been demonstrated (see also [48]). The accuracy of the proposed element has been checked and the convergence of the critical and post-critical quantities show good performance, which can be attributed to the simplicity of the linear finite element employed and the choice of corotational formulation for the extension to nonlinear analysis of folded laminated composites. The computational cost has

been monitored and the results show the advantage of Koiter's analysis versus Riks analysis, including considerations of accuracy and robustness for difficult test cases.

Chapter 5

Imperfection sensitivity analysis

5.1 A rack member in compression

In the following, an imperfection sensitivity analysis for RS 125 x 3.2 upright pallet racks in compression with and without perforations (net and brut) is presented. In the following, the brut section is indicated with the acronym RSB, while the perforated section with RSN. The geometry of the cross-section is shown in Fig. (5.1), while the details relating to the cross-section, perforations, material, experimental tests and numerical simulations can be found in [94, 95], the thickness considered for RSB and RSN sections is equal to 3.2 mm.

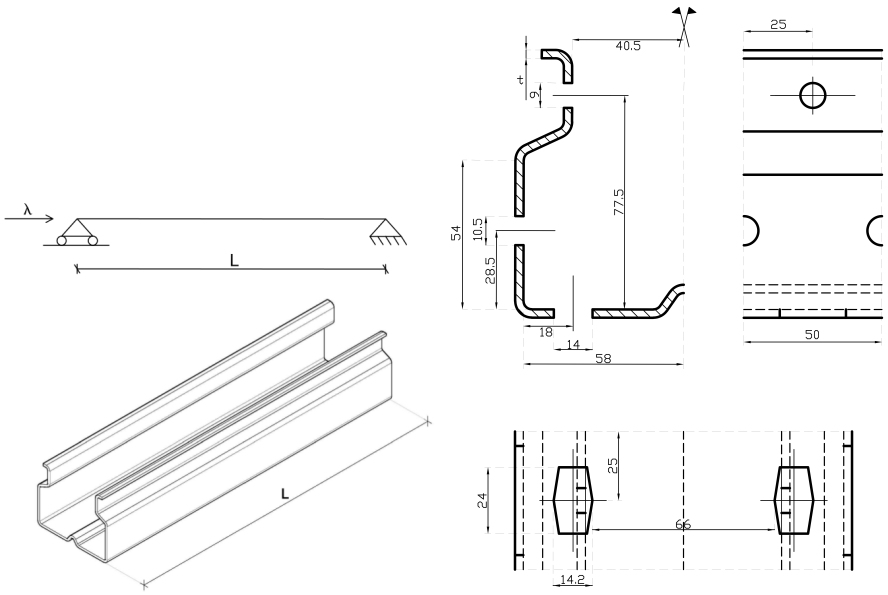

Figure 5.1: Geometry of RS 125 section (dimensions are expressed in mm) and boundary conditions.

The experimental work done in [94] covers various lengths of the columns, i.e. (i) stub columns; (ii) upright member specimens to check the influence of distortional buckling; (iii)

specimens of lengths equal to the half-wave length of distortional buckling; (iv) specimens of lengths corresponding to interactive buckling range. It is well known that the effect of imperfections is at its maximum in the interactive buckling range. Due to the coupling of buckling modes and imperfections the ultimate load drops significantly. According to [94] the interactive point is 2200 mm. Our interest is to see the influence of imperfections in the coupling range and the participation of the buckling modes. Consequently, the lengths considered in the analyses range from 1400 mm to 2500 mm. Increments of 100 mm have been considered. Firstly, only geometrical imperfections have been considered, in particular the $\tilde{u}$ (see Eqs. (1.8) and (1.9)) being assumed as

$$\tilde{u} = \tilde{u}^g + \tilde{u}^d \tag{5.1}$$

where $\tilde{u}^g$ and $\tilde{u}^d$ are global and distortional/local imperfections that are assumed as linear combinations of global $\dot{v}_i^g$ and distortional/local $\dot{v}_i^d$ buckling modes, that is

$$\tilde{u}^{(g)} = \sum_i r_i \dot{v}_i^g \;\; i = 1 \cdots m^g \quad , \quad \tilde{u}^{(d)} = \sum_i r_i \dot{v}_i^d \;\; i = 1 \cdots m^d \tag{5.2}$$

where r_i are random numbers, and m^g and m^d are the number of global and distortional/local buckling modes. The maximum values of $\tilde{u}^g_{max}$ and $\tilde{u}^d_{max}$ are assumed to be less than those of a assumed tolerances

$$\tilde{u}^g_{max} \leq \tilde{u}^g_{tol} \quad , \quad \tilde{u}^d_{max} \leq \tilde{u}^d_{tol} \tag{5.3}$$

with $\tilde{u}^g_{tol} = L/1000$ and $\tilde{u}^d_{tol} = 1.5 \cdot t$, where L and t are, respectively, the thickness and the length of the upright pallet rack (see Fig.5.1).

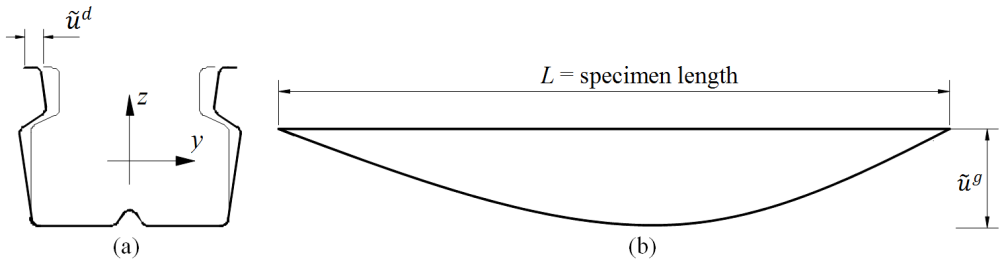

Figure 5.2: Type of imperfections for numerical analysis (a) distortional and (b) global.

Note that geometrical imperfections with a shape different from Eq. 5.2 can be considered (for more details see [98]). However, our aim is to find the worst cases of Eq. 1.7h in terms of minimum limit load so only geometric imperfections in the space of the buckling modes have been considered. The random process Eq. 5.2 is used to reach the previous goal. In our framework, the distribution of random numbers does not have any relationship with real imperfection distribution. A uniform distribution is employed but after their generation, the

random numbers are scaled so that Eq. 5.3 are satisfied with regard to the equality. In fact, assuming an equal shape for the imperfection the minimum limit load depends on their maximum amplitude.

From a computational point of view, the Koiter asymptotic analysis (see Eqs. (1)) has been performed using a corotational approach [9] within a mixed formulation based on MISS-4 finite element [15]. Further details about the implementation of this can be found in [11].

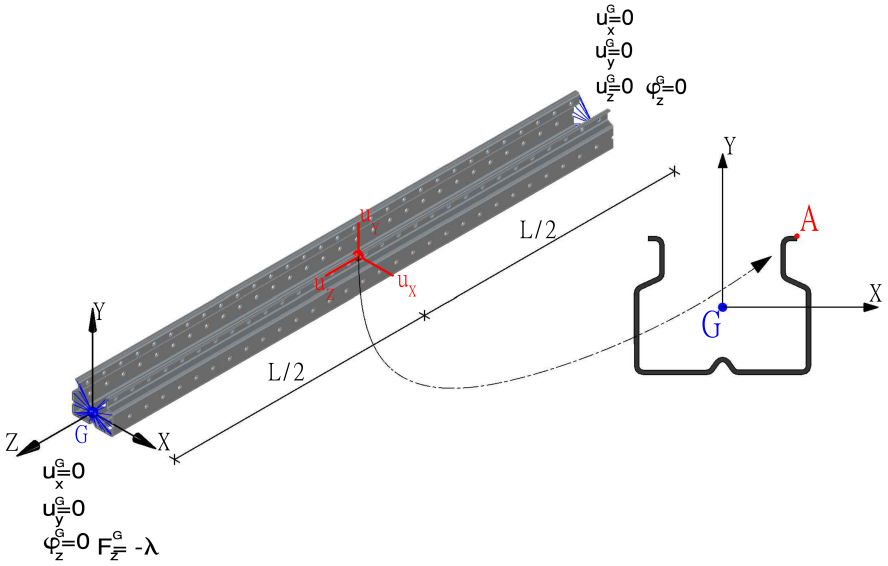

Figure 5.3: Geometry, boundary conditions of the member, reference point ("A") for displacements.

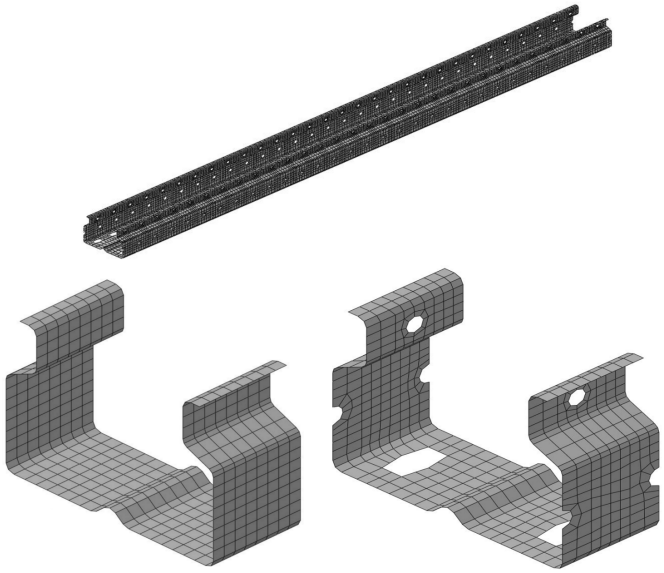

Figure 5.4: Detail of mesh for RS 125 x 3.2 section.

5.1.1 Buckling analysis

For each length, the first four buckling modes (see Eq. (1.7c)) are considered (see Tables (5.1) for RSB 125 x 3.2 and (5.2) for RSN 125 x 3.2, respectively). For the numerical simulation the end supports of the rack were modelled as they were in the experimental tests, i.e. pinned at one end and simply supported at the other, with rotation restrained at both ends as shown in Fig.(5.3). The details of the mesh are shown in Fig. (5.4).

Eight distortional buckling modes and two global buckling mode have been detected, as shown in Tables (5.1), (5.2) and Figs. (5.5), (5.6). For each of the buckling modes the following abbreviations have been used, for the consider length range, i.e. $1400 - 2500$ mm, i.e. S - symmetric, A - antisymmetric, F - flexural and FT - flexural torsional buckling. Fig. (5.9) shows the buckling loads and lengths of the upright members. The lengths corresponding to global/distorsional interactive buckling can be clearly seen, i.e. 2200 mm.

L (mm)	λ_1	Mode	λ_2	Mode	λ_3	Mode	λ_4	Mode
1400	507.20	$d1$ S	532.56	$d2$ S	712.98	$d3$ A	747.96	$d4$ A
1500	505.62	$d1$ S	509.71	$d2$ S	696.83	$d4$ A	698.64	$d3$ A
1600	492.74	$d2$ S	504.91	$d1$ S	663.13	$d4$ A	686.27	$d3$ A
1700	481.05	$d2$ S	501.60	$d1$ S	643.12	$d4$ A	677.45	$d3$ A
1800	473.77	$d2$ S	494.39	$d6$ S	635.60	$d4$ A	652.43	$d5$ S
1900	469.95	$d2$ S	484.83	$d6$ S	611.59	$d4$ A	632.25	$d5$ S
2000	468.51	$d2$ S	475.23	$d6$ S	563.65	$e1$ F	593.01	$d5$ S
2100	467.00	$d6$ S	468.23	$d7$ S	516.16	$e1$ F	550.02	$e2$ FT
2200	460.69	$d6$ S	467.60	$d7$ S	473.42	$e1$ F	509.33	$e2$ FT
2300	435.12	$e1$ F	456.36	$d6$ S	465.88	$d7$ S	471.94	$e2$ FT
2400	401.18	$e1$ F	437.92	$e2$ FT	453.77	$d6$ S	462.39	$d8$ S
2500	370.90	$e1$ F	407.09	$e2$ FT	452.58	$d6$ S	458.01	$d8$ S

Table 5.1: The first four buckling loads corresponding to the investigated length range for RSB 125 x 3.2 section. The buckling loads are expressed in kN. The buckling modes specified by letters d (d_1, d_2 ... d_8) and e (e_1, e_2) are respectively distorsional and global. The abbreviations S, A, F and FT indicate respectively: symmetric, antisymmetric, flexural and flexural torsional (see Fig. 5.5).

5.1.2 Post-buckling and imperfection sensitivity analysis

The post-buckling behavior (see Eq. (1.7h)) for the members with lengths $L = 1400$ ... 2500 mm have been analysed. The multimodal analysis has been performed considering the four buckling modes presented above. Five hundred random geometric imperfections have been considered. The equilibrium paths for RSN 125 x 3.2 with length $L = 2000$ mm have been reported in Figs. 5.12 and 5.13. This length (see Fig. (5.18)) shows a strong erosion (i.e. the reduction in minimum critical load) even if the buckling modes are not so coincident. In the Fig. 5.12, the equilibrium paths in terms of load amplification factor λ normalized on the minimum critical load λ_{min} versus the modal amplitude $\xi_i, \quad i = 1..4$ are presented. Each modal component ξ_i

L (mm)	λ_1	Mode	λ_2	Mode	λ_3	Mode	λ_4	Mode
1400	441.77	d_1 S	474.30	d_2 S	627.87	d_3 A	652.37	d_4 A
1500	438.64	d_1 S	452.94	d_2 S	610.10	d_3 A	626.31	d_5 S
1600	436.14	d_2 S	437.97	d_1 S	589.27	d_5 S	597.46	d_3 A
1700	423.80	d_2 S	436.98	d_1 S	564.69	d_5 S	586.87	d_3 A
1800	415.38	d_2 S	433.41	d_1 S	551.71	d_5 S	573.22	d_3 A
1900	410.20	d_2 S	426.92	d_7 S	546.53	d_6 S	547.35	d_3 A
2000	407.55	d_2 S	419.02	d_7 S	504.71	e_1 F	516.26	d_3 A
2100	406.60	d_2 S	411.34	d_7 S	463.19	e_1 F	480.49	e_2 FT
2200	404.82	d_7 S	406.41	d_2 S	425.29	e_1 F	445.97	e_2 FT
2300	391.28	e_1 F	399.81	d_7 S	405.97	d_2 S	413.88	e_2 FT
2400	360.93	e_1 F	384.47	e_2 FT	396.33	d_7 S	404.40	d_2 S
2500	333.79	e_1 F	357.73	e_2 FT	394.21	d_7 S	401.55	d_8 S

Table 5.2: The first four buckling loads corresponding to the investigated length range for RSN 125 x 3.2 section. The buckling loads are expressed in kN. The buckling modes specified by letters d (d_1, d_2 ... d_8) and e (e_1, e_2) are respectively distorsional and global. The abbreviations S, A, F and FT indicate respectively: symmetric, antisymmetric, flexural and flexural torsional (see Fig. 5.6).

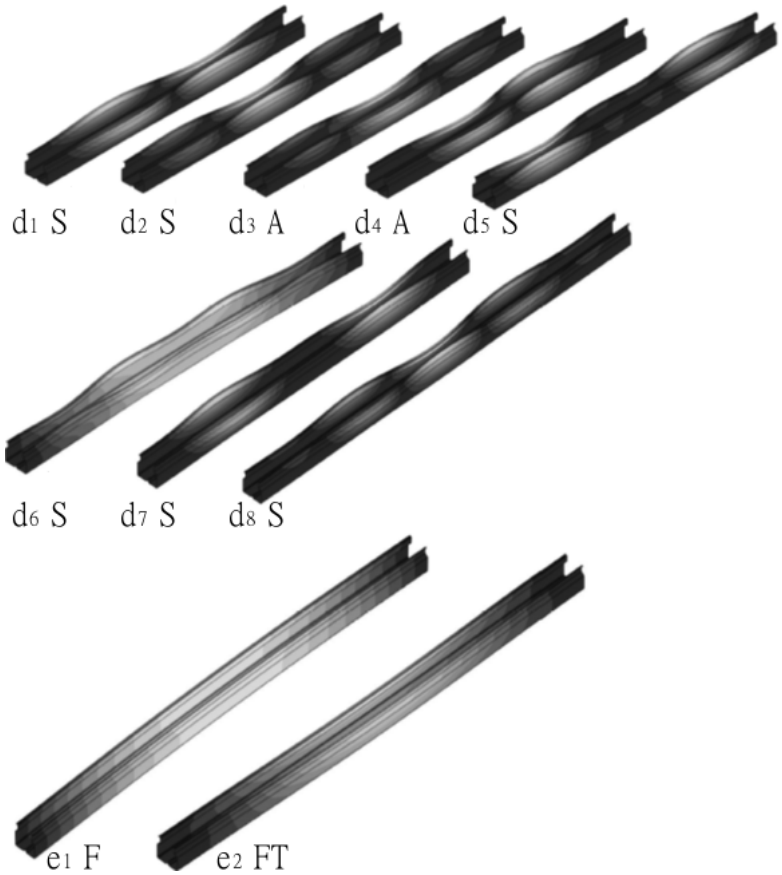

Figure 5.5: Distorsional d_1, d_2 ... d_8 and global e_1, e_2 buckling modes for RSB 125 x 3.2 section in the range $L = 1400$ ... 2500 mm.

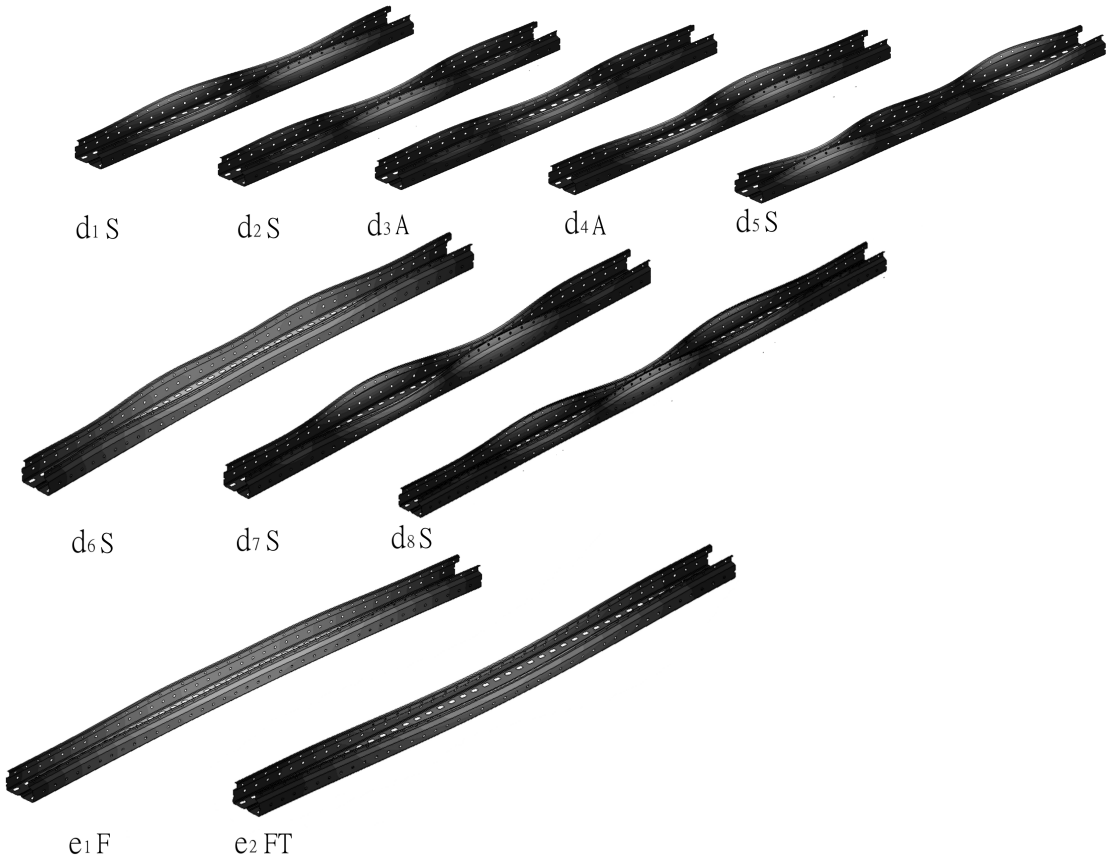

Figure 5.6: Distorsional d_1, d_2 ... d_8 and global e_1, e_2 buckling modes for RSN 125 x 3.2 section in the range $L = 1400$ ... 2500 mm.

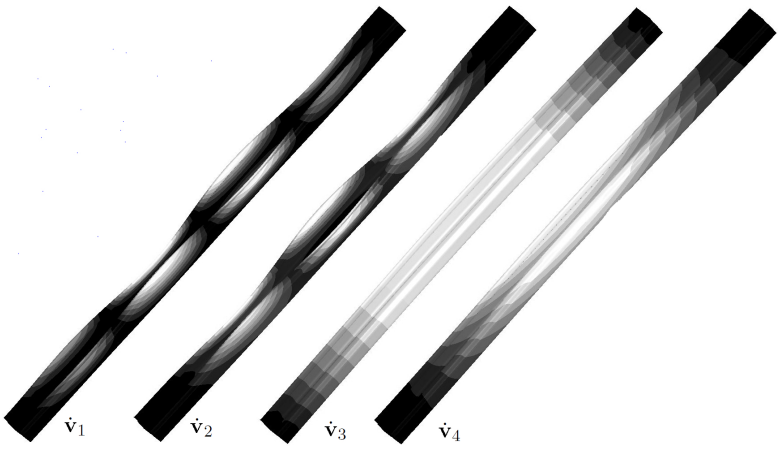

Figure 5.7: Buckling modes for RSB 125 x 3.2 section with $L = 2200$ mm.

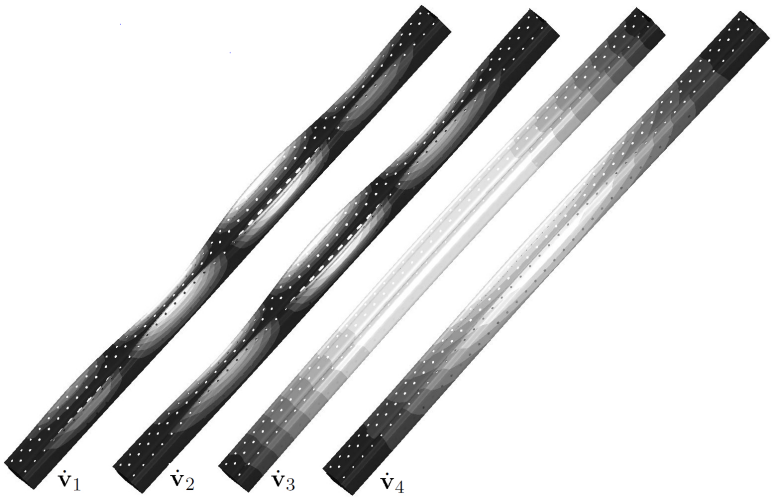

Figure 5.8: Buckling modes for RSN 125 x 3.2 section with $L = 2200\ mm$.

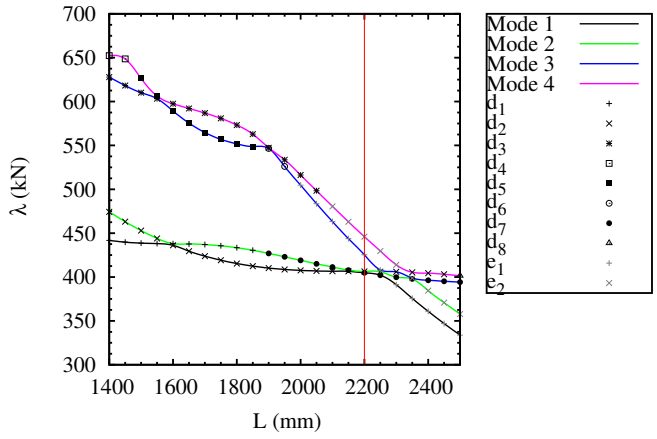

Figure 5.9: Buckling load and corresponding length for RSN 125 x 3.2 section. The length $L = 2200\ mm$ corresponding to global/distortional interactive buckling has been denoted.

has been represented using different colours. This graph clearly shows the modal interaction between the four modes because all ξ components have values other than zero. In the Fig. 5.13 the equilibrium paths in terms of λ versus the displacements are reported.

Finally, for the net section, other equilibrium paths for different lengths in terms of modal amplitude $\xi_i, \quad i = 1..4$ are presented in Figs. (5.14), following the mode classification given in Table (5.2) and Fig. (5.6). The graphs clearly show the modal interaction and type of interaction: distortional/distortional for the shorter specimens and global/distortional for the longer ones.

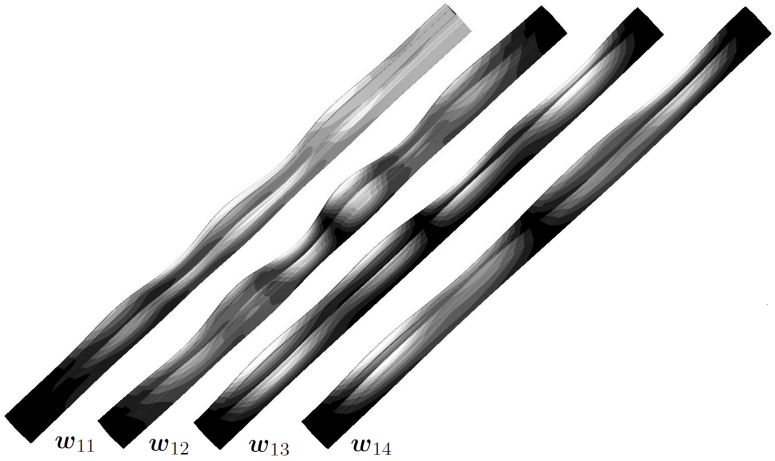

Figure 5.10: Quadratic corrections for RSB 125 x 3.2 section with $L = 2200\ mm$.

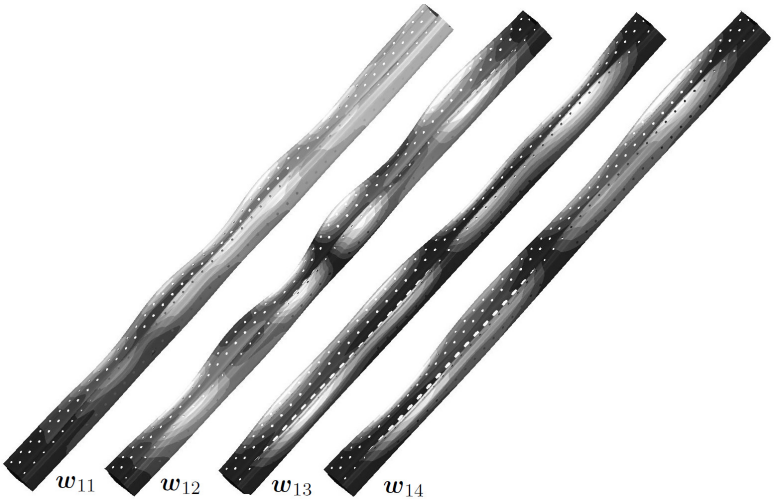

Figure 5.11: Quadratic corrections for RSN 125 x 3.2 section with $L = 2200\ mm$.

5.1.3 Limit load and worst case imperfection

The results of the post-buckling analysis have been summarized. The frequencies for the limit loads are reported in Fig. (5.15). For the specimens with strong buckling interaction , the values are very close to the peak of the distribution.

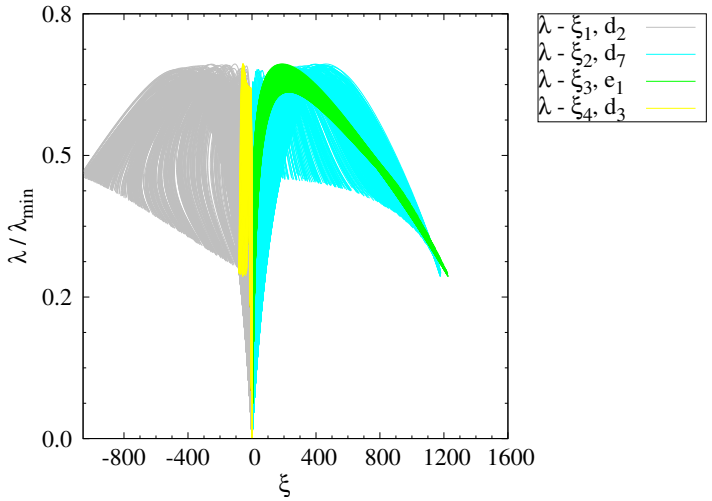

Figure 5.12: Equilibrium paths λ versus ξ_i $i = 1 \cdots 4$ for the length $L = 2000\ mm$. λ_{min} is the lowest critical load found.

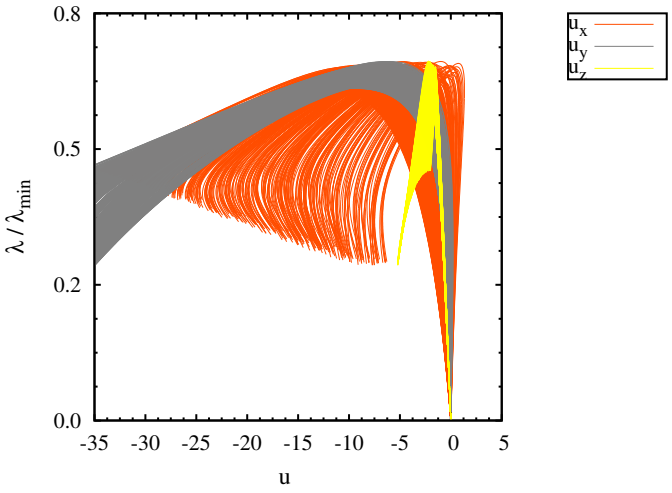

Figure 5.13: Equilibrium paths λ versus u. λ_{min} is the lowest critical load found. The displacement components u_x, u_y and u_z are measured in the point A. See Fig.5.3.

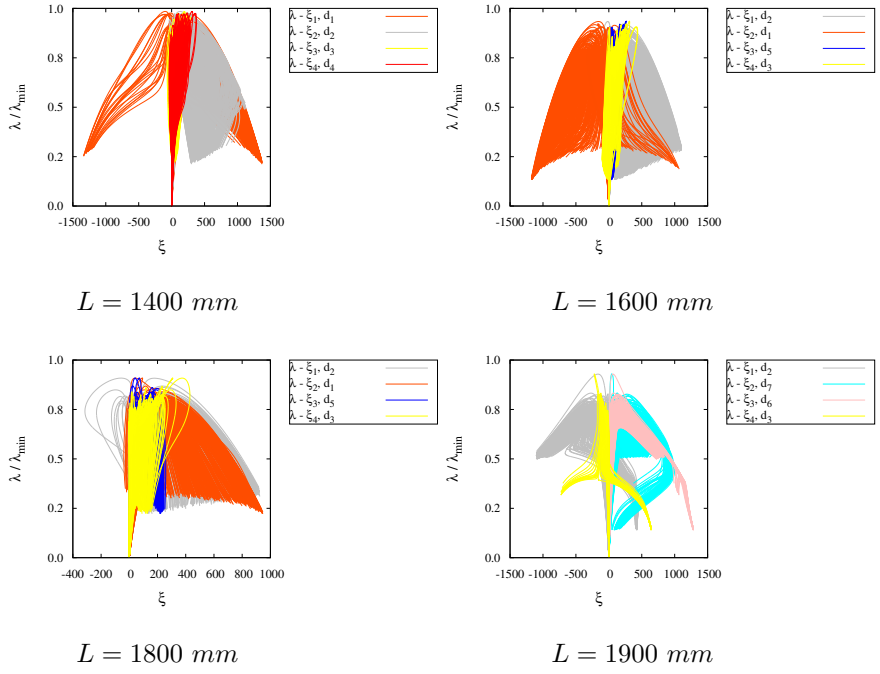

$L = 1400\ mm$ $L = 1600\ mm$

$L = 1800\ mm$ $L = 1900\ mm$

Figure 5.14: Equilibrium paths λ versus ξ_i $i = 1 \cdots 4$ for four lengths. λ_{min} is the lowest critical load found.

The probability density function, used to model the frequency for the limit load, is the Gumbel Max distribution:

$$f(\lambda_{lim}/\lambda_{min}|\mu,\sigma) = \left(\frac{1}{\sigma}\right) exp\left(-exp\left(-\frac{(\lambda_{lim}/\lambda_{min}-\mu)}{\sigma}\right) - \frac{(\lambda_{lim}/\lambda_{min}-\mu)}{\sigma}\right) \tag{5.4}$$

where μ is the location parameter and σ is the scale parameter.

The probability distribution functions for RSN 125 x 3.2, with the values of μ and σ, are showed in Fig. (5.17). The probability curves considering different numbers of imperfection are also shown for the specimen $L = 2000\ mm$ (Fig. (5.17)). As can be seen five hundred imperfection allow a good evaluation of the parameters of the probability function. The Monte Carlo simulation also allows the worst imperfection case to be found as shown in Fig. (5.16) for the length $L = 2000\ mm$ and in Table 5.3 where the participation in percentage (%) of buckling modes to worst imperfection is reported. The evaluation of the erosion is also given in [94]. In particular, for the studied cases the strongest erosion has been detected for the specimens $L = 2000\ mm$ and $L = 2200\ mm$ (see Fig. (5.18)), which is in agreement with the results obtained in papers [94, 95, 96]. It can be observed that based on the above parametric study, the obtained maximum nondimensional erosion is of 0.42 for the net section RS 125 x 3.2. In a direct comparison with the results obtained via the Erosion of Critical Bifurcation Load (ECBL) approach [27], it can be observed that the maximum erosion is a good agreement with the one obtained in [94], i.e. 0.44 for the RS 125 x 3.2 section, but for a combination of

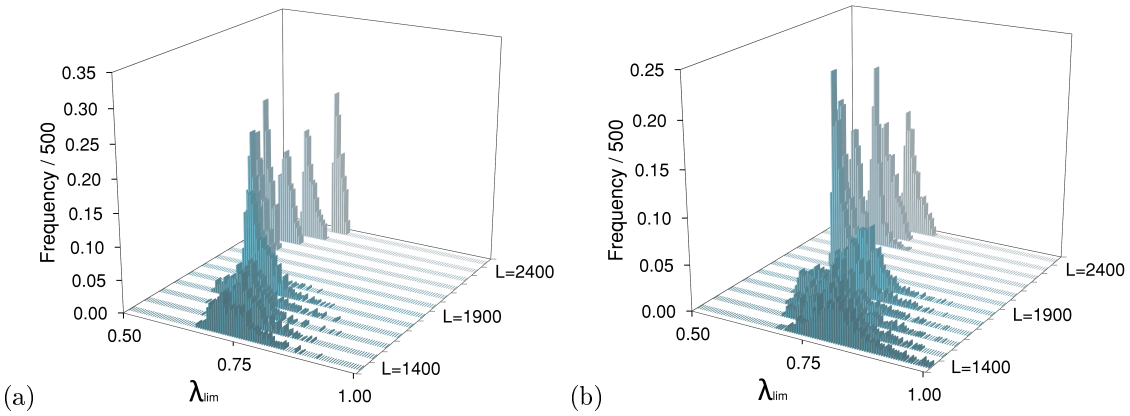

Figure 5.15: Frequency distribution of the limit load found λ_{lim} for the brut section (a) and net section (b).

imperfections ($\tilde{u}^g_{max} = L/750$ and $\tilde{u}^d_{max} = 1.5t$). The maximum erosion obtained in [96] via the ECBL approach, i.e. 0.395 for the RS 125 x 3.2 section, is also close to the one presented above but have been obtained for a combination of imperfections ($\tilde{u}^g_{max} = L/1000$ and $\tilde{u}^d_{max} = 1.0t$).

To show the sensitivity of the structure to the imperfection, once the worst imperfection $\tilde{u}_w$ is obtained a further sensitivity analysis has been performed assuming

$$\tilde{u} = \alpha\, \tilde{u}_w \tag{5.5}$$

with α being an amplification parameter. The results are shown in Fig. 5.19. The graphs show the specimens with maximum erosion, confirming the results shown in Fig. 5.9, and their sensitivity to the worst imperfection.

L (mm)	% Mode 1	% Mode 2	% Mode 3	% Mode 4
1400	82.49 (−)	7.68 (−)	7.33 (−)	2.50 (−)
1500	92.88 (−)	2.46 (−)	0.16 (−)	4.51 (−)
1600	56.05 (−)	33.92 (+)	0.49 (−)	9.55 (−)
1700	1.03 (−)	58.12 (+)	38.94 (+)	1.90 (−)
1800	50.93 (−)	43.32 (−)	0.03 (−)	5.72 (−)
1900	73.16 (−)	2.27 (−)	24.47 (−)	0.11 (+)
2000	70.69 (+)	4.46 (+)	22.42 (+)	2.43 (+)
2100	1.76 (+)	76.20 (−)	21.34 (−)	0.69 (+)
2200	76.67 (−)	0.59 (−)	21.37 (−)	1.37 (+)
2300	22.16 (−)	0.14 (+)	35.13 (−)	42.58 (−)
2400	21.96 (−)	0.40 (+)	74.61 (−)	3.02 (−)
2500	21.90 (−)	0.98 (+)	73.72 (−)	3.41 (−)

Table 5.3: Participation of buckling modes in worst imperfection in percentage (%) corresponding to the investigated length range for RSN 125 x 3.2 section. The buckling modes are normalized as reported in Eq. **??**. The sign in brackets indicates how the mode is accounted for with respect to the normalization.

Finally, note that the imperfection sensitivity analysis in the context of Koiter's approach allows us to perform a Monte Carlo simulation with very low computational cost. Table 5.4 shows

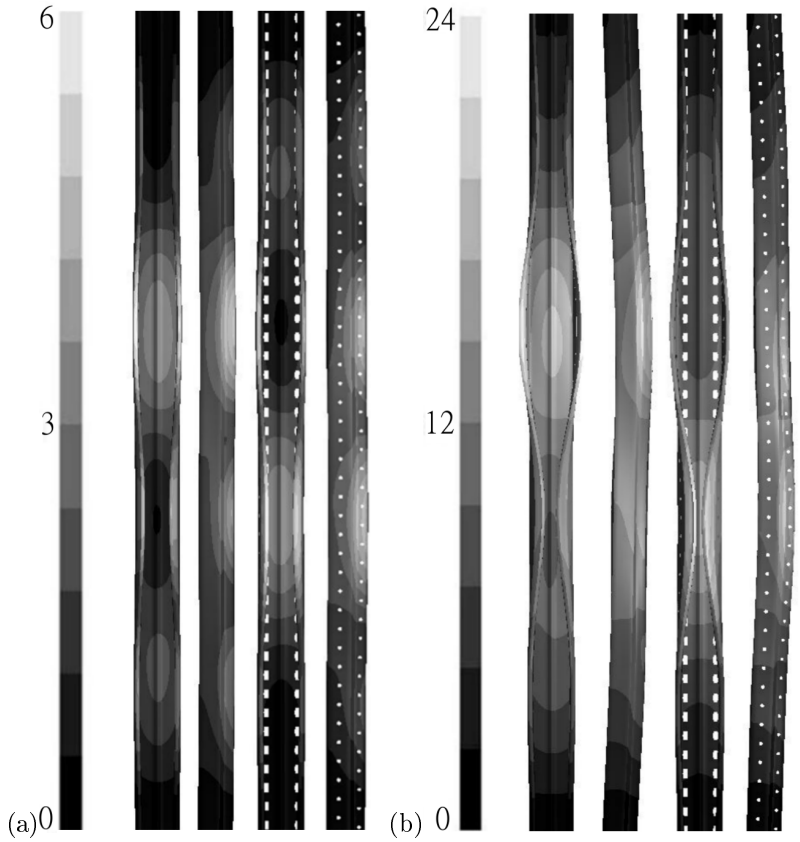

Figure 5.16: Section RS 125 x 3.2, brut and net, with length of 2200 *mm*: (a) initial shapes for worst imperfection amplified by factor 5.0, (b) deformed shapes at limit load for worst imperfection amplified factor 2.5.

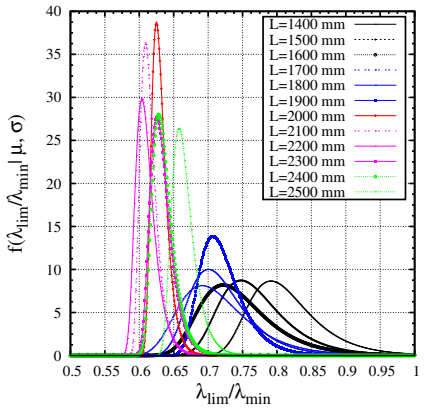

(a)

L (mm)	μ	σ
1400	0.7908	0.0425
1500	0.7478	0.0422
1600	0.7217	0.0449
1700	0.6905	0.0453
1800	0.7000	0.0368
1900	0.7070	0.0266
2000	0.6249	0.0095
2100	0.6089	0.0101
2200	0.6038	0.0123
2300	0.6258	0.0133
2400	0.6283	0.0131
2500	0.6575	0.0139

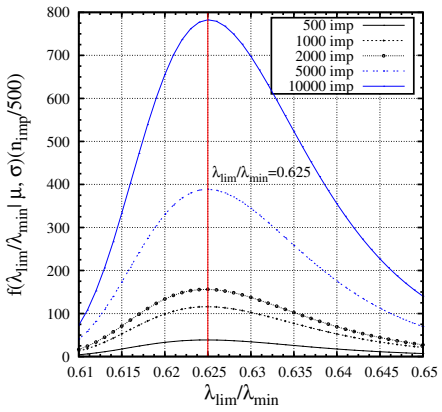

(b)

n imp.	μ	σ
500	0.6249	0.0095
1000	0.6251	0.0089
2000	0.6248	0.0094
5000	0.6249	0.0095
10000	0.6251	0.0094

Figure 5.17: (a) Probability distribution functions, for 500 geometric imperfections, corresponding to the investigated length range for RSN 125 x 3.2 section; (b) Probability distribution functions for $L = 2000$ mm for various numbers of imperfections. The values of the parameters of the probability distribution function (eq. (5.4)) are reported in the tables.

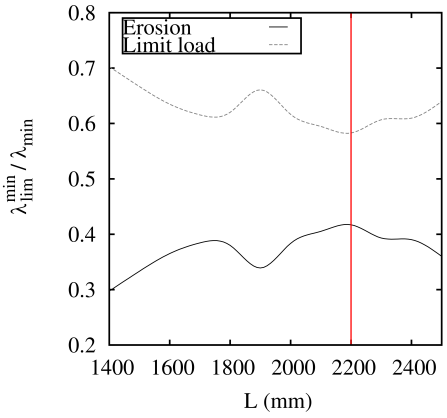

Figure 5.18: Section RSN 125 x 3.2 $L = 1400$ ... 2500 mm: the minimum limit load λ_{lim}^{min} is normalized on the first buckling load for each length. The specimen with maximum erosion is highlighted in red.

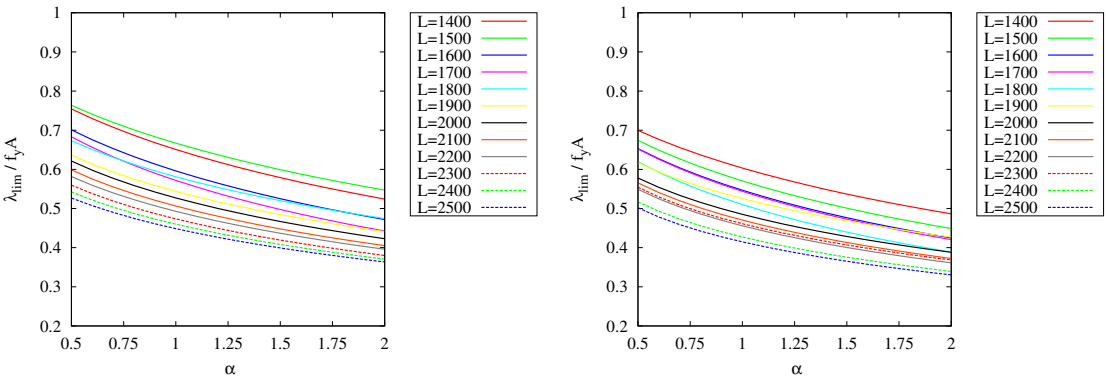

(a) Brut (b) Net

Figure 5.19: Section RS 125 x 3.2 $L = 1400 \ldots 2500$ mm: Sensitivity curve for the worst imperfection.

the time needed for the analysis. The computations are performed on an Intel(R) Xeon(R) CPU E5-2620 2.00Ghz Dual Core, 32 GB Ram on a single processor. Each value in Table 5.4 requires the solution of Eq. (1.7h) for as many random imperfections as indicated in the heading for that column.

The average times required for the steps i. to iv. have been studied [11], and remain of the order of seconds. This could allow users to run Monte Carlo simulations to account for other types of imperfections (i.e., load imperfection, residual stress) in order to obtain even more realistic evaluations of the worst structural performance.

		Time (s)				
L (mm)	N_v	500 imp.	1000 imp.	2000 imp.	5000 imp.	10000 imp.
1400	81011	7.040	16.143	30.681	76.307	151.766
1500	86555	7.580	16.976	31.165	85.254	166.156
1600	92099	8.259	17.738	32.432	91.276	168.527
1700	97643	7.513	17.984	29.624	75.458	167.950
1800	103187	6.548	13.322	26.192	91.681	144.472
1900	108731	9.070	18.805	36.020	91.728	191.864
2000	114275	9.100	18.518	36.334	102.258	213.065
2100	119819	8.650	18.330	49.168	87.095	177.278
2200	125363	10.400	22.620	46.832	120.245	216.871
2300	130907	9.324	19.594	35.880	96.923	180.056
2400	136451	9.045	19.251	49.823	89.310	177.996
2500	141995	9.364	20.358	37.628	110.245	203.174

Table 5.4: Section RS 125 x 3.2 $L = 1400 \ldots 2500$ mm: Computational costs. N_v denotes the numbers of variables.

5.1.4 A virtual laboratory for imperfection sensitivity analysis

Experimental study on pallet rack uprights in compression has been carried out at the Politehnica University of Timisoara. The experimental program was extensively presented in [94, 95]. The same cross-sections to the previous paragraphs are considered: the geometry of the cross-section is shown in Figure ((5.1)), while the details relating to the cross-section, perforations, material, experimental tests and numerical simulations can be found in [94, 95]. In the following, are

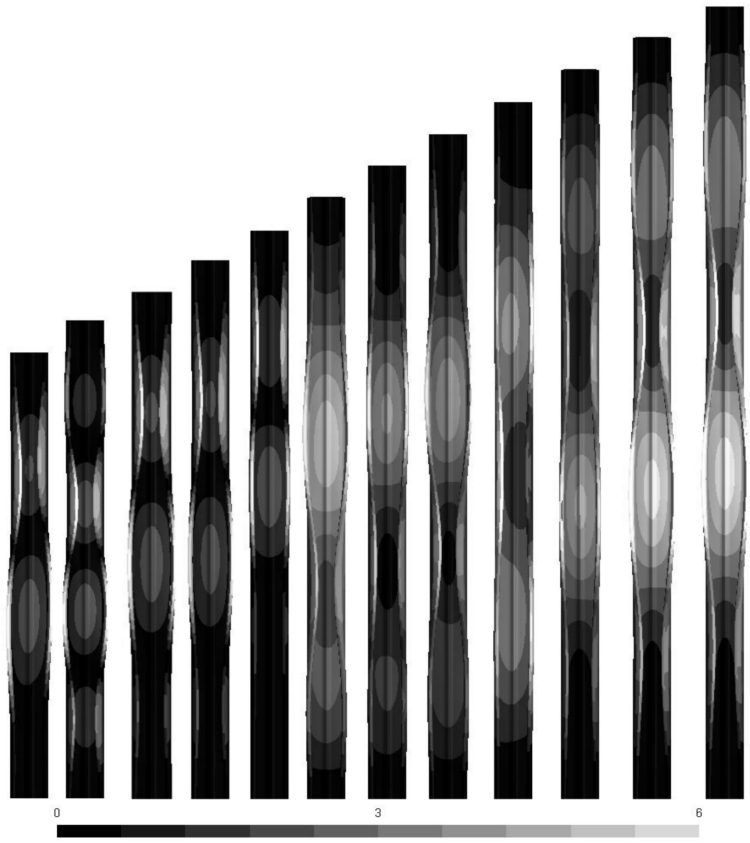

Figure 5.20: Section RSB 125 x 3.2 $L = 1400 \ldots 2500\ mm$: initial shapes for worst imperfection.

reported the results of an intensive imperfection sensitivity analysis for the pallet rack uprights in compression. For each section are considered five thicknesses: 1.0, 1.4, 2.0, 2.6 and 3.2 mm. A total of 120 beams are analyzed. In the Figures (5.20) and (5.21) are shown the initial shapes for worst imperfection for the brut and net cross sections with $t = 3.2\ mm$, respectively. The deformed shapes at limit load, for the brut and net cross sections with $t = 3.2\ mm$, obtained using the initial shapes for worst imperfection (Figures (5.20) and (5.21)) are shown in Figures (5.22) and (5.23).

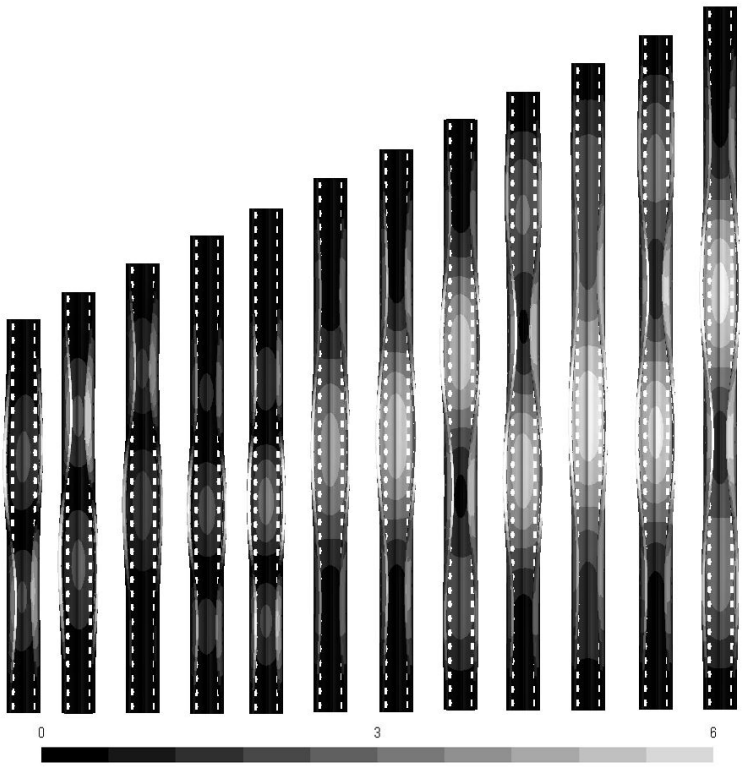

Figure 5.21: Section RSN 125 x 3.2 $L = 1400 \ldots 2500$ mm: initial shapes for worst imperfection.

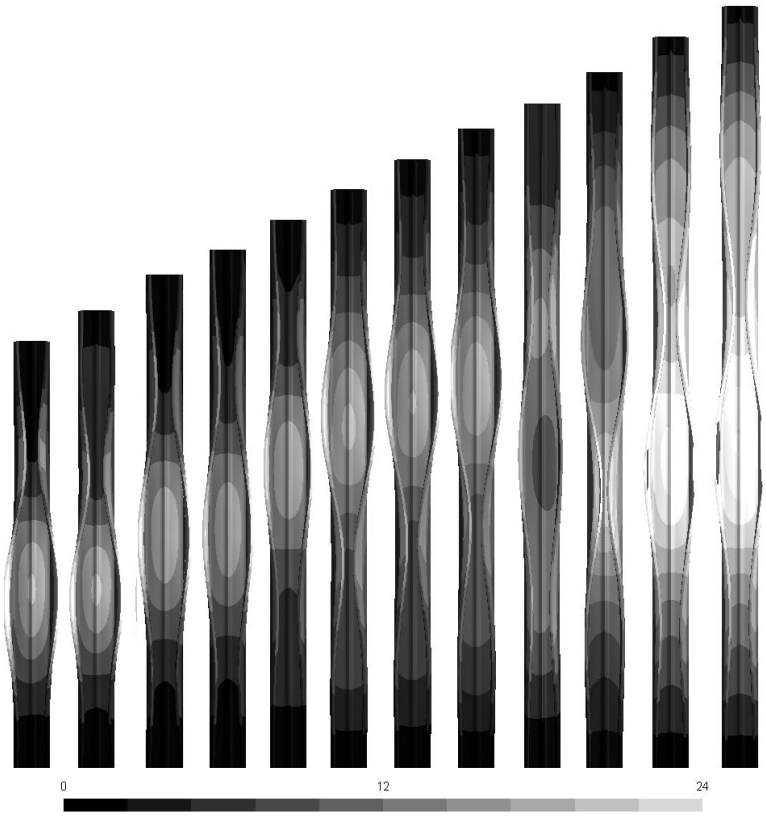

Figure 5.22: Section RSB 125 x 3.2 $L = 1400 \ldots 2500$ mm: deformed shapes at limit load for worst imperfection.

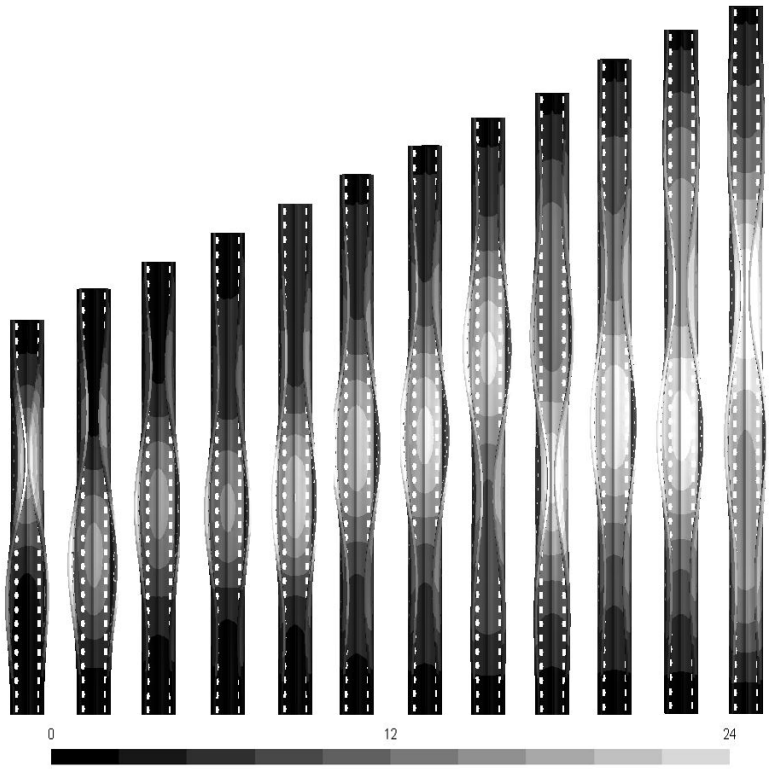

Figure 5.23: Section RSN 125 x 3.2 $L = 1400$ ... 2500 mm: deformed shapes at limit load for worst imperfection.

5.1.5 Remarks on Koiter's asymptotic analysis

The accuracy of the method in the recovery of the equilibrium path of steel perforated sections is also shown in Fig. 5.30. The comparison of Koiter's analysis versus a Riks path following analysis shows, also in this case, the accuracy of the method in the recovery of the pre-critical, critical and initial post-critical behaviours.

A crucial point in Koiter's analysis is the selection of the number of buckling modes to be included. No a-priori theoretical information is generally available that allows it to be stated if a certain number of modes is enough. However, an a-posteriori study varying the numbers of modes can be performed. The differences in the recovery of the equilibrium path with an assigned imperfection for the length $L = 2000$ mm have been reported in Fig. 5.28. The number of modes varies from 2 to 7. The equilibrium paths show different behaviour, above all in the post-critical range. However the limit point is well detected starting from the 4 modes considered. This statement is also supported by Table 5.5 where the minimum limit load λ_{lim}^{min} and the maximum limit load λ_{lim}^{max} have been reported for the length $L = 2000$ mm varying the number of modes and considering 500 imperfections. Starting from 4 the range between the maximum and minimum limit load is well-represented. So we can reasonably conclude that using 4-modes the non linear behaviour is correctly accounted for, at least for the statistical

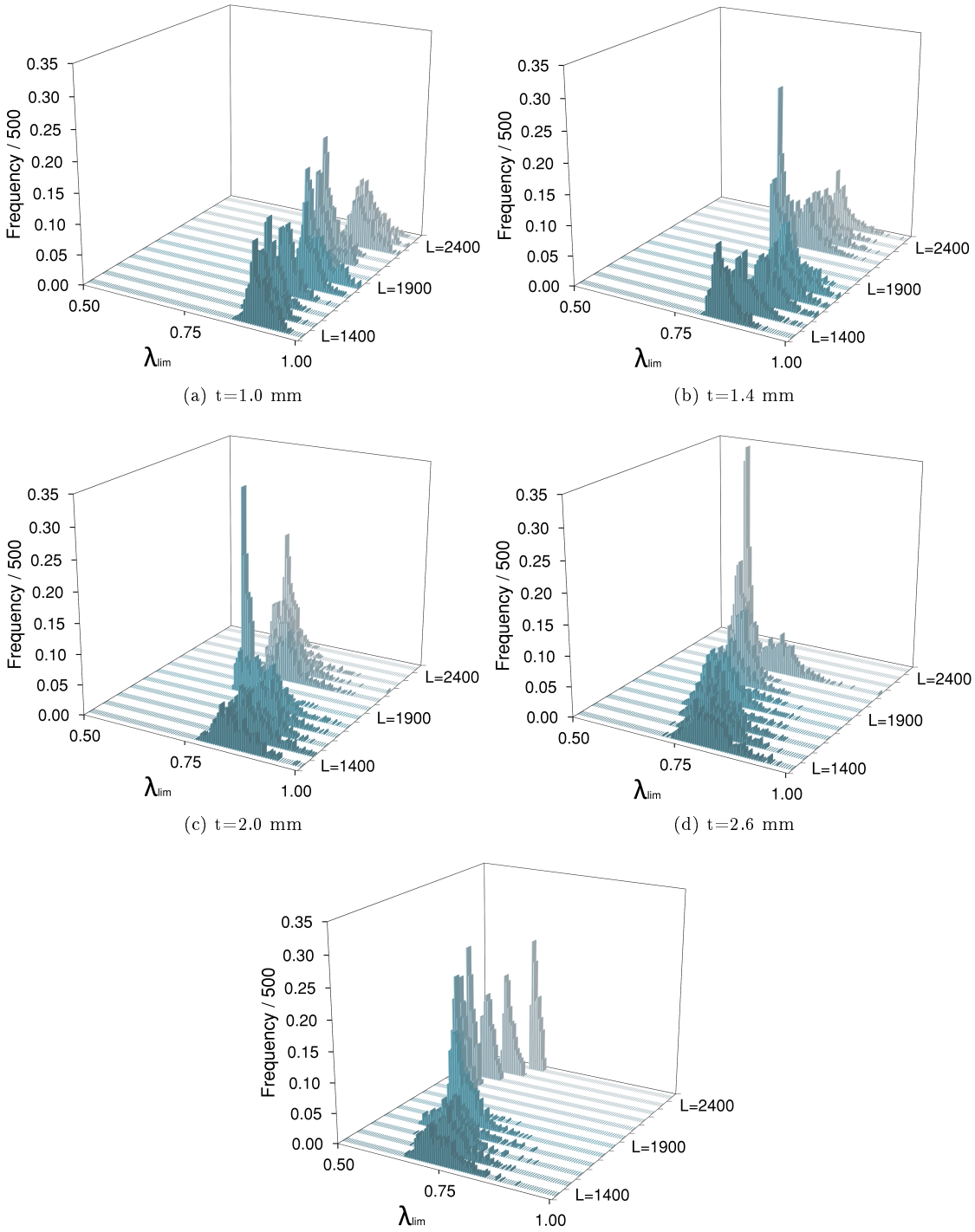

(a) t=1.0 mm

(b) t=1.4 mm

(c) t=2.0 mm

(d) t=2.6 mm

(e) t=3.2 mm

Figure 5.24: Section RSB 125: Frequency distribution of the limit load found λ_{lim}.

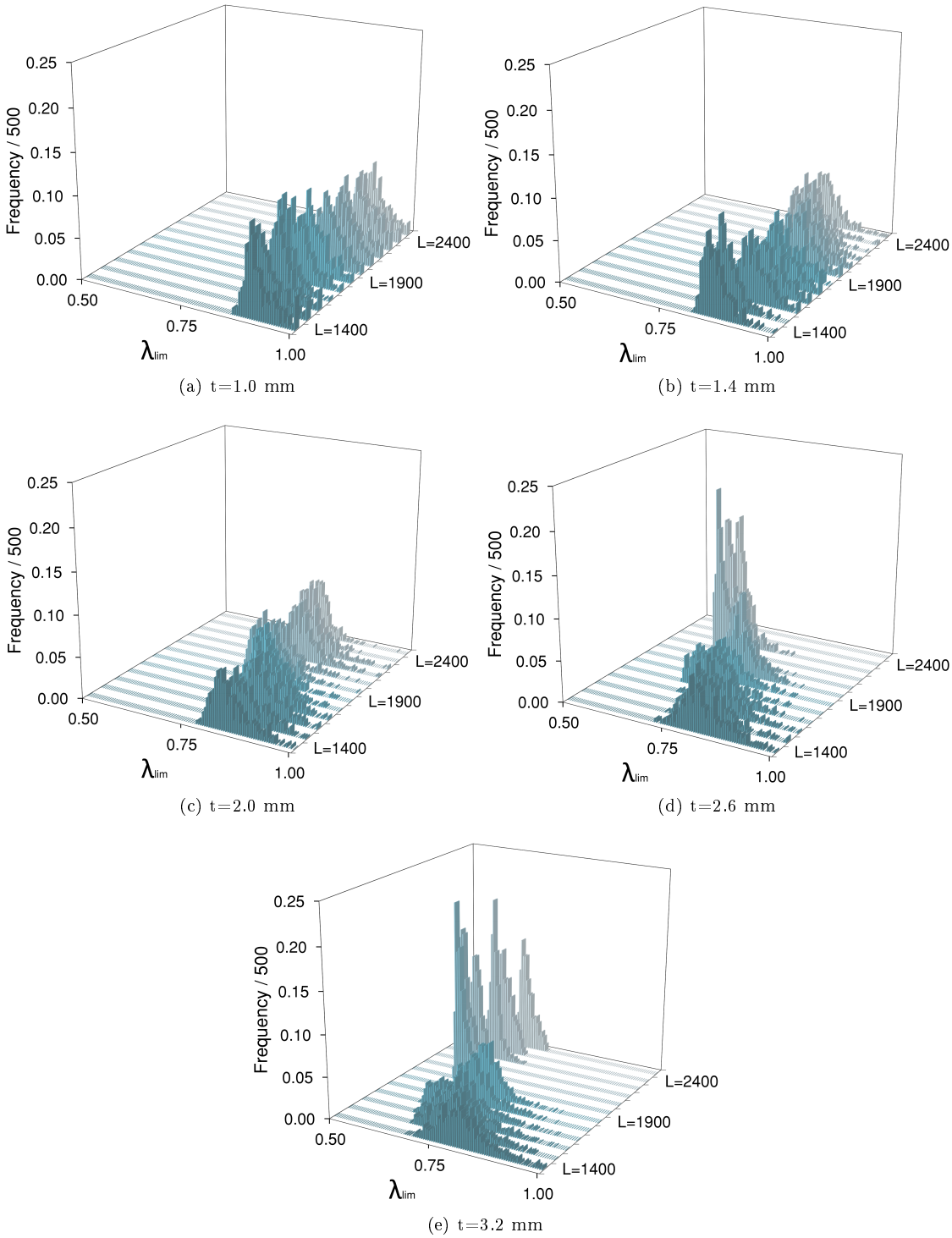

(a) t=1.0 mm

(b) t=1.4 mm

(c) t=2.0 mm

(d) t=2.6 mm

(e) t=3.2 mm

Figure 5.25: Section RSN 125: Frequency distribution of the limit load found λ_{lim}.

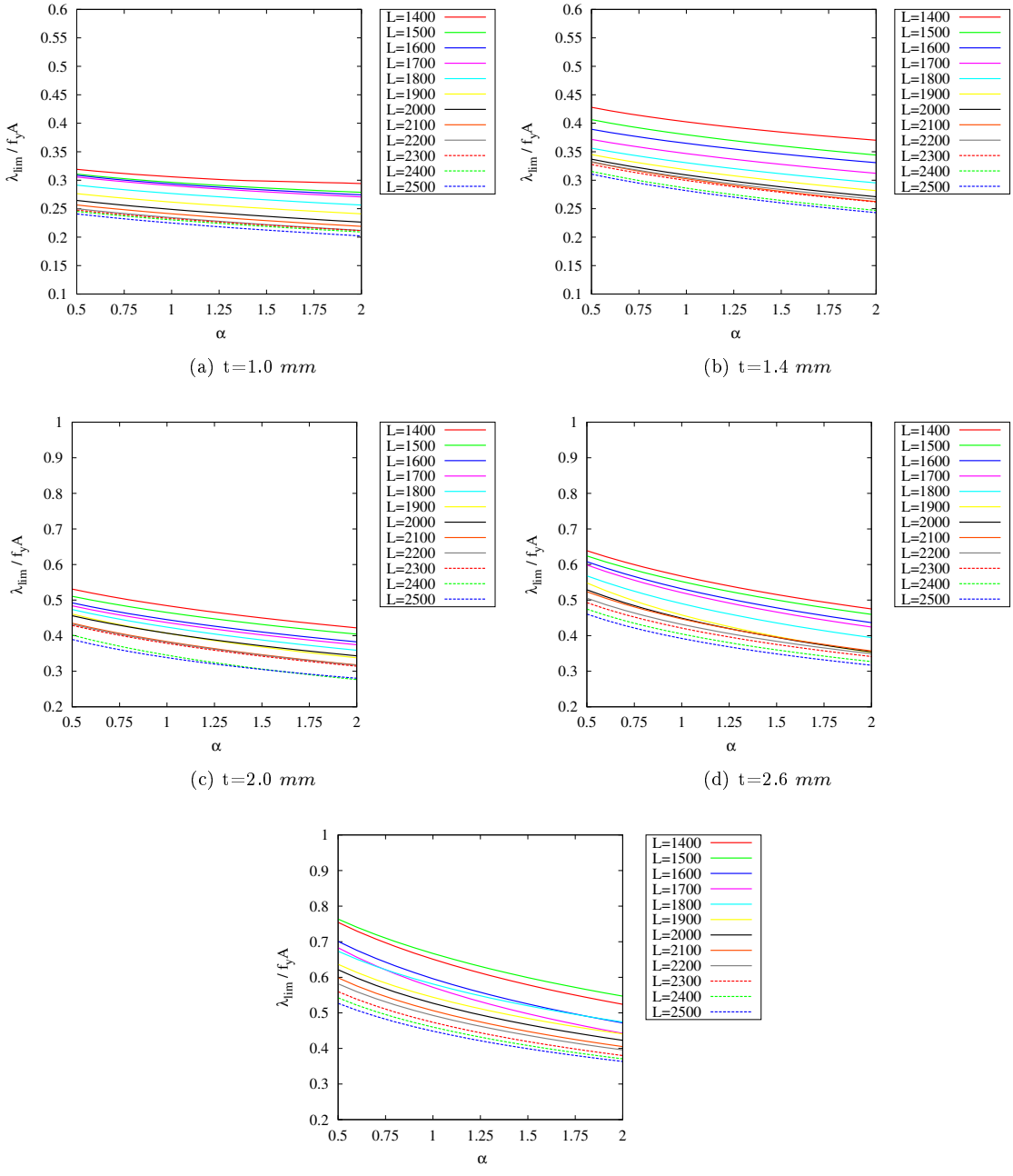

(a) t=1.0 mm

(b) t=1.4 mm

(c) t=2.0 mm

(d) t=2.6 mm

(e) t=3.2 mm

Figure 5.26: Section RSB 125 $L = 1400 \ldots 2500\,mm$: Sensitivity curve for the worst imperfection.

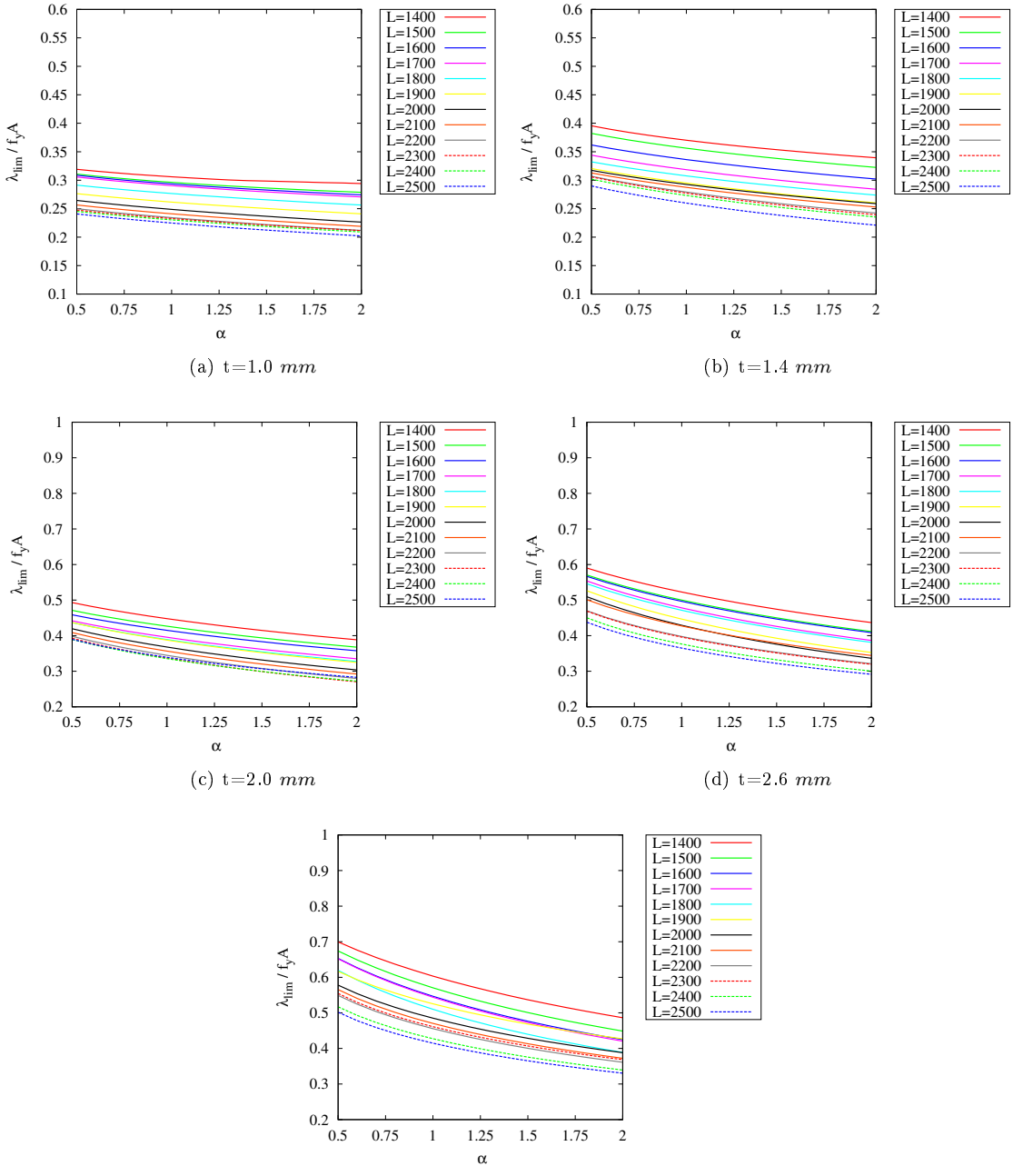

(a) t=1.0 mm

(b) t=1.4 mm

(c) t=2.0 mm

(d) t=2.6 mm

(e) t=3.2 mm

Figure 5.27: Section RSN 125 $L = 1400 \ldots 2500\,mm$: Sensitivity curve for the worst imperfection.

evaluation of limit load.

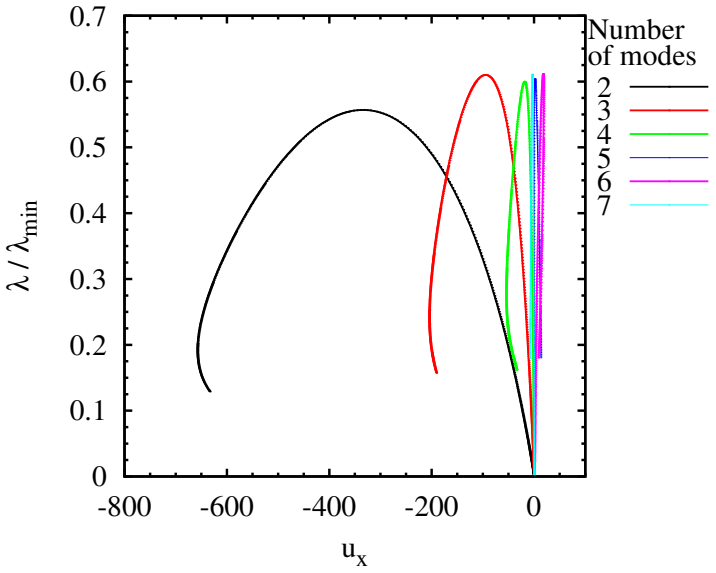

Figure 5.28: Section RS 125 x 3.2, length $L = 2000\ mm$: equilibrium paths λ/λ_{min} versus the displacements u_x for different numbers of buckling modes considered for Koiter's analysis. For each analysis, the worst imperfection in the buckling modes space has been used.

n modes	λ_{lim}^{min}	λ_{lim}^{max}
2	0.5570	0.5659
3	0.6113	0.6628
4	0.6117	0.8645
5	0.6040	0.8364
6	0.6095	0.8378
7	0.6109	0.8598

Table 5.5: Section RS 125 x 3.2, length $L = 2000\ mm$: λ_{lim}^{min} and λ_{lim}^{max} for varying numbers of buckling modes accounted for in Koiter's analysis.

The study of structures sensitive to imperfections requires testing several imperfections to find the worst cases and then the minimum limit load. The use of GMNIA analysis is often prohibitive in terms of computational cost and time [97]. On the other hand, Koiter's method allows the effects of thousands of imperfections to be tested with very low computational cost, even if it requires the validity of the elastic behaviour. In the case of the critical and initial post-critical behaviour these are characterized by a predominantly elastic behaviour, that is more recurrent for slender structures. The Koiter method can be used to select the worst cases that can then be analysed in a single GMNIA to take into account the geometrical and material nonlinear effects.

For completeness the study of length $L = 2000\ mm$ for the worst imperfection using GMNIA will be presented. The details used for the elasto-plastic analysis can be found in [94, 95]. In

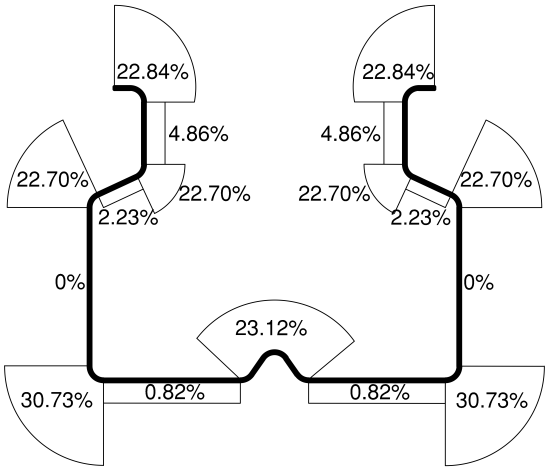

Figure 5.29: Section RS 125 x 3.2, length $L = 2000\ mm$: Yield stress increase due to cold forming ($\%f_y$).

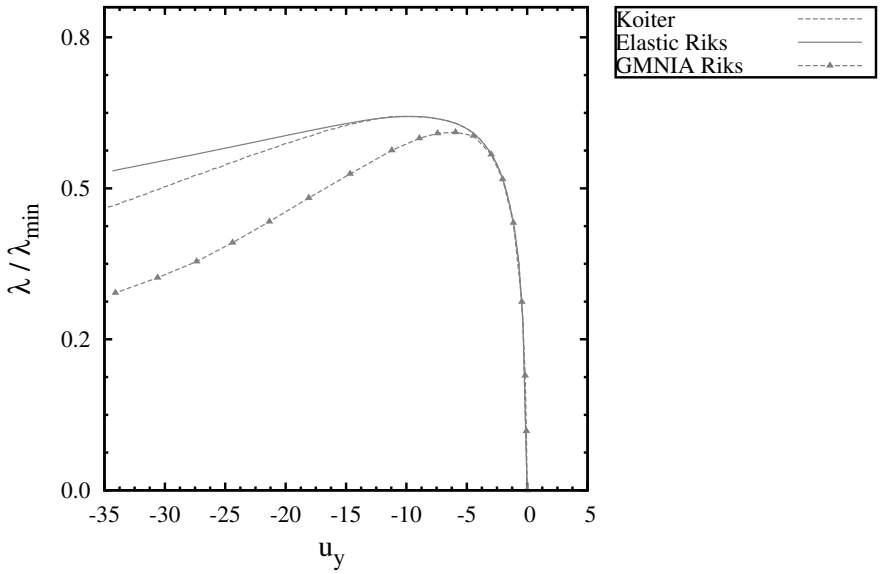

Figure 5.30: Section RS 125 x 3.2, length $L = 2000\ mm$: equilibrium paths λ/λ_{min} versus the displacements u_y using Koiter's and Riks elastic analysis and GMNIA. For each analysis the worst imperfection (see Table5.3) has been used.

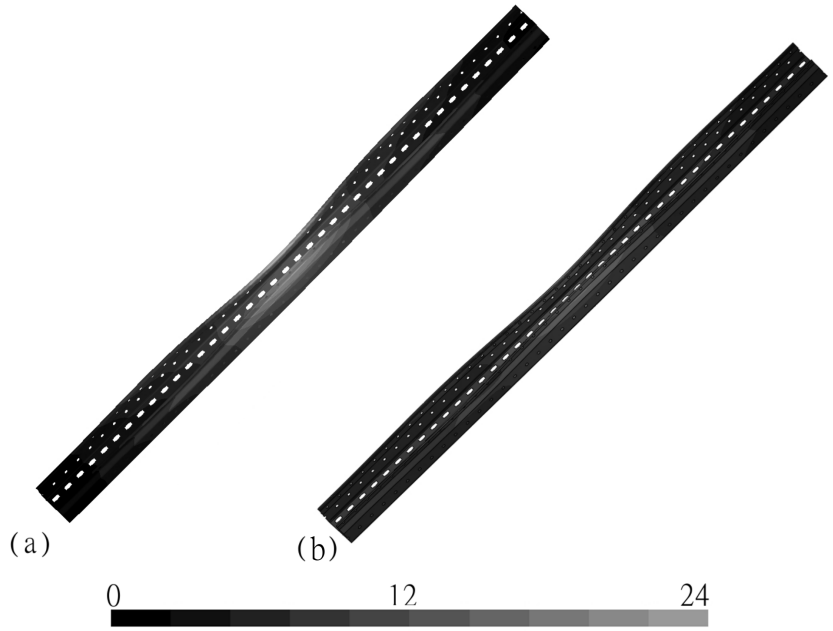

Figure 5.31: Section RS 125 x 3.2 $L = 2000$ mm: (a) deformed shape at limit load for worst imperfection obtained by Koiter approach; (b) deformed shape at limit load for worst imperfection obtained by Riks analysis.

particular the yield stress used is $f_y = 465.18$ N/mm^2 while the increments of yield stress due to cold forming are reported in Fig. 5.29. The equilibrium paths recovered with Koiter analysis and GMNIA analysis have been reported in Fig. 5.30. As clear shown the plasticity starts in the critical/ initial post-critical range producing an additional erosion in limit load. The deformed shapes at the limit load are reported in Fig. 5.31 for Koiter and GMNIA analysis, confirming that plasticity does not change the critical/initial post-critical behaviour in terms of deformation but only in terms of limit load reduction.

5.2 A laminated composite hinged box in compression

In the following, the box shown in Figure 5.32 is analyzed. The geometrical data are $L = 1000$ mm, $a = 500$ mm. Three witdh/thickness ratios are considered: $a/t = 1/500, 1/400, 3/1000$. The ply properties are $E_1 = 123.55$ GPa; $E_2 = 8.708$ GPa; $G = 5.695$ GPa; $\nu_{12} = 0.32$. The laminate stacking sequence is $[0/0/19/-19/37/-37/45/-45/51/-51]$. The bottom end of the box is hinged. The load is a uniform edge pressure applied at the top end of the box.

5.2.1 Buckling analysis

Once the fundamental path is evaluated (eq. 1.7a), a buckling analysis (eq. 1.7c) is performed. The first eight buckling loads are reported in Table 5.6 for different values of width/thickness ratio. The buckling modes for $t/a = 1/400$ are shown in Figure 5.33. The buckling modes are

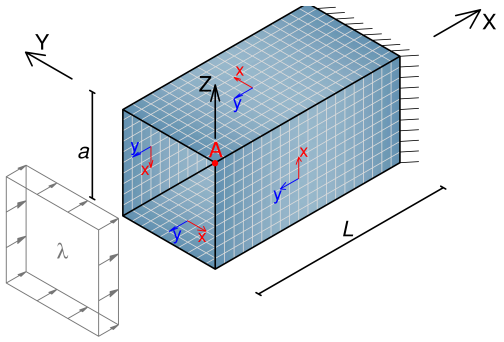

Figure 5.32: Geometry, boundary conditions, and load for the box in compression.

then used to generate random geometrical imperfections.

t/a	λ_1	λ_2	λ_3	λ_4	λ_5	λ_6	λ_7	λ_8
1/500	608.28	760.38	760.38	920.14	1005.10	1102.10	1281.22	1281.22
1/400	1187.16	1484.52	1484.52	1796.78	1961.72	2151.00	2501.40	2501.40
3/1000	2049.80	2564.00	2564.00	3104.00	3387.40	3714.20	4319.40	4319.40

Table 5.6: Buckling loads (in Newtons) for the box in compression at several t/a ratios.

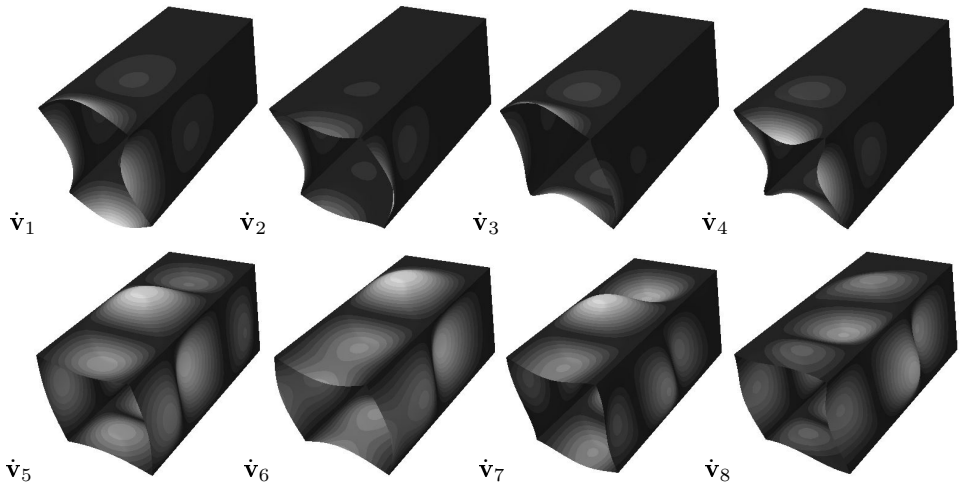

Figure 5.33: Buckling modes for the box in compression at $t/a = 1/400$.

5.2.2 Post-buckling and imperfection sensitivity analysis

Some of the quadratic corrections (eq.1.7d) are shown in Figure (5.34) and used to recover the structural behaviour of the imperfect structure. Only geometrical imperfections $\tilde{u}$ have been considered. In particular, they are generated as linear combinations of the buckling modes $\dot{v}_i$, that is

$$\tilde{u} = \sum_{i}^{m} r_i \dot{v}_i \tag{5.6}$$

where r_i are random numbers, and m is the number buckling modes included in the expansion (1.7e). For this example, $m = 8$ is used. Note that our aim is to find the worst imperfection.

Then, the real shape of the imperfection is not required and only the linear combinations of buckling modes are considered. The maximum value of $\tilde{u}_{max}$ is assumed to be bound by a tolerance

$$\tilde{u}_{max}/t \leq tol \tag{5.7}$$

For this example, $\tilde{u}_{max}/t = 1.5$ is used, while in practice the amplitude of the imperfection depends on the manufacturing process. Obviously, the amplitude of the imperfection affects the results in term of limit loads, as shown in the following.

The equilibrium paths for 500 random geometrical imperfections have been graphed in Figure (5.35) in terms of mode amplitude $\xi_i, i = 1..8$, and in Figure (5.36) in terms of nodal displacements. Loss of stability in the post-critical range and the presence of attractive paths [99, 100] can be seen in the figures. Even if the random imperfections generate different behaviour within a range, the imperfect paths manifest a convergent behaviour to some particular paths (i.e. attractive paths). This is also clear in Figure 5.37, where the interaction between the first mode and the remaining seven modes are shown, as well as in Figure 5.38 in terms of deformed configurations. A-priori knowledge of attractive paths could be used to increase the efficiency of the Monte Carlo simulation, by reducing the space of trial imperfections.

Monte Carlo simulation allows us to evaluate the frequency of occurrence of limit load (Figure 5.39), the worst imperfection (Figure 5.40), and the shape of the structure at the minimum limit load (Figure 5.41).

Finally, to show the sensitivity of the structure to the worst imperfection magnitude $\tilde{u}_w$, further sensitivity analysis has been performed varying $\tilde{u}_{max}/t$. The results are shown in Figure 5.42, showing that this composite box is very sensitive to imperfections.

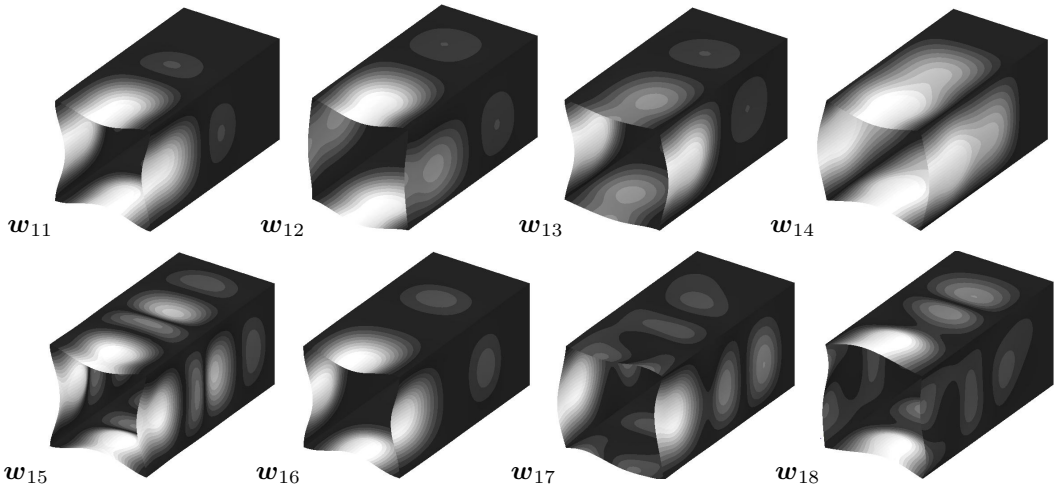

Figure 5.34: Quadratic corrections for the box in compression, with $t/a = 1/400$.

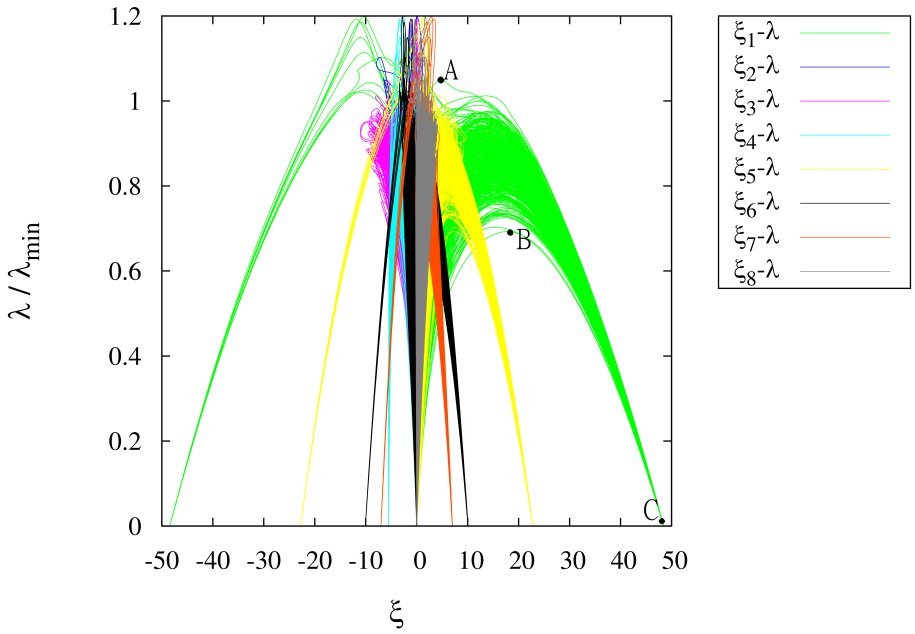

Figure 5.35: Equilibrium paths λ versus ξ_i, $i = 1...8$ for the box in compression, with $t/a = 1/400$.

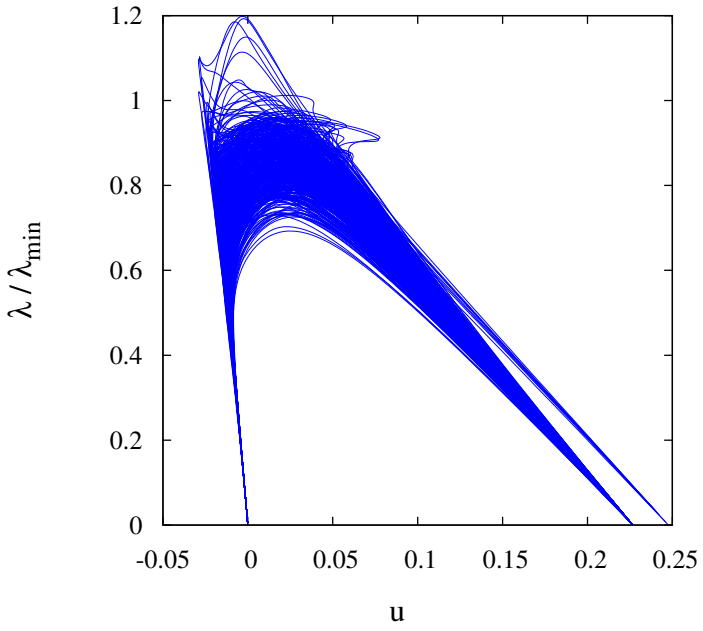

Figure 5.36: Equilibrium paths λ versus u for the box in compression, with $t/a = 1/400$. The displacement component u_x is measured at point A in Fig.(5.32).

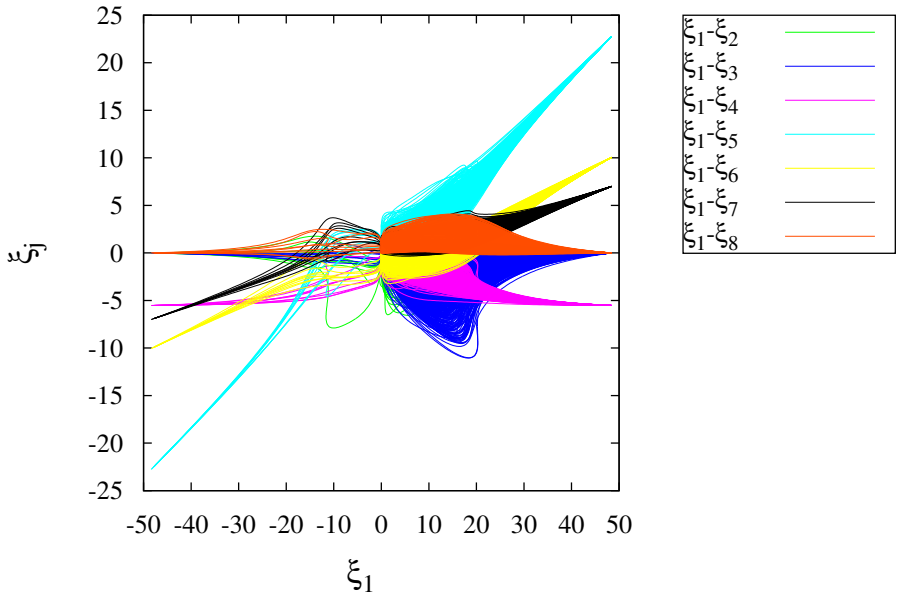

Figure 5.37: Interaction between the first mode (with amplitude ξ_1) and the remaining modes $\xi_j, j = 2..8$. The presence of attractive paths is clear.

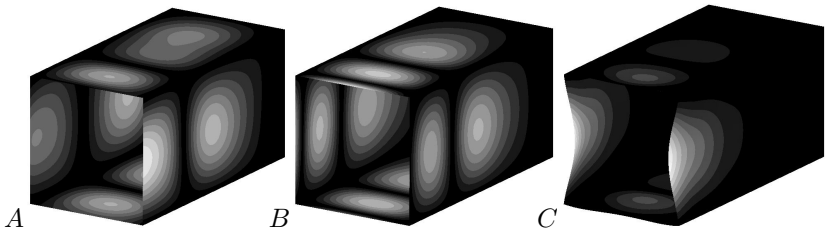

Figure 5.38: Deformed configuration at points A, B and C, labeled in Figure (5.35).

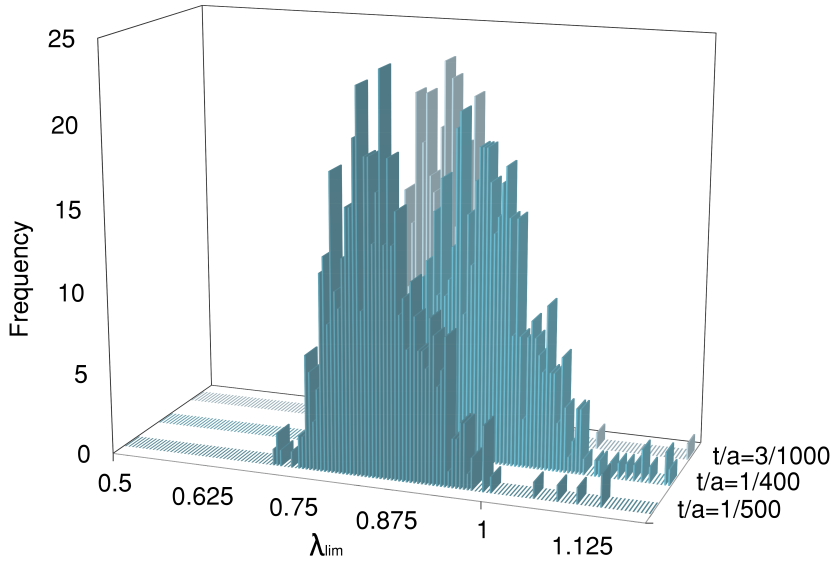

Figure 5.39: Frequency distribution of the lowest limit load found λ_{lim} for the clamped box in compression and several values of t/a.

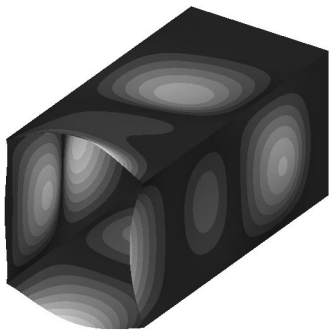

Figure 5.40: Shape of the worst imperfection for the box in compression, with $t/a = 1/400$.

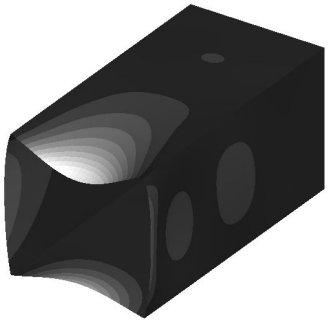

Figure 5.41: Mode shape at minimum limit load with the worst imperfection for the box in compression, with $t/a = 1/400$.

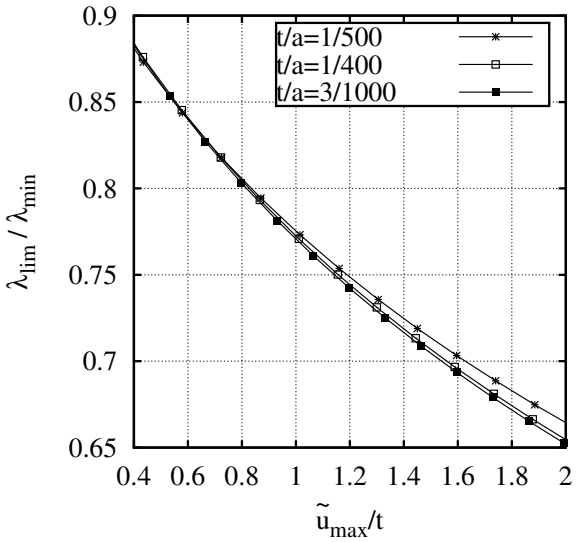

Figure 5.42: Load sensitivity to worst imperfection amplitude $\tilde{u}_{max}/t$ for the box in compression at several values of t/a.

5.3 A laminated composite box beam in compression

To illustrate some of the capabilities of the proposed element, the box beam shown in Figure 5.43 is analyzed [46]. The side flanges and webs have a width $a = 2.5$ mm and the top flange is $2a$. Three thickness are considered $t/a = 1/5, 3/10, 1/2$. The ply properties are $E_1 = 104$ GPa; $E_2 = 10.3$ GPa; $G = 5.15$ GPa; $\nu_{12} = 0.21$. The laminate stacking sequence is [0/90/0/90]. The box beam is loaded and simply supported at both ends while the side flanges are free. The load is a uniform edge pressure applied at the column ends on the skin only (fore more details see [47]).

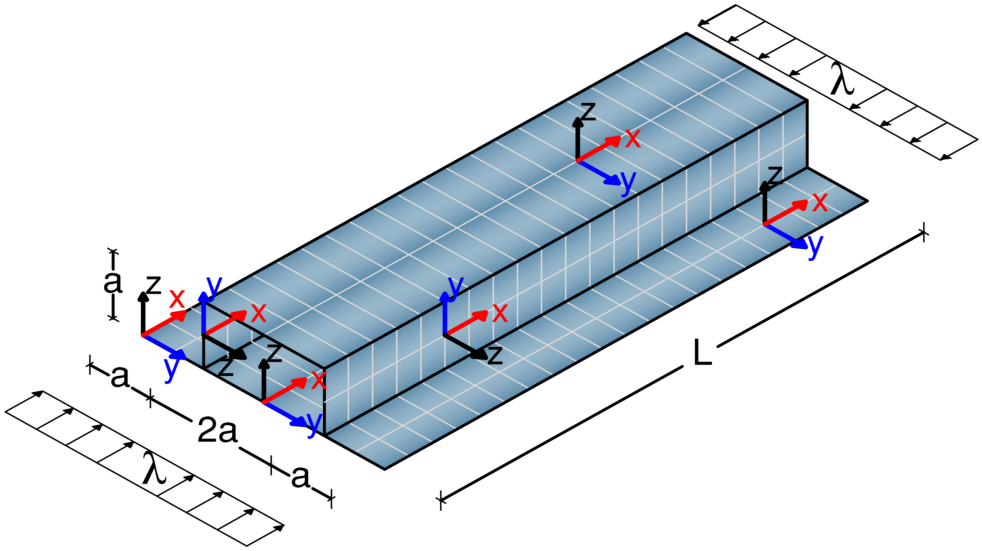

Figure 5.43: Box beam loaded axially. Geometry, boundary, and load conditions.

5.3.1 Buckling analyses

Once the fundamental path is evaluated (eq. 1.7a), a buckling analysis (eq. 1.7c) is performed. The first four buckling loads are shown in Table 5.7 for different length and thickness. The buckling modes for $L = 20\,mm, t/a = 3/10$ are reported in Figure 5.44. The buckling modes are then used to generate random geometrical imperfections.

	λ_1	λ_2	λ_3	λ_4	λ_1	λ_2	λ_3	λ_4	λ_1	λ_2	λ_3	λ_4
L	$t/a = 1/5$				$t/a = 3/10$				$t/a = 1/2$			
20	4879	5290	5322	5565	9811	10758	13031	1389	18282	25402	30795	32161
40	2976	4856	5339	5660	4558	10050	10627	1212	8052	18704	24702	26058
60	1589	4354	4985	5341	2420	6730	10115	9631	4230	12069	17657	16689
80	963	3021	4157	4450	1463	4628	6386	6751	2548	8181	11533	10835
100	639	2169	3085	2912	971	3310	4671	4427	1687	5809	7944	7489
120	453	1613	2240	2128	688	2458	3386	3229	1195	4297	5748	5454
140	337	1239	1692	1617	512	1885	2555	2449	888	3288	4331	4136
160	260	977	1318	1267	395	1486	1992	1917	686	2588	3373	3238
180	207	789	1055	1018	314	1199	1593	1541	545	2086	2696	2601
200	168	649	862	835	255	986	1302	1263	443	1714	2202	2134

Table 5.7: Buckling loads (in Newtons) for the box beam loaded axially. The used mesh for the analysis is reported in Fig. 5.43.

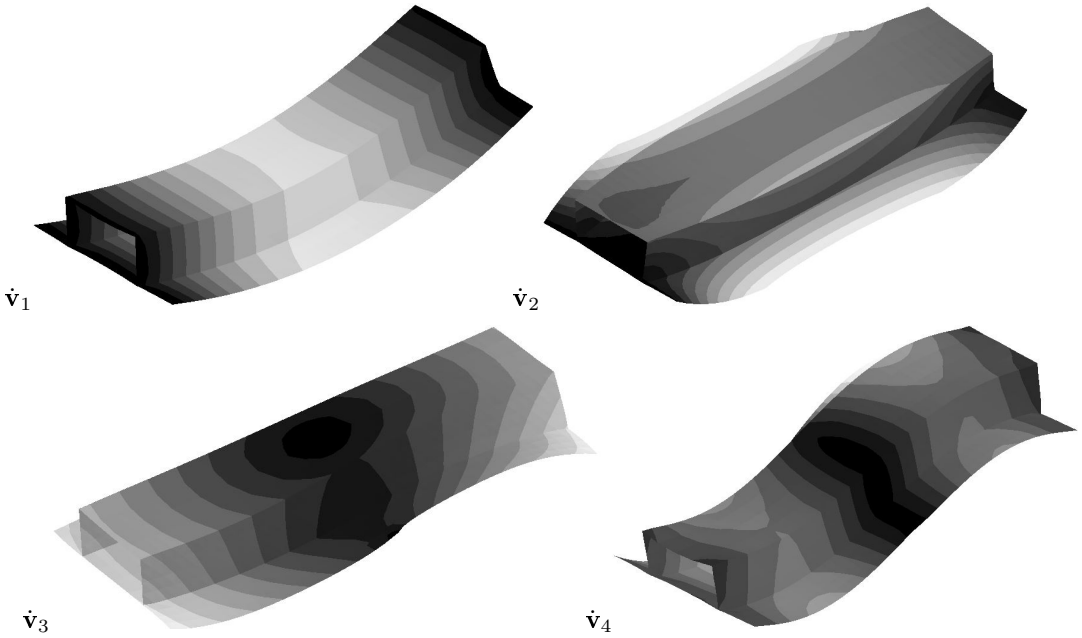

Figure 5.44: Buckling modes for the box beam with L=20 mm, t/a=3/10.

5.3.2 Post-buckling and imperfection sensitivity analyses

For this example, $u_{tol} = 1.5\,t$ is used (see Eq.(5.6) and (5.7)), while in practice the amplitude of the imperfection depends on the manufacturing process. The equilibrium paths for 500 random geometrical imperfections have been graphed in Figure (5.46) in terms of mode amplitude, and in Figure (5.47) in terms of nodal displacements. Monte Carlo simulation allows us to evaluate the frequency of occurrence of limit load (Figure 5.48), the worst imperfection (Figure 5.49), and the shape of the structure at the minimum limit load (Figure 5.50).

Finally, to show the sensitivity of the structure to the imperfection, once obtained the worst imperfection $\tilde{u}_w$ a further sensitivity analysis has been performed assuming

$$\tilde{u} = \alpha\,\tilde{u}_w \tag{5.8}$$

being α an amplification parameter. The results are shown in Figure 5.51. For this case the sensitivity to imperfection is not so high. Really, amplifying α from 1 to 2 the minimum limit load has a variation at most 10%.

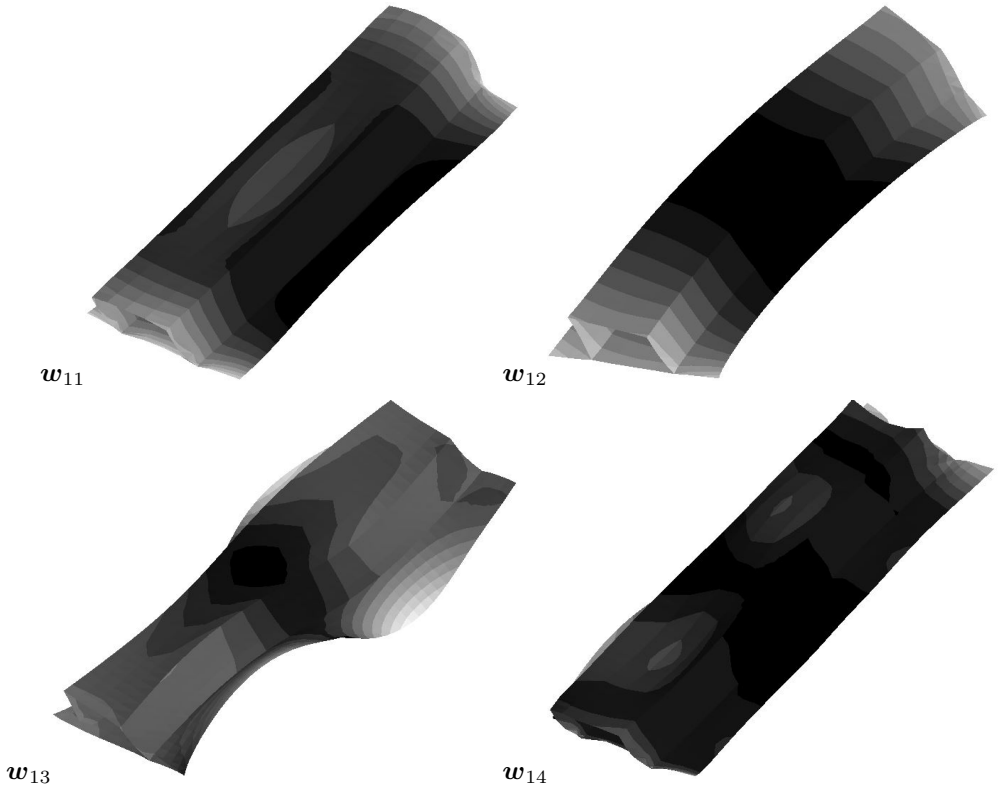

Figure 5.45: Quadratic corrections for the box beam with L=20 mm, t/a=3/10.

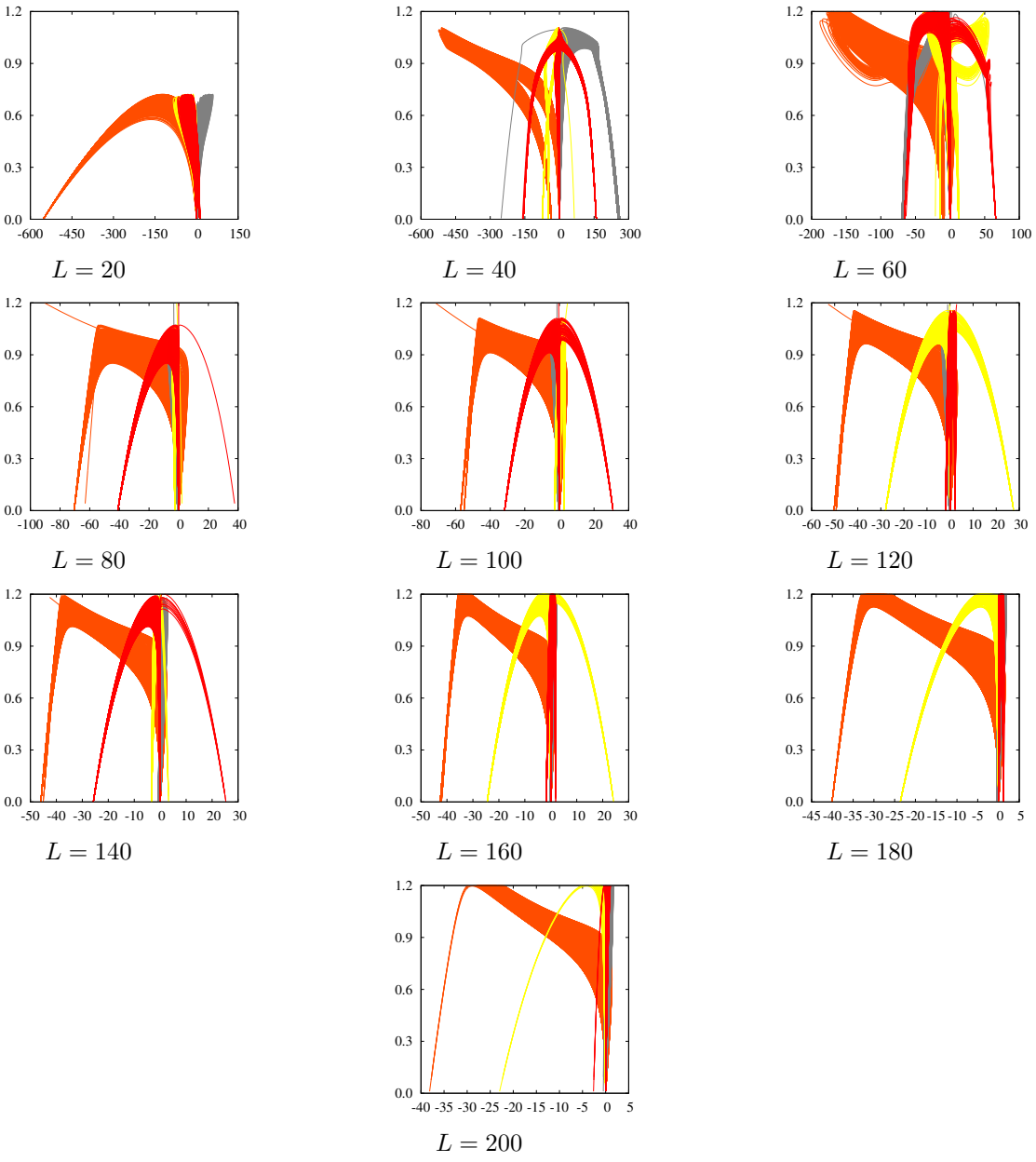

Figure 5.46: Equilibrium paths λ versus ξ_i (see (1.7e)) for the box beam loaded axially with uniform edge-pressure and simply supported at both ends on skin only, L = 20, 40...200 mm, t/a=3/10. Ordinate: λ/λ_{min}. Abscissa: mode amplitudes ξ_i, with i = 1...4 denoted by colors orange, grey, yellow, and red, respectively. λ_{min} is the lowest critical load found.

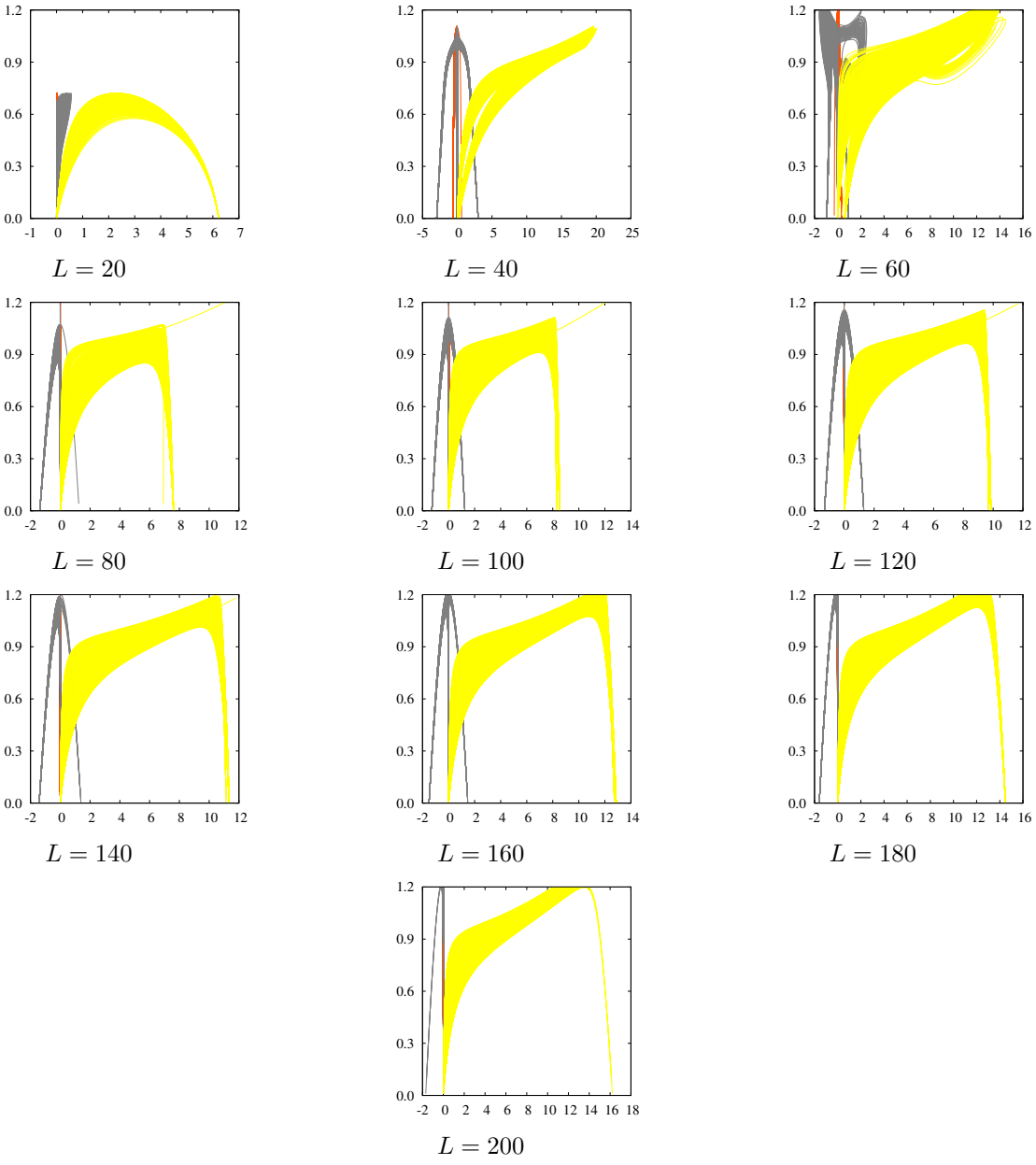

Figure 5.47: Equilibrium paths λ versus edge displacement u for the box beam loaded axially with uniform edge-pressure and simply supported at both ends on skin only, t/a=3/10. Ordinate: λ/λ_{min}. Abscissa: edge displacement u, for three cases denoted by colors orange, grey, and yellow, corresponding to column length $L = 20, 40, 200$ mm, respectively. λ_{min} is the lowest critical load found.

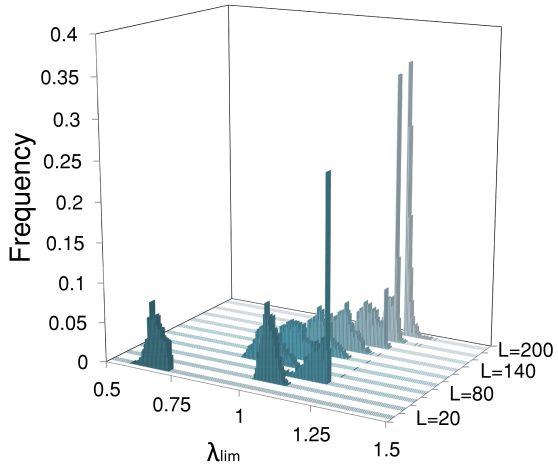

Figure 5.48: Frequency distribution of the lowest limit load found λ_{lim} for the box beam loaded axially with uniform edge-pressure and simply supported at both ends on skin only, $L = 20, 40, ...200$ mm; t/a=3/10.

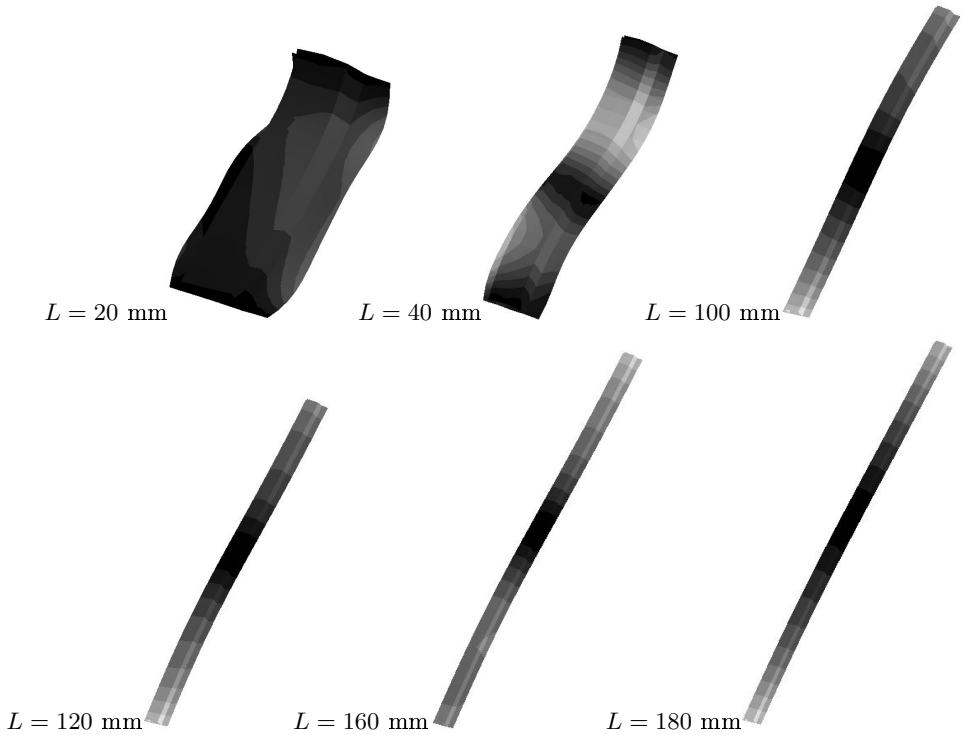

Figure 5.49: Shapes of the worst imperfection for the box beam loaded axially with uniform edge-pressure and simply supported at both ends on skin only, L = 20, 40, 100, 120, 160, 180 mm mm, t/a=3/10.

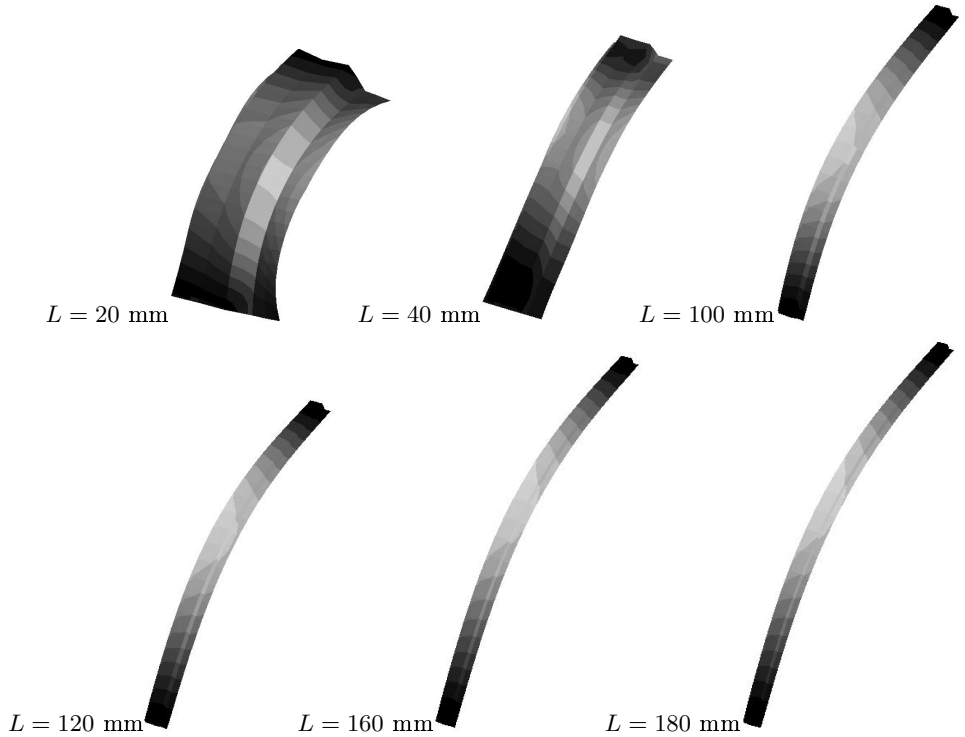

Figure 5.50: Mode shapes at minimum limit load with the worst imperfection for the box beam loaded axially with uniform edge-pressure and simply supported at both ends on skin only, $L = 20$, 40, 100, 120, 160, 180 mm, t/a=3/10.

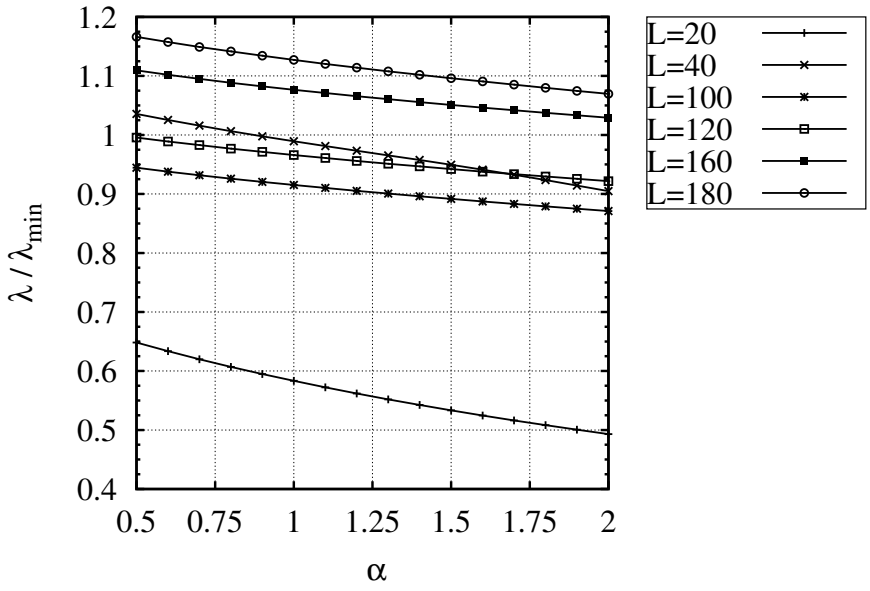

Figure 5.51: Sensitivity curve using the worst imperfection for the box beam loaded axially with uniform edge-pressure and simply supported at both ends on skin only, $L = 20, 40, 100, 120, 160, 180$ mm, t/a=3/10.

5.4 Laminated composite cylindrical shells in compression

The proposed methodology for imperfection sensitivity analysis is general in the sense that it can be applied to any type of slender structure. The particular FE formulation used in this work is based on a flat shell finite element (MISS-4,[15]) that is particularly suitable for the analysis of folded plates [46]. However, curved shells can be analyzed using MISS-4 by approximating the curved shell as a collection of small flat elements with characteristic size h, retaining h^2 convergence of the solution, as shown in [15, Section 4.3] and [109].

The buckling load of thin-walled cylindrical shells is overestimated by theoretical methods mainly due to the high sensitivity to geometrical imperfections of such structures. To tackle this problem, industry currently makes use of the Kock-Down Factor (KDF) approach, es-tablished by NASA in its space vehicle structural guide-lines, published in the 1960s [102]. This method has proved to be robust, but it does not take into account all the laminated composites mechanical properties, which can strongly influence the buckling behaviour [103], thus, lead-ing in most of the cases to overly conservative results [104], [105]. Moreover, these guidelines were built from em-pirical test data from 1930âĂŹs to 1960âĂŹs and therefore the NASA SP-8007 can be considered outdated from the point of view of the new materials and technological so-lutions developed since then.

Since 1970s a considerable number of experimental and numerical observations have been found to support new stochastic and deterministic methods for calculating more realistic knock-down factors (KDFs) for conical and cylindrical shell structures (fore more details see [2], [106],[107] [108], [110], [111], [30]).

In this section, two cylinders labeled Z32 and Z33 [107], are analyzed. These cylinders have been applied as benchmark cases of imperfection sensitivity [112, 114, 113]. The ply properties are $E_1 = 123.6$ GPa; $E_2 = 8.7$ GPa; $G = 5.7$ GPa; $\nu_{12} = 0.32$. The laminate stacking sequence is ${}_{IN}[-51/51/-45/45/-37/37/-19/19/0/0]_{OUT}$ and ${}_{IN}[0/0/19/-19/37/-37/45/-45/51/-51]_{OUT}$ for Z32 and Z33, respectively. The height is $510\,mm$, the radius $R = 250\,mm$ and the laminate thickness $t = 1.25\,mm$. In addition to the radius/thickness $R/t = 200$, the ratios $R/t = 50, 100, 400, 800$ have been analysed.

The cylinders are clamped on top and bottom, except for the axial displacement at the top edge, which is free to allow the application of a distributed load. The imperfection sensitivity analysis has been carried out for different radius versus thickness ratio. A mesh of square elements (6.8×6.8 mm) is used for all cases.

5.4.1 Buckling analysis

The results on buckling loads are reported in Tables 5.8 and 5.9. Buckling modes are shown in Figure 5.52, and the quadratic correction functions are shown in Figure 5.53. Eight buckling modes have been considered for the multi-modal analysis. The limit load distribution considering one thousand imperfections with maximum amplitude $\tilde{u}_{max}/t = 0.2$ is shown in Figure 5.54. The shape of the worst imperfection and the deformed shape at minimum limit load are shown in Figures 5.55 and 5.56,

respectively. The load sensitivity as a function of the amplitude of the worst imperfection is reported in Figure 5.57, where it can be seen that cylinder Z33 is more imperfection sensitive that Z32.

R/t	λ_1	λ_2	λ_3	λ_4	λ_5	λ_6	λ_7	λ_8
50	1680.540	1689.500	1701.370	1701.370	1722.910	1722.890	1771.550	1771.560
100	411.049	413.328	413.613	413.612	417.888	417.891	422.512	422.514
200	103.349	103.562	103.578	103.578	104.278	104.278	104.662	104.660
400	26.744	26.756	26.756	26.767	26.885	26.885	26.887	26.886
800	7.215	7.215	7.217	7.220	7.231	7.231	7.242	7.242

Table 5.8: Buckling loads (in kN) for cylinder Z32 as a function of radius/thickness ratio.

R/t	λ_1	λ_2	λ_3	λ_4	λ_5	λ_6	λ_7	λ_8
50	3195.180	3195.200	3305.300	3305.820	3312.270	3313.840	3355.110	3355.580
100	800.113	800.100	800.496	800.497	804.968	804.982	824.417	825.567
200	199.055	199.055	200.314	200.313	201.449	201.454	202.234	202.236
400	50.578	50.578	50.579	50.579	50.674	50.674	51.056	51.056
800	12.945	12.945	12.957	12.957	13.034	13.034	13.066	13.066

Table 5.9: Buckling loads (in kN) for cylinder Z33 as a function of radius/thickness ratio.

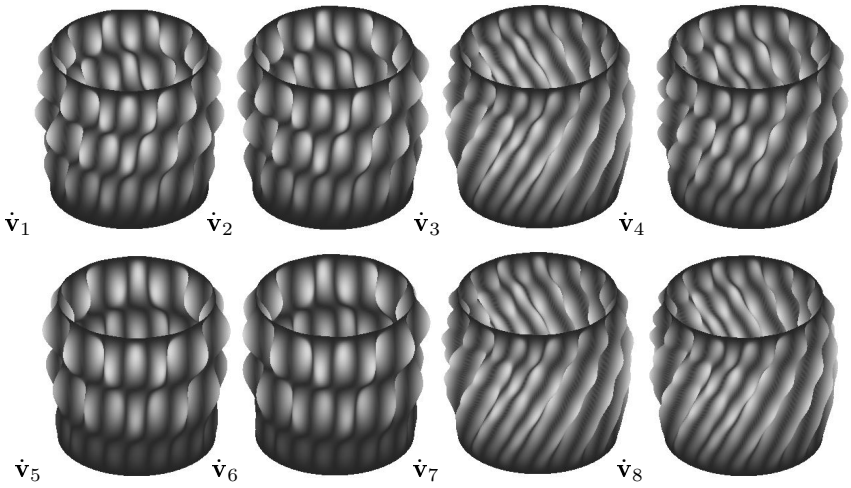

Figure 5.52: Buckling modes for cylinder Z33 with $R/t = 200$.

5.4.2 Post-buckling and imperfection sensitivity analysis

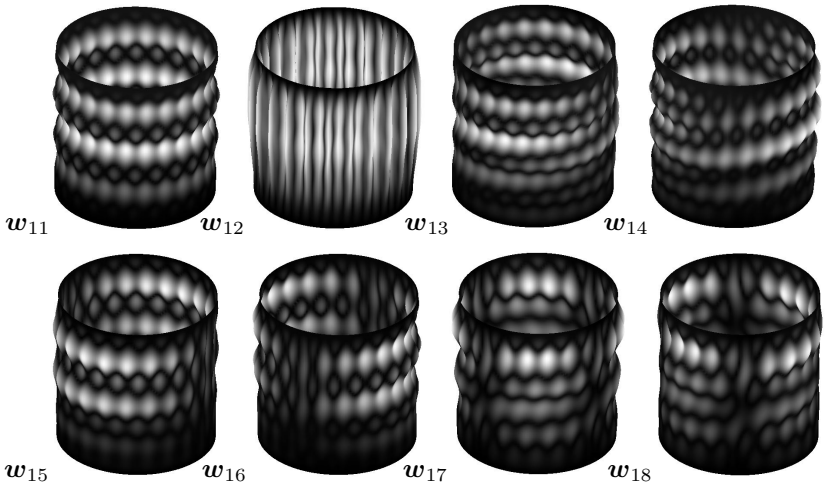

Figure 5.53: Quadratic corrections for cylinder Z33 with $R/t = 200$.

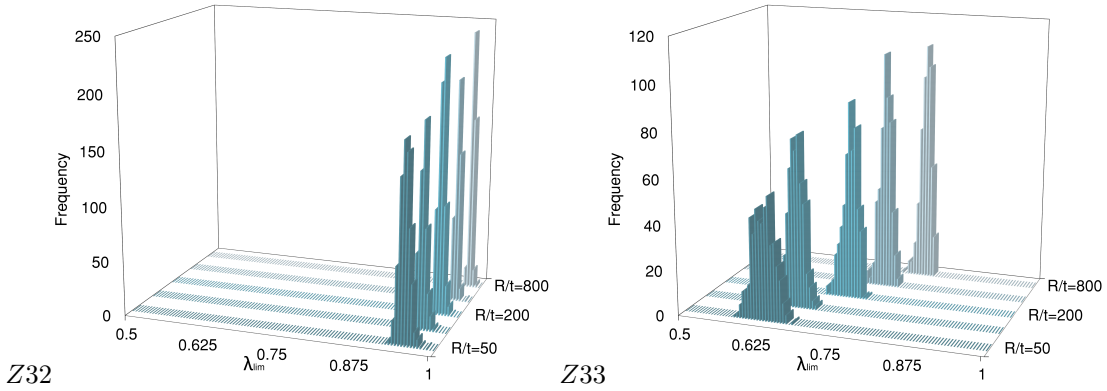

Figure 5.54: Frequency distribution of the lowest limit load λ_{lim} for cylinders Z32 on the left and Z33 on the right at several values of radius-to-thickness ratios.

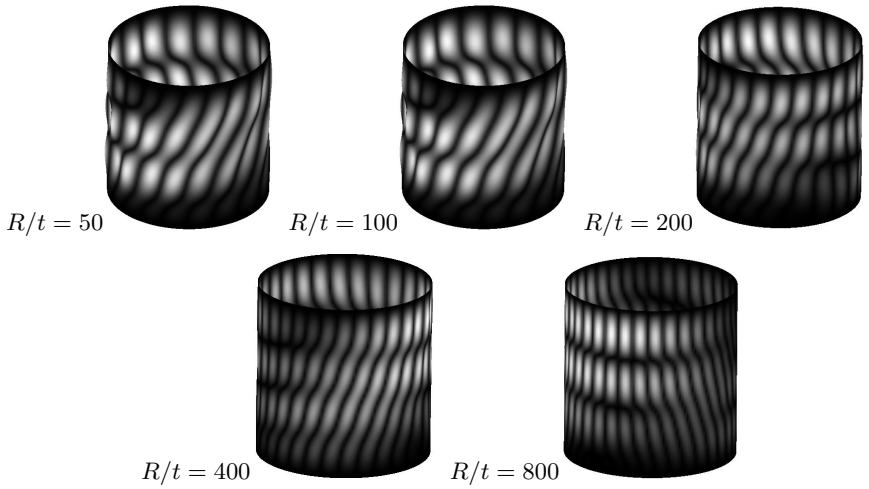

Figure 5.55: Shapes of the worst imperfection for cylinder Z33 at several radius-to-thickness ratios.

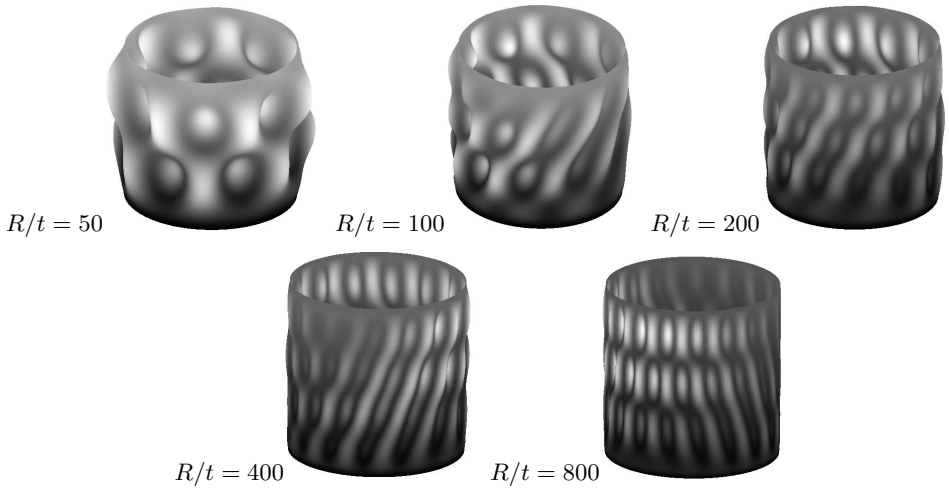

Figure 5.56: Mode shapes at minimum limit load with the worst imperfection for cylinder Z33 and several radius-to-thickness ratios.

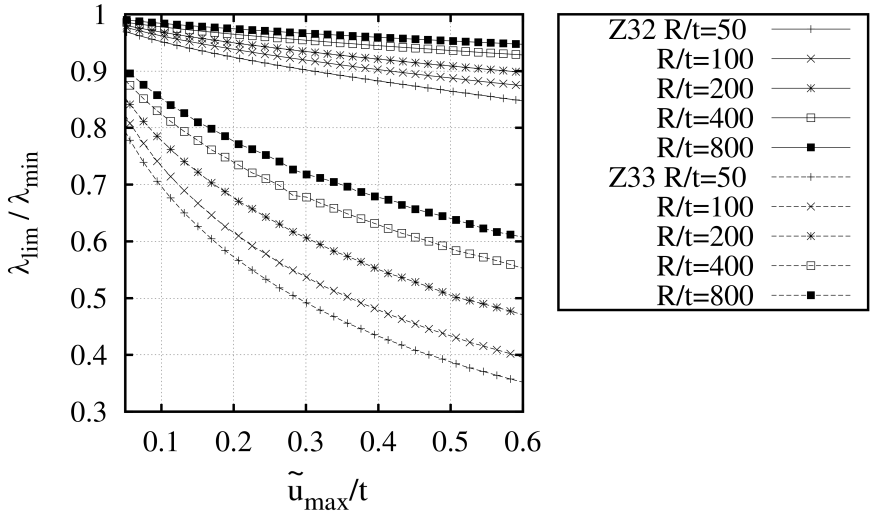

Figure 5.57: Limit load sensitivity to worst imperfection amplitude for cylinders Z32 and Z33 and several radius-to-thickness ratios.

5.4.3 A virtual laboratory for imperfection sensitivity analysis of laminated composite cylindrical shells

In the following, are reported the results of an intensive imperfection sensitivity analysis for several cylinders. Geometrical and mechanical parameters, for each cylinder, are reported in Table (5.10), while the laminate stacking sequence are reported in Table (5.11). For the cylinders $Z07$, $Z15$, $Z33$ and $Z36$ the imperfection sensitivity analysis has been carried out for different radius versus thickness ratio.

Eight buckling modes have been considered for the multi-modal analysis. The first eight buckling load, for the cylinder considered, are reported in the Tables (5.12). The buckling load for the cylinders $Z07$, $Z15$, $Z33$ and $Z36$, for different radius versus thickness ratio, are reported in the Tables (**??**), (5.13), (5.14) and (5.15). One thousand imperfections with maximum amplitude are considered during the simulations. The shape of the worst imperfection and the deformed shape at minimum limit load are shown in Figures 5.58 and 5.59, respectively.

The load sensitivity as a function of the amplitude of the worst imperfection are reported in Figure 5.60, where it can be seen that cylinder $Z33$ is more imperfection sensitive than the cylinders analyzed.

$Cylinder$	$R\ [mm]$	$H\ [mm]$	$t\ [mm]$	$E_1\ [GPa]$	$E_2\ [GPa]$	ν_{12}	$G_{12}\ [GPa]$	$G_{13}\ [GPa]$	$G_{23}\ [GPa]$
$Z07$	250	510	0.125	142.500	8.700	0.28	5.100	5.100	5.100
$Z11$	250	510	0.125	123.550	8.708	0.319	5.695	5.695	3.400
$Z12$	250	510	0.125	123.550	8.708	0.319	5.695	5.695	3.400
$Z14$	250	510	0.125	123.550	8.708	0.319	5.695	5.695	3.400
$Z15$	250	500	0.11575	157.400	8.600	0.28	5.300	5.300	5.300
$Z18$	250	510	0.125	123.550	8.708	0.319	5.695	5.695	3.400
$Z21$	250	510	0.125	123.550	8.708	0.319	5.695	5.695	3.400
$Z36$	400	800	0.125	142.500	8.700	0.28	5.100	5.100	5.100

Table 5.10: Geometrical and mechanical parameters for the cylinders analyzed.

$Cylinder$	LSS
$Z07$	$_{IN}[24, -24, 41, -41]_{OUT}$
$Z11$	$_{IN}[60, -60, 0, 0, 68, -68, 52, -52, 37, -37]_{OUT}$
$Z12$	$_{IN}[51, -51, 45, -45, 37, -37, 19, -19, 0, 0]_{OUT}$
$Z14$	$_{IN}[51, -51, 90, 90, 40, -40]_{OUT}$
$Z15$	$_{IN}[24, -24, 41, -41]_{OUT}$
$Z18$	$_{IN}[-37, 37, -52, 52, -68, 68, 0, 0, -60, 60]_{OUT}$
$Z21$	$_{IN}[39, -39, 0, 0, 50, -50]_{OUT}$
$Z36$	$_{IN}[34, -34, 0, 0, 53, -53]_{OUT}$

Table 5.11: The LSS for each cylinder analyzed.

$Cylinder$	λ_1	λ_2	λ_3	λ_4	λ_5	λ_6	λ_7	λ_8
$Z07$	32.571	32.571	32.770	32.770	33.098	33.098	32.619	33.261
$Z11$	284.079	284.079	285.139	285.140	287.204	287.204	289.283	293.045
$Z12$	101.066	101.282	101.285	101.285	101.285	101.963	102.308	102.309
$Z14$	86.756	86.756	86.783	86.784	87.007	87.008	87.089	87.089
$Z15$	29.429	29.429	29.816	29.816	29.914	29.914	30.032	30.032
$Z18$	233.439	233.439	233.517	233.564	234.636	234.642	234.964	234.973
$Z21$	73.977	73.977	74.058	74.058	74.203	74.203	74.415	74.415
$Z36$	90.151	90.151	90.228	90.228	90.269	90.280	90.501	90.502

Table 5.12: Buckling loads (in kN) for the cylinders $Z07$, $Z11$, $Z12$, $Z14$, $Z15$, $Z18$, $Z21$ and $Z36$.

R/t	λ_1	λ_2	λ_3	λ_4	λ_5	λ_6	λ_7	λ_8
414	50.852	50.852	59.510	51.773	51.773	51.833	52.240	52.240
439	44.947	44.948	52.041	45.654	45.654	46.088	46.243	46.243
464	40.130	40.130	46.177	40.532	40.532	41.025	41.361	41.361
489	36.108	36.108	41.053	36.212	36.212	36.746	36.942	36.942
514	32.535	32.535	36.530	32.699	32.699	33.068	33.196	33.196
539	29.429	29.429	32.770	29.816	29.816	29.914	30.032	30.032
639	20.678	20.678	22.501	20.727	20.727	20.979	21.010	21.010
739	15.318	15.318	16.336	15.507	15.507	15.567	15.622	15.622
839	11.852	11.852	12.454	11.854	11.854	11.970	11.984	11.984
939	9.367	9.367	9.745	9.471	9.471	9.495	9.501	9.501
1039	7.637	7.637	7.888	7.658	7.658	7.705	7.727	7.727

Table 5.13: Buckling loads (in kN) for the cylinders $Z15$ as a function of R/t.

R/t	λ_1	λ_2	λ_3	λ_4	λ_5	λ_6	λ_7	λ_8
75	1404.934	1404.937	1414443.00	1414.469	1448.244	1448.275	1469.149	1469.149
100	789.015	789.018	790795.90	790.801	797.558	797.570	809.825	810.264
125	502.389	502.391	503868.20	503.871	505.992	505.995	514.126	514.156
150	344.372	344.372	346655.40	346.655	349.181	349.181	353.277	353.327
175	255.233	255.233	255883.70	255.883	256.690	256.691	258.643	258.643
200	199.055	199.055	200.314	200.313	201.449	201.454	202.234	202.236
300	86.661	86.661	86865.41	86.865	86.995	86.995	87.174	87.173
400	48.861	48.861	48981.09	48.981	48.993	48.993	49.176	49.176
500	31.353	31.353	31419.36	31.419	31.435	31.435	31.508	31.508
600	21.819	21.819	21876.92	21.876	21.882	21.882	21.897	21.897
700	16.074	16.074	16094.15	16.094	16.136	16.136	16.139	16.139

Table 5.14: Buckling loads (in kN) for the cylinders $Z33$ as a function of R/t.

R/t	λ_1	λ_2	λ_3	λ_4	λ_5	λ_6	λ_7	λ_8
408	151.504	151.504	151.705	151.710	151.719	151.730	152.329	152.328
433	134.912	134.913	135.075	135.076	135.088	135.124	135.592	135.595
458	120.972	120.973	121.105	121.106	121.135	121.151	121.540	121.542
483	108.965	108.965	109.074	109.075	109.105	109.126	109.443	109.444
508	98.940	98.941	99.032	99.032	99.069	99.081	99.348	99.349
533	90.151	90.151	90.228	90.228	90.269	90.280	90.501	90.502
633	64.693	64.693	64.734	64.734	64.768	64.779	64.896	64.897
733	48.804	48.804	48.828	48.828	48.858	48.862	48.933	48.933
833	38.236	38.236	38.251	38.251	38.275	38.278	38.323	38.323
933	30.826	30.826	30.836	30.836	30.856	30.857	30.888	30.888
1033	25.428	25.428	25.436	25.436	25.451	25.453	25.475	25.475

Table 5.15: Tthe cylinders $Z36$ as a function of R/t .

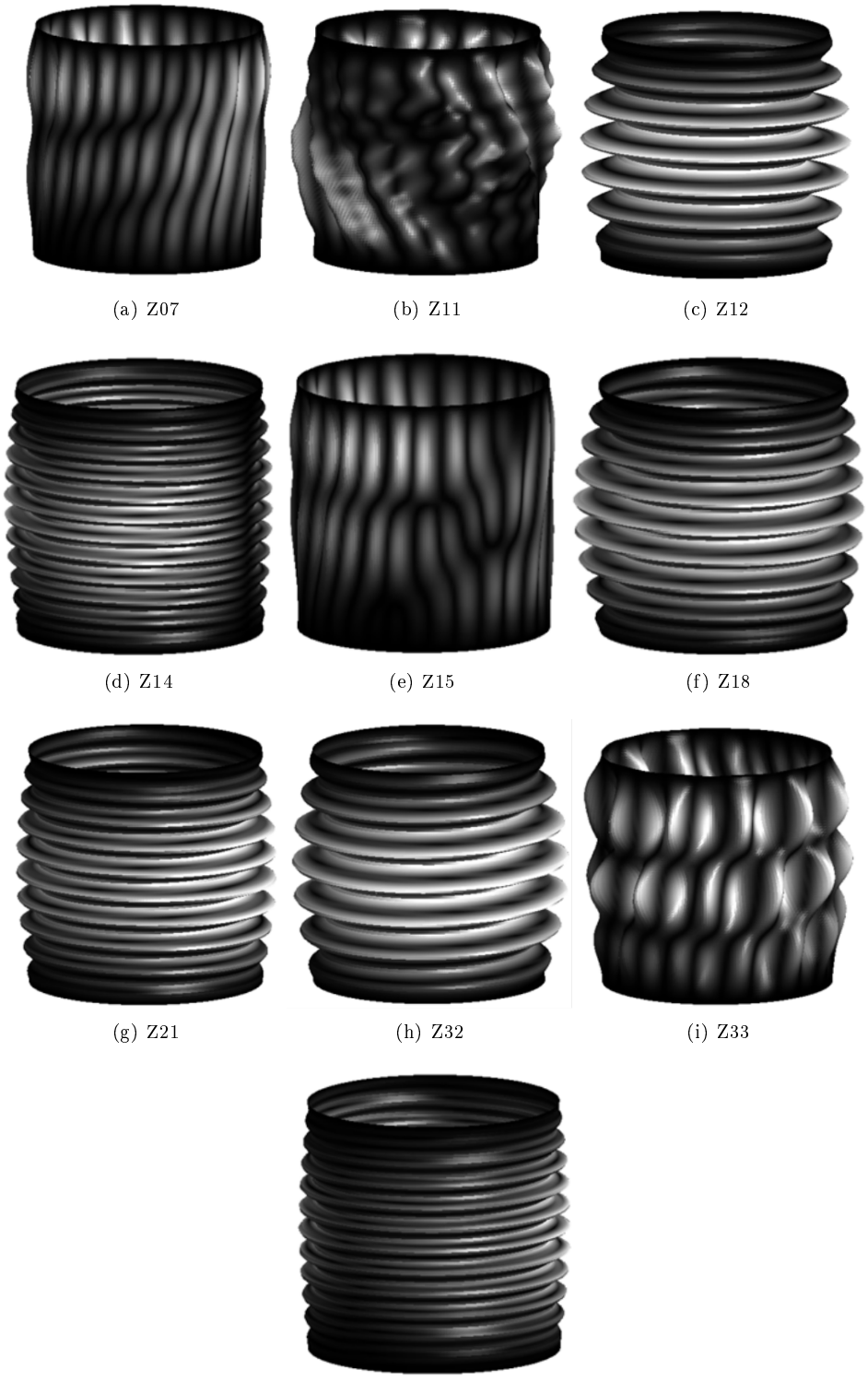

(a) Z07 (b) Z11 (c) Z12

(d) Z14 (e) Z15 (f) Z18

(g) Z21 (h) Z32 (i) Z33

(j) Z36

Figure 5.58: Shapes of the worst imperfection for several cylinders using 1000 geometrical imperfection.

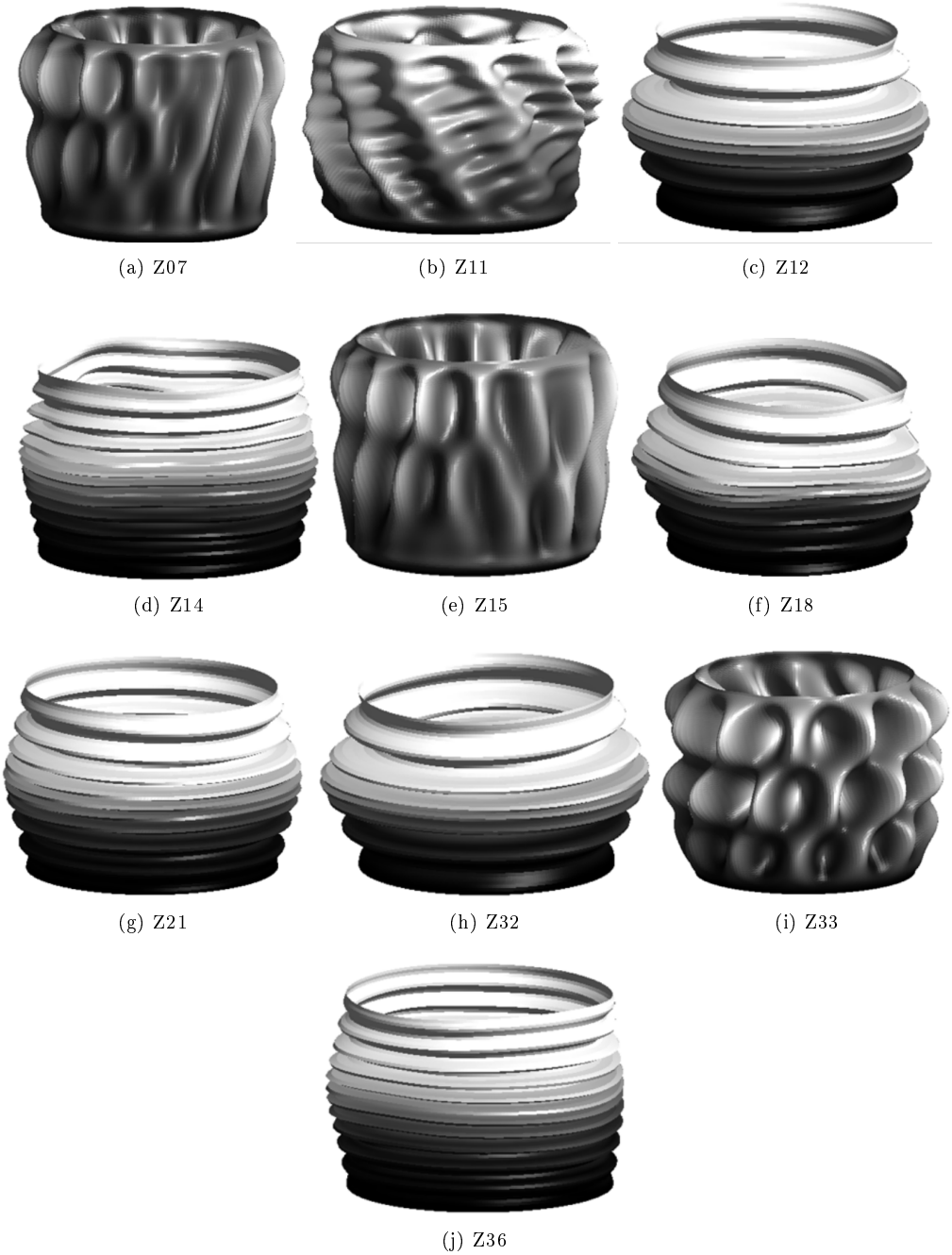

(a) Z07 (b) Z11 (c) Z12

(d) Z14 (e) Z15 (f) Z18

(g) Z21 (h) Z32 (i) Z33

(j) Z36

Figure 5.59: Shapes of the worst deformation for several cylinders using 1000 geometrical imperfection.

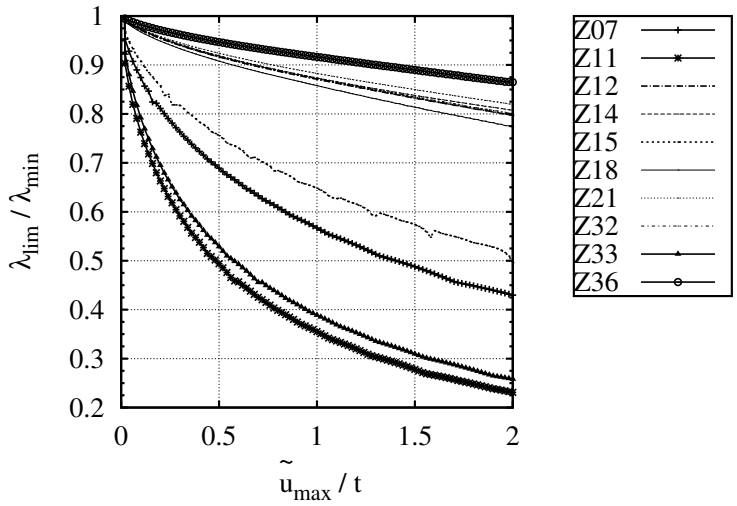

Figure 5.60: Limit load sensitivity to worst imperfection amplitude for cylinders $Z07$, $Z11$, $Z12$, $Z14$, $Z15$, $Z18$, $Z21$, $Z32$, $Z33$ and $Z36$ using 1000 geometrical imperfection.

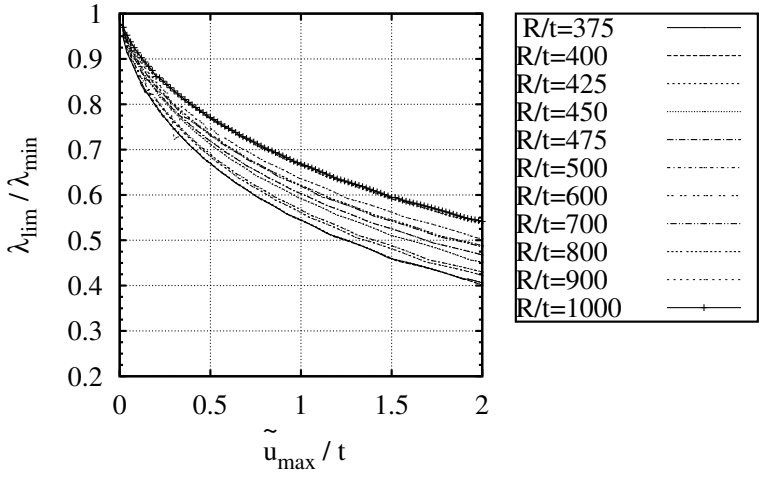

Figure 5.61: Limit load sensitivity to worst imperfection amplitude for cylinder $Z07$ and several radius-to-thickness ratios.

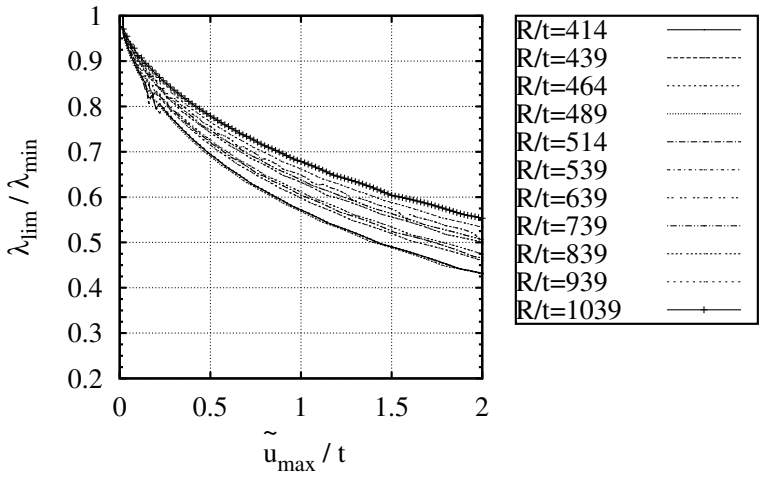

Figure 5.62: Limit load sensitivity to worst imperfection amplitude for cylinder $Z15$ and several radius-to-thickness ratios.

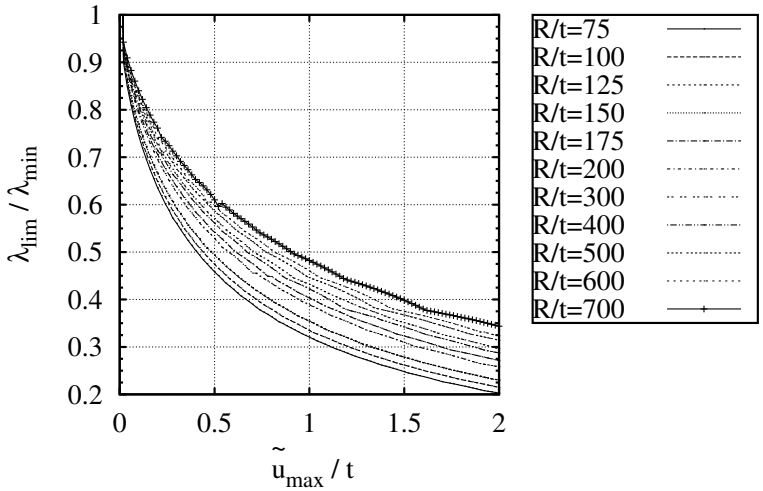

Figure 5.63: Limit load sensitivity to worst imperfection amplitude for cylinder $Z33$ and several radius-to-thickness ratios.

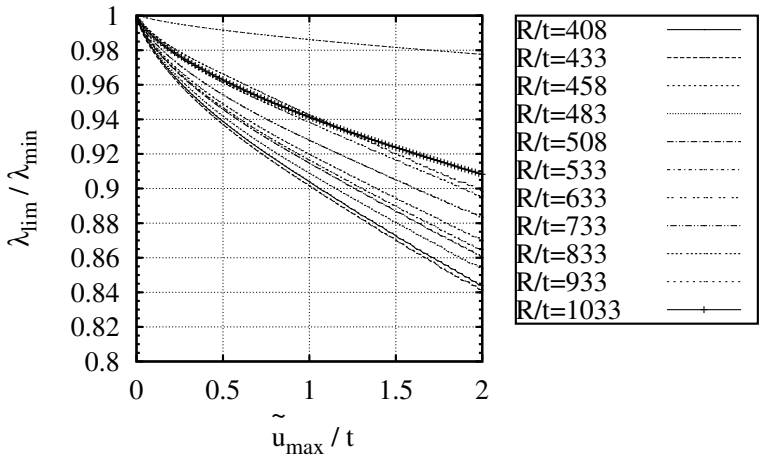

Figure 5.64: Limit load sensitivity to worst imperfection amplitude for cylinder $Z36$ and several radius-to-thickness ratios.

5.4.4 Further remarks

The imperfection sensitivity analysis in the context of Koiter's approach allows us to perform Monte Carlo simulation with very low computational cost. Analysis time is reported in Table 5.16. The computations are performed on a Intel(R) Xeon(R) CPU E5-2620 2.00Ghz Dual Core, 32 GB Ram on a single core. Each value in Table 5.16 requires the solution of eq. (1.7h) for as many random imperfections as indicated in the heading for that column.

The average time required for the steps i. to iv. have been studied [11], and they remain of the order of seconds. The times are also a few seconds for a very large number of imperfections. This could allow users to run Monte Carlo simulations to account for other types of imperfections (i.e., load imperfection, residual stress, and so on) in order to obtain even more realistic evaluations of structural performance.

For the example studied, an imperfection in the shape of the first buckling mode (see $\hat{\boldsymbol{v}}$ in Figure 5.52) does not necessarily produce the worst imperfection (see Figure 5.55). Also, the buckling modes for minimum limit load do not resemble the worst imperfection. These observations provide empirical justification for performing a full exploration of the imperfection space, as proposed in this work.

The accuracy, robustness, and reliability of the results are closely related to the use of geometrically exact structural models and mixed formulation. The latter is necessary to prevent extrapolation locking phenomena [14]. The use of a corotational formulation coupled with a mixed finite element allows to easily satisfy these requirements. Moreover, Koiter's approach being based on asymptotic expansion, allows to recover the equilibrium path in an approximate fashion. The best accuracy is available for the pre-critical and the initial post-critical behavior. A numerical comparison between Riks' and Koiter's method for the recovery a single equilibrium path, as implemented in this paper, can be found in [8, 9, 11].

The accuracy of imperfection sensitivity of Koiter's analysis compared to Riks' analysis are shown (numerically) in Figure 5.65. The path-following solution is obtained using Riks' standard implementation in Abaqus [84] along withS4R element. The accuracy of our implementation of Koiter's method

(Section 1) decreases with the imperfection amplitude. This is due to the fact that the imperfections are incorporated during post-processing, i.e. eq. (1.7h), in order to keep the computational cost to a minimum. A method for improving the imperfection amplitude range of Koiter's method is reported by [117] along with an extensive discussion on calculations of imperfection sensitivity curves for unstiffened and stiffened cylinders is also reported.

	Time (s)				
R/t	100 imp.	500 imp.	1000 imp.	5000 imp.	10000 imp.
50	18.011	89.688	270.346	5344.72	10764.88
100	14.403	67.853	242.540	5434.89	10599.07
200	14.643	77.345	249.089	5350.40	10480.74
400	19.964	97.050	285.614	5275.00	10193.00
800	11.652	60.923	217.769	5106.57	10694.88

Table 5.16: Computational cost for cylinder Z33 and several radius-to-thickness ratios. The cost refers to the solution of equation (1.7h).

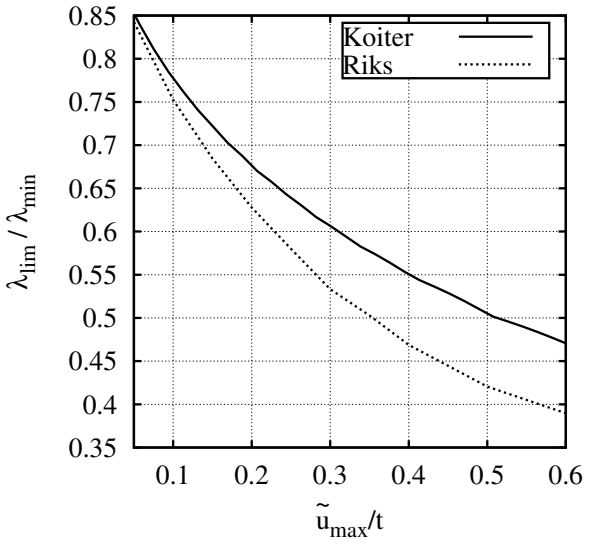

Figure 5.65: Load sensitivity to worst imperfection $\tilde{u}_{max}$ for cylinder Z33 with $R/t = 200$.

Conclusions

The advantages of using Koiter's asymptotic approach for the analysis of slender elastic structures has been shown. The possibility of performing an efficient and reliable imperfection sensitivity analysis, including cases with modal interaction, based on Monte Carlo simulation has been demonstrated. The computational cost needed to account for a large sample of imperfections is, on average, in the range of a few seconds. The worst imperfections can be detected without a-priori knowledge about the shape of such imperfections. The load capacity can evaluated statistically and its sensitivity to the amplitude of the worst imperfection can be calculated easily.

Acknowledgement

Though only my name appears on the cover of this dissertation, a great many people have contributed to its production. I owe my gratitude to all those people who have made this dissertation possible and because of whom this experience has been one that I will cherish forever.

My deepest gratitude is to Professor R. Zinno who gave me a great opportunity, bringing in every way my training.

I am deeply grateful to Professor R. Casciaro for the long discussions that helped me sort out the technical details of my work.

Dr. A. Madeo's insightful comments and constructive criticisms at different stages of my research were thought-provoking. I am grateful to him for holding me to a high research standard and enforcing strict validations for each research result, and thus teaching me how to do research.

I am indebted to dr. G. Zagari for his continuous encouragement and guidance. I am also indebted to the members of the SMARTLAB Laboratory with whom I have interacted during the course of my PhD. I am very grateful to Professor D. Bruno that, during these three years, has been a Friend and a Professor always present.

I am very grateful to Professor E. J. Barbero, from West Virginia University, for remote collaboration and excellent results obtained with him.

I would like to express my very sincere gratitude to Professors D. Dubina and V. Ungureanu for the friendly hospitality at the prestigious Polytechnic University of Timisoara. I acknowledge my gratitude to the Professor P. Weaver and dr. R. Groh, from University of Bristol, for the absolute support in the lasts months of my research. Finally, I take this opportunity to express the profound gratitude from my deep heart to my beloved parents and my sister for their love and continuous support both spiritually and materially.

Bibliography

[1] Daoud F, Calomfirescu M. Optimization of Composite Aircraft Structures in Consideration of Postbuckling Behavior. Int J Str Stab Dyn 2010; 10(4):905-916.

[2] Degenhardt R, Castro SGP, Arbelo MA, Zimmerman R, Khakimova R, Kling A. Future structural stability design for composite space and air frame structures. Thin Wall Struct 2014; 81:29-38.

[3] Riks E. An incremental approach to the solution of snapping and buckling problems. Int J Solids Struct 1979; 15(7):529-551.

[4] Kouhia R, Mikkola M. Tracing the equilibrium path beyond compound critical points. Int J Numer Meth Eng 1999; 46(7):1049-1074.

[5] Koiter WT. On the stability of elastic equilibrium. 1945; English transl. NASA TT-F10, 883 (1967) and AFFDL-TR70-25 (1970).

[6] Casciaro R. Computational asymptotic post-buckling analysis of slender elastic structures. Phenomenological and Mathematical Modelling of Structural Instabilities, Springer Vienna 2005; 470:195-276.

[7] Barbero EJ. Prediction of Compression Strength of Unidirectional Polymer Matrix Composites. J Compos Mater 1998; 32(5):483-502.

[8] Garcea G, Madeo A, Zagari G, Casciaro R. Asymptotic post-buckling FEM analysis using corotational formulation. Int J Solids Struct 2009; 46(2):377-397.

[9] Zagari G, Madeo A, Casciaro R, de Miranda S, Ubertini F. Koiter analysis of folded structures using a corotational approach. Int J Solids Struct 2013; 50(5):755-765.

[10] Zagari G. Koiter's asymptotic numerical methods for shell structures using a corotational formulation 2009; 50(5):755-765. Tesi di Dottorato.

[11] Barbero EJ, Madeo A, Zagari G, Zinno R, Zucco G. Koiter asymptotic analysis of folded laminated composite plates. Composites Part B 2014; 61:267-274.

[12] Garcea G, Madeo A, Casciaro R. The implicit corotational method and its use in the derivation of nonlinear structural models for beams and plates. J Mech Mat Struct 2012; 7(6):509-538.

[13] Garcea G, Madeo A, Casciaro R. Nonlinear FEM analysis for beams and plate assemblages based on the Implicit Corotational Method. J Mech Mat Struct 2012; 7(6):539-574.

[14] Garcea G, Salerno G, Casciaro R. Sanitizing of locking in Koiter perturbation analysis through mixed formulation. Comput Method Appl M 1999; 180:137-167.

[15] Madeo A, Zagari G, Casciaro R, Miranda S. A Mixed 4-Node 3D plate Element Based on Self-Equilibrated Isostatic Stresses. Int J Str Stab Dyn 2014; DOI: 10.1142/S0219455414500667

[16] Madeo A, Zagari G, Casciaro R. An isostatic quadrilateral membrane finite element with drilling rotations and no spurious modes. Finite Elem Anal Des 2012; 50:21-32

[17] Pian THH, Sumihara K. Rational approach for assumed stress finite elements. Int J Numer Methods Eng, 1984; 20(9): 1685-1695.

[18] Godoy LA. Theory of Elastic Stability-Analysis and Sensitivity. Taylor and Francis 1999.

[19] Barbero EJ. Prediction of Buckling-Mode Interaction in Composite Columns. Mech Compos Mater St 2000; 7:269-284.

[20] Barbero EJ, Dede E, Jones S. Experimental Verification of Buckling-Mode Interaction in Intermediate-Length Composite Columns. Int J Solids Struct 2000; 37:3919-3934.

[21] Garcea G., Bilotta A, Madeo A, Casciaro R. Direct evaluation of the post-buckling behaviour of slender structures through a numerical asymptotic formulation. Direct Methods for Limit States in Structures and Materials 2014; 203-228.

[22] Godoy LA, Barbero EJ, Raftoyiannis IG. Finite elements for post-buckling analysis. I - the w-formulation. Comput Struct 1995; 56(6):1009–1017.

[23] Godoy LA. Thin-Walled Structures with Structural Imperfections. NY Elsevier, 1996.

[24] Allman DJ. A compatible triangular element including vertex rotations for plane elasticity analysis. Comput Struct, 1984; 19(1-2): 1-8.

[25] Allman DJ. A quadrilateral fiite element including vertex rotations for plane elasticity analysis. Int J. Numer Methods Eng, 1988; 26(3): 717-730.

[26] Hughes T, Brezzi F. On drilling degrees of freedom. Comput Methods Appl Mech Eng, 1989; 72(1): 105-121.

[27] Dubina D. The ECBL approach for interactive buckling of thin-walled steel members. Steel and Composite Structures 2001; 1(1):75-96.

[28] Dubina D, Ungureanu V. Effect of imperfections on numerical simulation of instability behaviour of cold-formed steel members. Thin Wall Struct 2002; 40(3):239-262.

[29] Dubina D, Ungureanu V. Instability mode interaction: From Van Der Neut model to ECBL approach. Thin Wall Struct 2014; 81:39-49.

[30] Castro SGP, Zimmermann R, Arbelo MA, Khakimova R, Hilburger MW, Degenhardt R. Geometric imperfections and lower-bound methods used to calculate knock-down factors for axially compressed composite cylindrical shells. Thin Wall Struct 2014; 74:118-132.

[31] Arbelo MA, Degenhardt R, Castro SGP, Zimmermann R. Numerical characterization of imperfection sensitive composite structures. Compos Struct 2014; 108:295-303.

[32] Orifici AC, Bisagni C. Perturbation-based imperfection analysis for composite cylindrical shells buckling in compression. Compos Struct 2013; 106:520-528.

[33] Barbero EJ, Madeo A, Zagari G, Zinno R, Zucco G. Imperfection sensitivity analysis of laminated folded plates.Thin-Walled Structures 90, 128-139.

[34] Garcea G. Mixed formulation in Koiter analysis of thin-walled beam. Computer Methods in Applied Mechanics and Engineering 2001; 190: 3369âĂŞ3399.

[35] Garcea G. Asymptotic post-buckling analysis of rectangular plates by HC finite elements. International Journal for Numerical Methods in Engineering 1995; 38: 2325âĂŞ2345.

[36] Rankin C.C., Nour-Omid B. The use of projectors to improve finite element performance. Computer and Structures 1998; 30: 257âĂŞ267.

[37] Nour-Omid B., Rankin C.C.. Finite rotation analysis and consistent linearization using projectors. Computer Methods in Applied Mechanics and Engineering 1991; 93: 353âĂŞ384.

[38] Crisfield, M.A., 1997. Nonlinear Finite Element Analysis of Solids and Structures, vol. 1âĂŞ2. Wiley, Chichester.

[39] Barbero EJ. Introduction to composite materials design–Second Edition. Boca raton, FL: CRC Press, 2010.

[40] Davalos JF, Chen A, Qiao P. FRP Deck and Steel Girder Bridge Systems: Analysis and Design. Boca Raton, FL: CRC Press, 2013.

[41] Arbelo MA, de Almeida SFM, Donadon MV, Rett SR, Degenhardt R, Castro SGP, Kalnins K, Ozoliņš O. Vibration correlation technique for the estimation of real boundary conditions and buckling load of unstiffened plates and cylindrical shells. Thin Wall Struct 2014; 79:119-128.

[42] Reddy JN. Mechanics of Laminated Composite Plates and Shells - Theory and Analysis Boca Raton: CRC Press, 2004.

[43] MATLAB. The Mathworks. Boston, MA, 2013.

[44] Laitinen M, Lahtinen H, Sjölind S G. Transverse shear correction factors for laminates in cylindrical bending. Commun Numer Methods in Eng, 1995; 11(1): 41-47.

[45] de Miranda S, Ubertini F. A simple hybrid stress element for shear deformable plates. Int J Numer Methods Eng, 2006; 65(6): 808-833.

[46] Barbero EJ, Madeo A, Zagari G, Zinno R, Zucco G. A mixed isostatic 24 dof element for static and buckling analysis of laminated folded plates. Compos Struct 2014; 116:223-234.

[47] Barbero EJ, Madeo A, Zagari G, Zinno R, Zucco G. A Mixed Finite Element for Static and Buckling Analysis of Laminated Folded Plates. The Twelfth International Conference on Computational Structures Technology.

[48] Barbero EJ, Madeo A, Zagari G, Zinno R, Zucco G. ASYMPTOTIC POST-BUCKLING FEM ANALYSIS OF LAMINATED COMPOSITE FOLDED PLATES. ECCM-16^{TH} EUROPEAN CONFERENCE ON COMPOSITE MATERIALS, Seville, Spain, 22-26 June 2014.

[49] Madeo A, Casciaro R, Zagari G, Zinno R, Zucco G. A mixed isostatic 16 dof quadrilateral membrane element with drilling rotations, based on Airy stresses. Finite Elements in Analysis and Design 89, 52-66.

[50] Barbero EJ. Introduction to Composite Materials Design. CRC, Boca Raton, FL, second edition, 2011.

[51] Mostafa M, Sivaselvan MV, Felippa CA. A solid-shell corotational element based on ANDES, ANS and EAS for geometrically nonlinear structural analysis. Int J Numer Meth Eng 2013. 95(2):145-180.

[52] Mostafa M, Sivaselvan MV, Felippa CA. Reusing linear finite elements in material and geometrically nonlinear analysis-Application to plane stress problems. Finite Elem Anal Des 2013; 69:62-72.

[53] Caselli F, Bisegna P. Polar decomposition based corotational framework for triangular shell elements with distributed loads. Int J Numer Meth Eng 2013; 95(6):499-528.

[54] Li ZX, Liu YF, Izzuddin BA, Vu-Quoc L. A stabilized co-rotational curved quadrilateral composite shell element. Int J Numer Meth Eng 2011; 86(8):975-999.

[55] Maunder EAW, Izzuddin BA. A hybrid equilibrium element for folded plate and shell structures, Int J Numer Methods Eng, 2013; 95:451-477.

[56] Norachan P Suthasupradit S, Kim KD. A co-rotational 8-node degenerated thin-walled element with assumed natural strain and enhanced assumed strain. Finite Elem Anal Des 2012; 50:70-85.

[57] Rodrigues O. Des lois géométriques qui régissent les déplacements d'un système solide dans l'espace, et de la variation des coordonnées provenant de ces déplacements considérés indépendamment des causes qui peuvent les produire. J Math Pure Appl 1840; 5:380-440.

[58] Bilotta A, Casciaro R. Assumed stress formulation of high order quadrilateral elements with an improved in-plane bending behaviour. Comput Meth Appl Mech Eng, 2002; 191(15-16): 1523-1540.

[59] Hibbitt, Karlsson, Sorensson. Abaqus theory manual, version 6.8, Dassault 2009.

[60] Zhang YX, Yang CH. Recent developments in finite element analysis for laminated composite plates. Compos Struct, 2009; 88(1): 147-157.

[61] Khandam R, Noroozi S, Sewell P, Vinney J. The development of laminated composite plate theories: a review. J Mater Sci, 2012; 47: 5901-5910.

[62] Zhang YX, Kim KS. Two simple and efficient displacement-based quadrilateral elements for the analysis of composite laminated plates. Int J Numer Methods Eng, 2004; 61(11): 1771-1796.

[63] Zhang YX, Kim KS. A simple displacement-based 3-node triangular element for linear and geometrically nonlinear analysis of laminated composite plates. Comput Meth Appl Mech Eng, 2005; 194(45): 4607-4632.

[64] Gendy AS, Saleeb AF. Free vibrations and stability analysis of laminated composite plates and shells with hybrid/mixed formulation. Comput Struct, 1997; 63(6): 1149-1163.

[65] Auricchio F, Sacco E. A mixed-enhanced finite-element for the analysis of laminated composite plates. Int J Numer Methods Eng, 1999; 44: 1481-1504.

[66] Auricchio F, Sacco E. Partial-mixed formulation and refined models for the analysis of composite laminates within an FSDT. Compos Struct 1999; 46(2): 103-113.

[67] Barbero EJ. Finite Element Analysis of Composite Materials using Abaqus. CRC Press, 2013.

[68] Daghia F, de Miranda S, Ubertini F, Viola E. A hybrid stress approach for laminated composite plates within the First-order Shear Deformation Theory. Int J Solids Struct, 2008; 45(6): 1766-1787.

[69] Moleiro F, Mota Soares CM, Mota Soares CA, Reddy JN. Mixed least-squares finite element model for the static analysis of laminated composite plates. Comput Struct, 2008; 86(9): 826-838.

[70] Hiller JF, Bathe KJ. Measuring convergence of mixed finite element discretizations: an application to shell structures. Comput Structs, 2003; 81(8): 639-654.

[71] Alfano G, Auricchio F, Rosati L, Sacco E. MITC finite elements for laminated composite plates. Int J Numer Methods Eng, 2001; 50(3): 707-738.

[72] Hossain SJ, Sinha PK, Sheikh AH. A finite element formulation for the analysis of laminated composite shells. Comput Struct, 2004; 82(20-21): 1623-1638.

[73] Thai CH, Nguyen-Xuan H, Nguyen-Thanh, Le TH, Nguyen-Thoi T, Rabczuk T. Static, free vibration, and buckling analysis of laminated composite Reissner-Mindlin plates using NURBS-based isogeometric approach. Int J Numer Methods Eng, 2012; 91(6): 571-603.

[74] Liu GR, Zhao X, Dai KY, Zhong ZH, Li GY, Han X. Static and free vibration analysis of laminated composite plates using the conforming radial point interpolation method. Compos Sci Technol, 2008; 68(2): 354-366.

[75] Sgambitterra G, Adumitroaie A, Barbero EJ, Tessler A. A robust three-node shell element for laminated composites with matrix damage. Composites Part B, 2011; 42(1):41-50.

[76] Eby D, Averill RC. Zig-zag sublaminate model for nonlinear analysis of laminated panels. J Aerosp Eng, 2000; 13(3):100-109.

[77] Carrera E, Miglioretti F, Petrolo M. Accuracy of refined finite elements for laminated plate analysis. Compos Struct, 2011; 93(5): 1311-1327.

[78] Khosravi P, Ganesan R, Sedaghati R. An efficient facet shell element for corotational nonlinear analysis of thin and moderately thick laminated composite structures, Comput Struct, 2008; 86:850-858.

[79] Wang Z, Sun Q. Corotational nonlinear analyses of laminated shell structures using a 4-node quadrilateral flat shell element with drilling stiffness, Acta Mech Sin, 2013,doi 10.1007/s10409-014-0009-x.

[80] Andrade LG, Awruch AM, Morsch IB. Geometrically nonlinear analysis of laminate composite plates and shells using the eight-node hexahedral element with one-point integration, Compos Struct, 2007; 79:571-580.

[81] Schafer BW. Cold-formed steel structures around the world, Steel Construction 2011; (4) 3.

[82] Benedetti A, de Miranda S, Ubertini F. A posteriori error estimation based on the superconvergent Recovery by Compatibility in Patches. Int J Numer Methods Eng, 2006; 67: 108-131.

[83] de Miranda S, Patruno L, Ubertini F. Transverse stress profiles reconstruction for finite element analysis of laminated plates. Compos Struct, 2012; 94(9): 2706-2715.

[84] Hibbitt, Karlsson, and Sorensson. Abaqus theory manual, version 6.8. Dassault, 2009.

[85] Reddy JN. Mechanics of Laminated Composite Plates and Shells - Theory and Analysis. Boca Raton: CRC Press, 1997.

[86] Raju G, Wu Z, Weaver PM. Postbuckling analysis of variable angle tow plates using differential quadrature method. Compos Struct, 2013; 106: 74-84.

[87] Lindgaard E, Lund E. Nonlinear buckling optimization of composite structures. Comput Meth Appl Mech Eng, 2010; 199(37-40): 2319-2330.

[88] Sze KY, Liu XH, Lo SH. Popular benchmark problems for geometric nonlinear analysis of shells. Finite Elem Anal Des 2004;40: 1551–1569.

[89] Debski H, Kubiak T, Teter A. Experimental investigation of channel-section composite profiles behavior with various sequences of plies subjected to static compression. Thin Walled Struct 2013;71:147–154.

[90] Brezzi F, Cornalba M, Di Carlo A. How to get around a simple quadratic fold. Numerische Mathematik 1986;48(4);417–427.

[91] Debski H, Kubiak T, Teter A. Buckling and postbuckling behaviour of thin-walled composite channel section column. Compos Struct 2013;100:195–204.

[92] Teter A, Kolakowski Z. Interactive buckling and load carrying capacity of thin walled beam columns with intermediate stiffeners. Thin Walled Struct 2004;42:211–254.

[93] Teter A, Kolakowski Z. Buckling of thin–walled composite structures with intermediate stiffeners. Compos Struct 2005;69: 421–428.

[94] Crisan A, Ungureanu V, Dubina D. Behaviour of cold-formed steel perforated sections in compression. Part 1-Experimental investigations. Thin Wall Struct 2012;61:86-96.

[95] Crisan A, Ungureanu V, Dubina D. Behaviour of cold-formed steel perforated sections in compression: Part 2-numerical investigations and design considerations. Thin Wall Struct 2012; 61:97-105.

[96] Ungureanu V, Dubina D. Sensitivity to Imperfections of Perforated Pallet Rack Sections. Mechanics and Mechanical Engineering 2013;17(2):207-220.

[97] Papadopoulos V, Soimiris G, Papadrakakis M. Buckling analysis of I-section portal frames with stochastic imperfections. Eng Struct 2013;47:54-66.

[98] Ungureanu V, Dubina D, Madeo A, Zagari G, Zucco G, Zinno R. Koiter Asymptotic Analysis of Thin-Walled Cold-Formed Steel Members. The Eighth International Conference on Advances in Steel Structures 2015.

[99] Salerno G, Casciaro R. Mode jumping and attrative paths in multimode elastic buckling. Int J Numer Meth Eng 1997; 40:833-861.

[100] Casciaro R, Mancusi G. Imperfection sensitivity due to coupled local instability: a non-convex QP solution algorithm. Int J Numer Meth Eng 2006; 67(6):815-840.

[101] Salerno G, Uva G. Ho's theorem in global−local mode interaction of pin-jointed bar structures. Int J Nonlinear Mech 2006; 41(3):359-376.

[102] Weingarten V. I., Seide P., Peterson J. P. Buckling of thin-walled circular cylinders. NASA SP-8007. Wash-ington, (DC, USA): National Aeronautics and Space Administration; 1968.

[103] Geier B., Meyer-Piening H.-R., Zimmermann R. On the influence of laminate stacking on buckling of com-posite cylindrical shells subjected to axial compres-sion. Composite structures, vol. 55, no. 4, p. 467-474, 2002.

[104] Arbocz J., Starnes Jr J.H. Future directions and chal-lenges in shell stability analysis. Thin-Walled Struc-tures, vol. 40, no 9, p. 729-754, 2002.

[105] R., Berthge A., Kling A., Zimmermann R., Rohwer K., Tessmer J. et al. Probabilistic approach for improved buckling knock-down factors of CFRP cylindrical shells. In proceedings of: First CEAS Eu-ropean Air and Space Conference, 2008.

[106] DESICOS [online], http://www.desicos.eu/.

[107] Castro SGP, Zimmermann R, Arbelo MA, Degenhardt R. Exploring the constancy of the global buckling load after a critical geometric imperfection level in thin-walled cylindrical shells for less conservative knock-down factors. Thin Wall Struct 2013; 72:76-87.

[108] Khakimova R, Castro SGP, Arbelo MA, Degenhardt R, Rohwer K, Zimmermann R., et al.Studies of imperfection sensitive conical composite structures. In: International conference on composites/nano engineering, Tenerife; 2013.

[109] Barbero EJ, Madeo A, Zagari G, Zinno R, Zucco G. Imperfection sensitivity analysis of composite cylindrical shells using Koiter's method. 3rd International Conference on Buckling and Postbuckling Behaviour of Composite Laminated Shell Structures with DESICOS Workshop.

[110] Khakimova R, Warren CJ, Zimmermann R, Castro SGP, Arbelo MA, Degenhardt R. The single perturbation load approach applied to imperfection sensitive conical composite structures, Thin Wall Struct 2014; 84:369-377.

[111] Khakimova R, Zimmermann R, Di Pascua MF, Castro SGP, Arbelo MA, Degenhardt R. Buckling and postbuckling of truncated conical shells with varying semi-vertex angle: the use of the single perturbation load approach. In 54th Israel annual conference on aerospace sciences, Haifa; 2014.

[112] Arbelo MA, Herrmann A, Castro SGP, Khakimova R, Zimmermann R, Degenhardt R. Investigation of buckling behavior of composite shell structures with cutouts. Appl Compos Mater 2014; DOI 10.1007/s10443-014-9428-x.

[113] Castro SGP, Mittelstedt C, Monteiro FAC, Degenhardt R, Ziegmann G. Evaluation of non-linear buckling loads of geometrically imperfect composite cylinders and cones with the Ritz method. Compos Struct 2015; 122:284-289.

[114] Castro SGP, Mittelstedt C, Monteiro FAC, Arbelo MA, Degenhardt R, Ziegmann G. A semi-analytical approach for linear and non-linear analysis of unstiffened laminated composite cylinders and cones under axial, torsion and pressure loads. Thin Wall Struct 2015; DOI 10.1016/j.tws.2015.01.002.

[115] Barbero EJ, Raftoyiannis IG, Godoy LA. Finite elements for post-buckling analysis. II - application to composite plate assemblies. Comput Struct 1995;56(6):1019–1028.

[116] Andrade LG, Awruch AM, Morsch IB. Geometrically nonlinear analysis of laminate composite plates and shells using the eight-node hexahedral element with one-point integration. Compos Struct 2007;79:571–580.

[117] Xu H. Buckling, Postbuckling and Imperfection Sensitivity Analysis of Different Type of Cylindrical Shells by Hui's Postbuckling Method. University of New Orleans Theses and Dissertations 2013, Paper 1781.

[118] Lindgaard E, Lund E. Nonlinear buckling optimization of composite structures. Comput Meth Appl Mech Eng, 2010; 199(37-40): 2319-2330.

[119] Sze KY, Liu XH, Lo SH. Popular benchmark problems for geometric nonlinear analysis of shells. Finite Elem Anal Des 2004;40: 1551–1569.

[120] Debski H, Kubiak T, Teter A. Experimental investigation of channel-section composite profiles behavior with various sequences of plies subjected to static compression. Thin Walled Struct 2013;71:147–154.

[121] Brezzi F, Cornalba M, Di Carlo A. How to get around a simple quadratic fold. Numerische Mathematik 1986;48(4);417–427.

[122] Debski H, Kubiak T, Teter A. Buckling and postbuckling behaviour of thin-walled composite channel section column. Compos Struct 2013;100:195–204.

[123] Teter A, Kolakowski Z. Interactive buckling and load carrying capacity of thin walled beam columns with intermediate stiffeners. Thin Walled Struct 2004;42:211–254.

[124] Teter A, Kolakowski Z. Buckling of thin–walled composite structures with intermediate stiffeners. Compos Struct 2005;69: 421–428.